

*File with
N76-13139*

ATS 04139

**Video Guidance, Landing, and Imaging Systems
for
Space Missions**

by
Roger T. Schappell
Robert L. Knickerbocker
John C. Tietz
Christopher Grant
Robert B. Rice
Richard B. Moog

**REPRODUCIBLE COPY
(FACILITY CASEFILE COPY)**

Prepared under Contract No. NAS 1-13558 by
MARTIN MARIETTA CORPORATION
DENVER DIVISION
DENVER, COLORADO 80201

for

NATIONAL AERONAUTICS AND SPACE ADMINISTRATION

FOREWORD

This report presents results of a 15-month video guidance, landing, and imaging systems feasibility study and laboratory evaluation program. Digital simulation results, experimental results, and the laboratory hardware used in development of the required technology are summarized herein. The last chapter of this report contains a summary of the mission-related achievable benefits and an outline of recommended action for further development and implementation of this technology.

CONTENTS

	<u>Page</u>
INTRODUCTION	1
	thru
	4
THEORY OF OPERATION	5
Planetary Lander Site Selection, Navigation, and	
Obstacle Avoidance	5
Earth Resources Orbiting Vehicles	10
Earth Orbital Rendezvous and Docking	12
	thru
	16
PHYSICAL SIMULATOR AND VIDEO SYSTEM ELECTRONICS . . .	17
Physical Simulator	17
General Description	21
Functional Description	25
Computer Interface	34
Simulator Software	35
Surface Model	38
	thru
	42
EXPERIMENTAL RESULTS	43
Camera Calibration and Checkout	43
Algorithm Evaluation Experiments for Planetary	
Landers	46
Pointing and Tracking for Earth Resources	
Applications	61
Rendezvous and Docking Experiments	71
	thru
	82
ANALYSIS OF ENTRY NAVIGATION FOR PLANETARY LANDERS .	83
System Operation	84
Simulation Results	85
Offset Aim Point Strategy	90
Conclusions and Recommendations	94
ANALYSIS FOR TERMINAL DESCENT PHASE GUIDANCE FOR	
PLANETARY LANDERS	96
Lander Constraints and Propulsion System	96

	<u>Page</u>
Impact of Additional Fuel on Propulsion System	99
Maneuver Capability	99
Effects of Scan Positioning	108
	thru
	113
SCIENTIFIC IMAGING CONSIDERATIONS	114
Introduction	114
System Operation	114
Viking Data Link Capability	116
Entry Vehicle Dynamics	119
Typical Data Storage and Transmission Requirements	122
Conclusions and Recommendations	123
SUMMARY AND RECOMMENDATIONS	124
Planetary Landing Site Selection System	124
Earth Resources Pointing and Tracking System	127
Video Stationkeeping and Docking Sensor System	130
Aircraft Approach and Landing System	133
Future Study Recommendations Summary	135
	thru
	136

FIGURES

1. Reference Mission - Viking	7
2. System Operation	8
3. Scan Format	9
4. Video Signal Processor	9
5. Acquisition & Tracking Methodology	11
6. Onboard Rendezvous and Docking System Configuration	12
7. Video Processor Block Diagram	14
8. Far-Steering Video Functions	15
9. Near-Steering and Stationkeeping	16
10. Six-Degree-of-Freedom Laboratory Simulator	18
11. Control Console	19
12. PDP-9 Digital Computer	20
13. VGLIS Simulator System Block Diagram	22
14. Simulator Control Panel	24
15. Image Dissector	26
16. Digital Sweep Control System Block Diagram	27
17. Sweep Control Panel	28

	<u>Page</u>
18. Video Processing Electronics	31
19. Carriage Servosystem Single-Axis Block Diagram .	32
20. Lens Servosystem Single-Axis Block Diagram . . .	33
21. Monte Carlo Run	37
22. Scaled Surface Model	38
23. Scaled Surface Model and ERTS Photograph	39
24. Desert Land Forms of Peru	40
25. Spatial Frequency in Object Space, 1 p/mm	45
26. Zoom Lens Characteristics	47
27. Monitor Observations for a Typical Experiment at 1-sec Intervals	49
28. Monte Carlo Experiment	50
29. Monte Carlo Run - Subframe Size Experiment with Best Area Selected	53
30. Monte Carlo Run - Minimum Row/Column Steering . .	53
31. Monte Carlo Run - Scientific Site Biasing	54
32. Monte Carlo Run (Field-of-View = 8.68 deg) . . .	55
33. Distribution of Ratings for 208 Randomly Selected Sites on Model	57
34. Crash Probability versus Sun Angle	58
35. Monte Carlo Run - Sun Angle = 30 deg from Normal to Surface	60
36. Monte Carlo Run - Sun Angle = 45 deg from Normal to Surface	60
37. Monte Carlo Run - Sun Angle = 50 deg from Normal to Surface	60
38. Monte Carlo Run - Sun Angle = 60 deg from Normal to Surface	60
39. Scan Configuration	62
40. Circuitry for Computing Vector Components	63
41. Vector Length Versus Wavelength for Various Interfaces	66
42. Multi-Spectral Scanning Scheme	67
43. Record of Track Produced by Algorithm	68
44. Landsat Image of Chesapeake Bay	68
45. Target for Cloud Experiment	70
46. Tracking Experiment Results	70
47. Laboratory Setup	71
48. Test Scene	72
49. Digitized Brightness Map	73
50. Thresholded Version	73
51. Area Test of Simulated Satellite	75
52. Object Center Test	76
53. Center Test, Simulated Spacecraft	77

	<u>Page</u>
54. Orientation Test	78
55. Stereo Ranging Test	79
56. Spectrum of Roll Capability (PT. Mass)	85
57. Mean Atmosphere Chute Deployment Constraints on Roll	86
58. Roll Effect on Dynamic Pressure Profile	87
59. Down and Crossrange Capability (PT. Mass)	88
60. 6 DOF Roll Capability	89
61. Altitude/Time Correlation	91
62. Mach Number and Dynamic Pressure	91
63. Predicted Impact Point History	92
64. Roll and Roll Command	92
65. Down and Crossrange Errors	93
66. Offset Aim Point Used with Roll Maneuvering	93
67. Viking Velocity - Altitude Descent Contour	97
68. Viking Maximum Maneuver Capability	100
69. Terminal Descent Guidance and Control System	102
70. Maximum Maneuver Capability Footprints	103
71. Post Optimization Algorithm	104
72. Crossrange Maneuver Capability	107
73. Scan Always Centered at PIP	109
74. Digital Surface Simulation	110
75. Digital Simulation of Sensor Field-of-View	110
76. Scan Positioning Logic Summary	111
77. Scan Positioned by Requiring Selected Area Coordinates to Remain Constant	112
78. Predicted Impact Point Traces for Landings	112
79. Scan Positioned by Moving to Boundary of Previous Area	113
80. Pitch Rate During Parachute Descent	121
81. Yaw Rate During Parachute Descent	121
82. Monte Carlo Experiment Results	125
83. Advantages of a Landmark Tracker for Earth Orbital Missions	128
84. Helicopter Automatic Approach and Landing System	134

TABLES

I. Area Calculation	74
II. Area Measurement Repeatability	74
III. 6 DOF Landmark Navigation Test Cases	88
IV. Post Iteration History	106
V. Maximum Maneuver Distances	107
VI. Camera Resolution Versus Time	116
VII. Viking Relay Link Operating Modes	117
VIII. Viking Entry Dynamics	119
IX. Viking Data Storage and Transmission	122
X. Study Results for Interplanetary and Lunar Missions	126
XI. Study Results for Earth Resources Missions	129
XII. Study Results for Spacecraft Rendezvous and Docking Missions	131

VIDEO GUIDANCE, LANDING, AND IMAGING SYSTEMS FOR SPACE MISSIONS

By: Roger T. Schappell, Robert L. Knickerbocker, John C. Tietz,
Christopher Grant, Robert B. Rice, and Richard D. Moog

INTRODUCTION

This study is concerned with exploring the adaptive potential of video guidance technology for earth orbital and interplanetary missions. Since a number of imaging systems are available and will undoubtedly be flown on future spacecraft for scientific imaging, inspection or remote control functions, it is logical to explore further utility and capability of these sensors in terms of autonomous real-time target acquisition, pointing, and tracking, thereby augmenting the primary guidance, navigation, and attitude control hardware, and enhancing the scientific data gathering ability of the vehicle.

More specifically, this study is concerned with the application of video acquisition, pointing, tracking, and navigation technology to three primary missions--a planetary lander, earth resources satellite, and spacecraft rendezvous and docking. Emphasis is on maximum use of available information to enhance the onboard decision-making capabilities of a given spacecraft.

In the case of a planetary lander, it is desirable to provide navigation during entry, and scientific site selection and obstacle avoidance during the terminal descent phase of flight by way of autonomous real-time observation and decision making. This technology has been investigated and successfully demonstrated in the laboratory and is included in the report.

Another requirement exists in the area of future earth resources satellites whereby acquisition and tracking of a particular surface feature or other constituent of interest would greatly increase the use of directive sensors, and minimize data transmission bandwidth and time requirements. Optimization of useful science information return, as a function of time in orbit, would result from the adaptiveness provided by the pointing and tracking system.

A third area of concern is rendezvous and docking of spacecraft for inspection, refurbishment, and retrieval missions.

It has been established that most future spacecraft such as Space Tug, Earth Orbital Teleoperator and Free Flying Satellite Experiments will carry a TV camera for manned observation and possibly remote control. Since a camera is available and the potential mission requirements are such that real-time autonomous operation would extend the operational capability of the chosen vehicle, consideration must be given to maximum use of available data such as the video output. A discussion of the feasibility of this technique and experimental results is reported herein.

The primary objective of this study is to develop algorithms for the missions discussed above, and evaluate them in the laboratory using a physical simulator and scaled surface models. The first phase of this study resulted in a successful feasibility demonstration of the planetary landing site section system.* Subsequent to this, other algorithms were developed and tested for the earth resources and rendezvous and docking missions, respectively.

The approach taken was:

- (1) Establish reference mission requirements and constraints.
- (2) Perform necessary analytical and digital simulation studies to assist in arriving at representative guidance and navigation requirements.
- (3) Develop video data processing algorithms as a function of target characteristics and observables.
- (4) Breadboard video data processing logic and integrate it with the TV camera, display, and physical simulator.
- (5) Develop software for automating experiments and for providing a permanent record of results.
- (6) Design and build scaled surface models.

*Schappell, R. T., Knickerbocker, R. L., Tietz, J. C., Grant, C., and Flemming, J. D.: Video Guidance, Landing, and Imaging System System (VGLIS) for Space Missions, Final Report, NASA CR-132574, February, 1975.

- (7) Integrate and checkout 6D simulator, breadboarded algorithms, scan electronics, TV camera, surface model, and PDP-9 scientific computer.
- (8) Run experiments and document results.

The significance of this study, as verified by the analytical and experimental results, is that the output of a scanning sensor system such as a TV camera can be operated on by conventional filtering techniques and simple processing algorithms to arrive at an adaptive and autonomous sensor system capable of making intelligent decisions with regard to the observed area or constituent of interest.

In other words, one does not require computational and hardware complexity to provide a degree of intelligence for the applications of interest to this study. On the other hand, further experimental work is required to provide a more comprehensive definition and selection of the observables, and to optimize the algorithms and data formatting electronics for a particular mission. This future activity is discussed in the summary and recommendations section.

Documentation of the study results was somewhat complicated by the three missions of interest; however, because of commonality of experimental equipment and simulator, and the experimental approach, the contents of this report is organized in the following manner:

The Introduction describes the main objectives, the study approach, and the general study results.

The Theory of Operation chapter is as implied and also includes a summary of the guidelines as provided by NASA.

The Physical Simulator and Breadboard Electronics chapter contains a full description of the six-degree-of-freedom laboratory simulator, the scaled surface models, the simulator/PDP-9 scientific computer interface, the video system breadboard electronics, as well as a description of the software developed for automating the experimental procedure and for providing experimental flexibility in terms of video processing algorithm evaluation.

The Experimental Results chapter describes the experimental procedures, calibration, algorithm evaluation procedures, and the Monte Carlo simulation activity used in establishing system

feasibility. Actual experimental data is presented for each of the three missions.

The analysis chapters on Entry Navigation and Terminal Descent Phase Guidance are applicable to the planetary lander mission only and are based on results derived from a modularized six-degree-of-freedom trajectory program that is capable of simulating orbiting vehicles and planetary landers of various types.

The Scientific Imaging considerations chapter addresses the use of a TV camera in an imaging mode to record or transmit photographs of the landing site during the entry through terminal descent phases of a planetary landing.

The Summary and Recommendations chapter presents an overview of the results and suggests an approach to the further development and use of the video guidance technology.

The simplicity of design and added scientific use of this technology make it particularly applicable to future earth orbital and planetary programs requiring onboard intelligence and a measure of adaptive performance as a function of the observed environment.

THEORY OF OPERATION

The operational modes for the various missions that were considered in this study are described to provide the reader with an understanding of possible benefits achievable through use of adaptive guidance and control mechanizations. Again, it must be emphasized that the uniqueness is in the signal processing hardware and not necessarily in the sensor head. Although an image dissector was used in laboratory experiments in performance of this study, other cameras, low-light-level television, IR scanners, etc, may work equally well; however, a sensor selection effort should be part of a later study and would be based on spectral radiance characteristics of the target, spatial resolution requirements, and other mission-related characteristics.

This chapter of the report, presented in three sections--planetary landers, earth resources orbiting vehicles, and earth orbital rendezvous and docking vehicles--will be discussed in that sequence.

Planetary Lander Site Selection, Navigation, and Obstacle Avoidance

Studies relating to stellar-body exploration programs have pointed out the need for an adaptive guidance scheme capable of providing automatic real-time guidance and site selection capability. For the case of a planetary lander without such guidance, targeting is limited to what are believed to be generally favorable areas to ensure a reasonable landing-success probability. The Mars Viking Lander will be jeopardized by obstacles exceeding 22 cm in diameter. The need is further dramatized by the failures of the Russian Mars landers and the Luna 23 that was damaged on impact. Conversely, the benefits of onboard navigation and real-time selection of a landing site and obstacle avoidance have been demonstrated by the Apollo lunar landings, in which man performed the surface sensing and steering functions. Therefore, an adaptive video guidance system has been developed, breadboarded, and flown on a six-degree-of-freedom simulator.

The Viking Mars mission was used in this study to arrive at consistent and realistic design requirements and goals. The system must be compatible with the Viking lander in mission profile, vehicle dynamics, interfacing, and environmental requirements. It also must be able to detect and avoid 22-cm obstacles during the latter portion of the terminal descent phase; therefore, a TV imaging system with contrast detection logic was chosen

for the reference configuration, and it is hereafter referred to as the adaptive video guidance system (AVGS).

The primary objective for the first phase of this study was to design and test a breadboarded video guidance system that would demonstrate the capability to autonomously select the least hazardous landing site on a scaled three-dimensional planetary surface model. This was accomplished by a coordinated physical and digital simulation effort that established system feasibility, which was based on the system's ability to repeatedly locate an acceptable landing site in arbitrary areas regardless of initial conditions. The second phase of this study was concerned with scientific site selection and entry guidance, which are discussed later in this report.

The following guidelines were used in performance of the planetary lander related effort:

- (1) The lander vehicle and flight characteristics were assumed to be similar to those of the '75 Viking vehicle.
- (2) A median atmospheric density profile exists at terminal descent altitudes.
- (3) The lander propulsion system may have up to 10 kg of propellant available for site selection maneuvers.
- (4) The Mars terrain model shall have several hazardous regions and several "safe" landing sites.
- (5) The color and texture of the terrain surface and its illumination should be chosen to represent nominal surface conditions, not extreme conditions.

AVGS is a unique approach to increasing the probability of a successful landing on an undefined surface. It will, therefore, significantly contribute to the adaptive capability of a spacecraft targeted to a solar body. The primary ingredients of the AVGS are a TV camera sensor and the processing electronics that operate on raw video data and output a steering bias to the lander computer. The uniqueness of this approach is in the video signal processing logic, which is simple in design and makes maximum use of the available data.

In the case of a planetary lander application such as the Viking Mars mission, the AVGS would be activated after having jettisoned the parachute and would continue to function during the terminal descent phase, as shown in Figure 1.

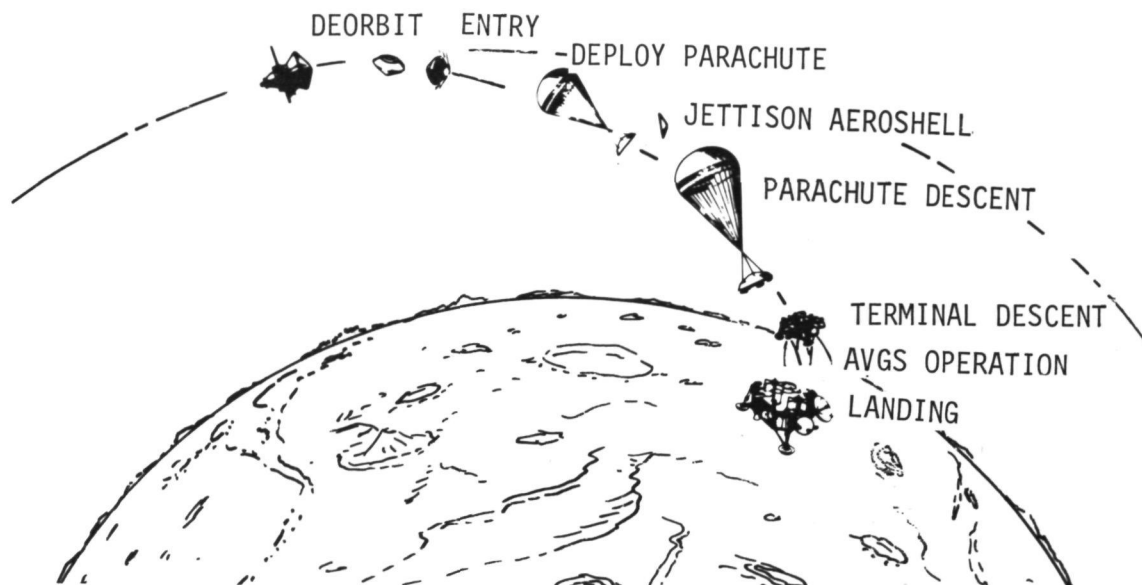


Figure 1 Reference Mission - Viking

At approximately 1000 meters, the system is activated and dynamically scans the area surrounding the predicted impact point (PIP) as determined by the lander computer. The video data are then processed, resulting in a steering command to the lander computer and, consequently, to the propulsion subsystem to avoid rocks, craters, and major slopes, as shown in Figure 2. The PIP is always within the total field of view (TFV) capability of the AVGS. The TFV is necessarily large to permit observance of the PIP in spite of anticipated vehicle attitude excursions necessary for maneuvering during the terminal landing phase. Use of electronic beam positioning obviates the need for extensive data processing of the entire area, for mechanical gimbals, and for reorienting the vehicle to observe the area about the PIP. The scanned TFV is a fixed angle; the surface area scanned diminishes as a function of altitude while resolution improves. The logic permits observation and avoidance of major surface features at higher altitudes where maximum maneuvering capability can be achieved with minimum fuel consumption. After the AVGS scans the surface,

the video data are processed and a new impact point is selected (the area with the least contrast). A bias steering command to the lander computer initiates maneuvering to the preferred landing site. The sequence is repeated at intervals on the order of every second to approximately 15 meters from the surface. Operating time varies from 20 to 34 seconds as a function of propulsion system constraints, control system philosophy, atmospheric density, wind velocity, and maneuvering distance requirements.

The site selection algorithm is implemented in the following manner. Receiving a positioning command from the lander computer, the scanned TFV is centered about this point, and a matrix of A_{ij} areas is scanned, as shown in Figure 3.

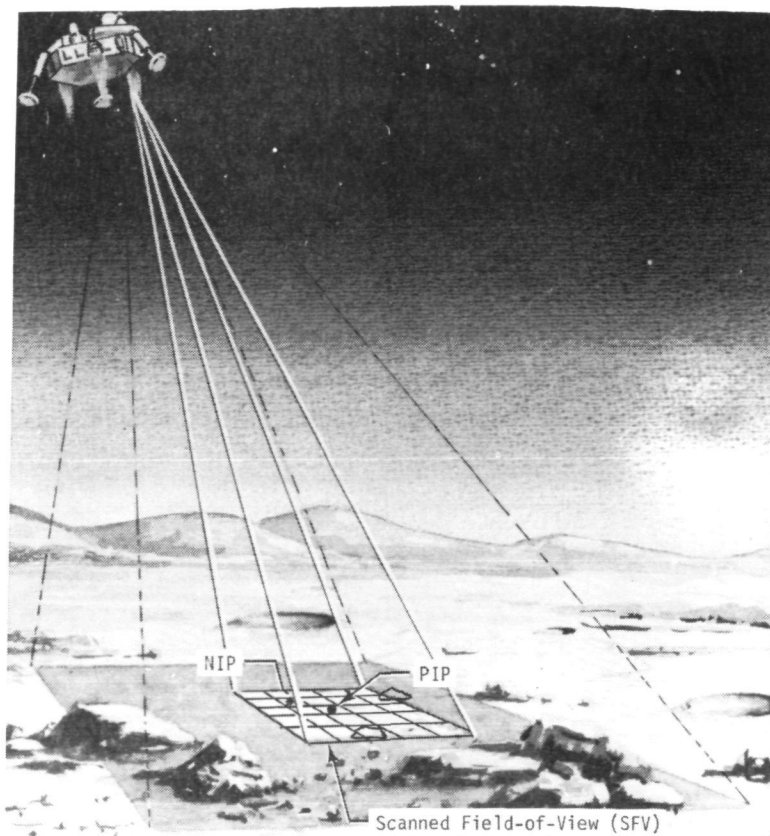


Figure 2 System Operation

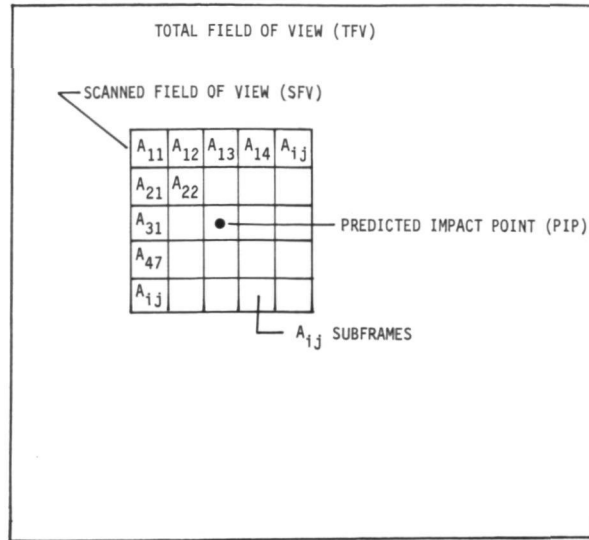


Figure 3 Scan Format

Scanning of the A_{ij} subframes is accomplished by biasing scanning signals to move the scanned area on the photocathode to each of the A_{ij} areas. Typically, each subframe is sequentially scanned with 100 lines and 100 picture elements per line. The video signal is then processed by the appropriate filters, as shown in Figure 4.

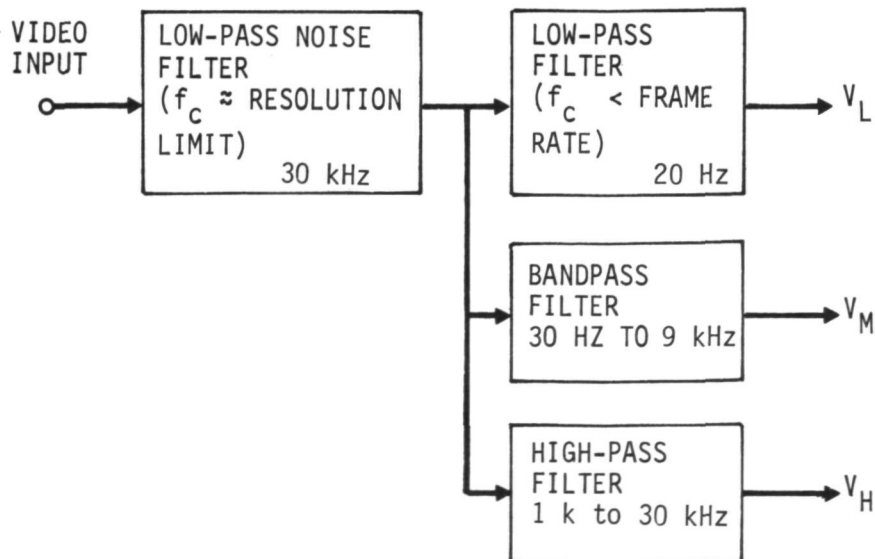


Figure 4 Video Signal Processor

In this diagram, a 30 kHz low-pass filter is used to remove noise at frequencies above the resolution limit of the camera. The second low-pass 20-Hz filter has its output proportional to the dc components of the video signal. The high-pass filter extracts the 1- through 30-kHz portion of the video signal. The three output signals, V_L , V_H , and V_M , represent the rectified integral of the dc component, the high-frequency ac components, and the low- to middle-frequency ac components of the video signal, respectively. These outputs are then used in calculation of the "suitability rating" for each subframe. The rating scheme is as follows:

$$\text{Rating} = a \left(\frac{|\bar{V}_M|}{|\bar{V}_L|} \right) + \left(\frac{|\bar{V}_H|}{|\bar{V}_L|} \right) \text{ where } |\bar{V}_M|, |\bar{V}_H|, \text{ and } |\bar{V}_L| \text{ are}$$

the absolute values of average values of V_M , V_H , and V_L for a subframe. The weighting factor, a , was selected empirically to give the best agreement between the algorithm and the experimenter's subjective evaluation of various areas.

The ratings for the A_{ij} subframes are then compared, and the one with the lowest rating is selected as the new impact point.

Earth Resources Orbiting Vehicles

The objective of this task was to establish the feasibility of remote acquisition, pointing, and tracking for future earth resources applications that would "aid" in pollution monitoring, flood plain observations, survey missions, constituent tracking, etc. The goal is to investigate technology that will lead to development of a uniquely simple and adaptive sensor mechanization to enable use of a scanning imaging system to acquire and track various targets of scientific interest to maximize data return for a given mission.

Typically, a coastline tracker and cloud detection system would operate in the manner illustrated in Figure 5.* During a particular orbital pass, the primary objective is to acquire and track the river, the ocean coastline being a secondary objective. Cloud cover areas are to be avoided. A horizontal scan is made of the entire swath, slope is measured for a given spectral region, and the coastline is detected. The sensor maintains lock until it encounters a cloud front whereupon it performs another scan until the coastline is acquired, and then proceeds to orient the science instrumentation with respect to the acquired coastline. Details of the algorithm used and the results achieved experimentally are included in the Experimental Results chapter. A real-time acquisition, tracking, and control mode would be used to point the science instrumentation.

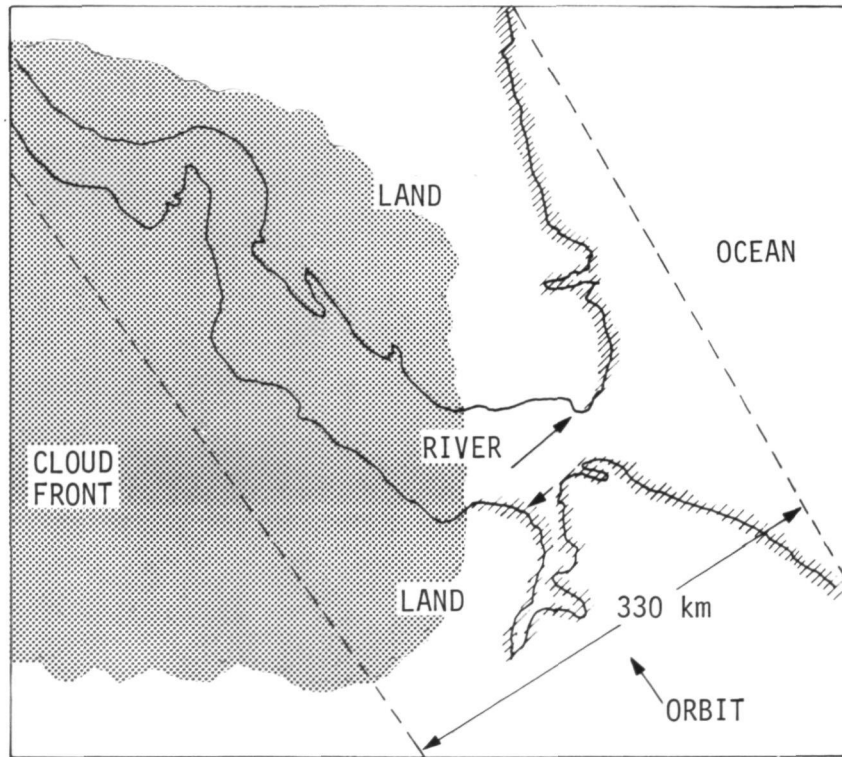


Figure 5 Acquisition and Tracking Methodology

*Staylor, W. F., and Harrison, E. F.: Study of a Water Quality Imager for Coastal Zone Missions. Presented at 21st Annual Meeting of the Institute of Environmental Sciences, Anaheim, California, April, 1975.

Earth Orbital Rendezvous and Docking

This task outlines an approach to provide automatic steering and stationkeeping on an unmanned vehicle for rendezvous and inspection of other spacecraft. The system comprises a TV camera, specialized scan control, analog preprocessor or dedicated microprocessor, and onboard digital computer as shown in Figure 6. The system components function in much the same way as the planetary lander video guidance system in that the digital computer provides a supervisory function while high data rate computation is performed in the microprocessor hereafter referred to as the video processor (VP). Large data block storage in the spacecraft digital computer and a high-speed A/D converter interface are, therefore, not required. The system is essentially self-contained, thus minimizing processing by the onboard computer.

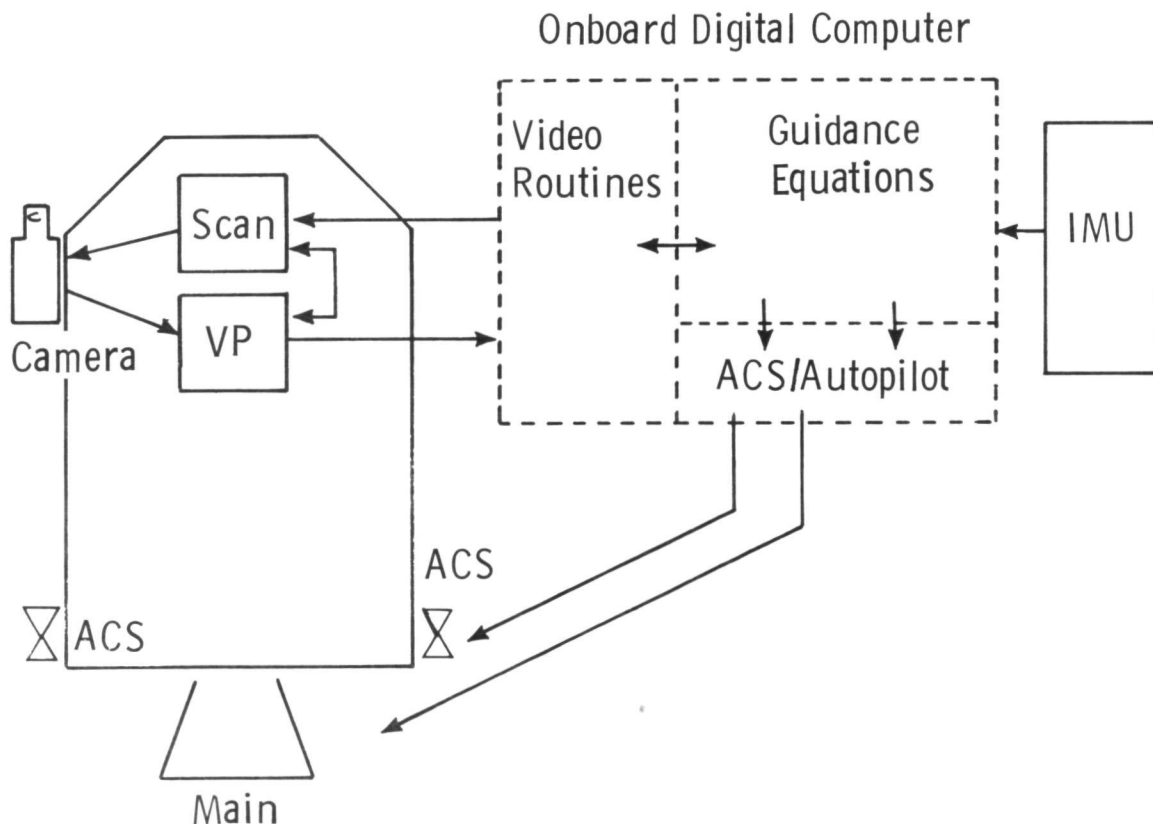


Figure 6 Onboard Rendezvous and Docking System Configuration

The several different tasks will be based on a common sequence of processing. The camera is commanded to scan a certain area of given coordinates and size of scan in the field of view. The VP operates on the camera data and issues discrete values to the spacecraft digital computer at the end of a frame. The digital computer then decides what the next camera operation and VP function will be. A wide variety of tasks may be accomplished in this manner depending on the digital computer software. With this scheme, all mundane calculations are performed in the VP, leaving the digital computer free for other work and allowing lower data rates on A/D converters. Also, detailed logic and complex calculations are resident in the digital computer that is best suited to this purpose.

As an example of this type of processing, consider the problem of horizon detection. Assume the object is a bright disk on black background. The digital computer would set the camera frame size to be approximately twice the expected area of the object. A frame would be scanned in which the VP would take the following functions: integral video (threshold), first X moment, first Y moment. At the end of scan, this information is passed to the digital computer, which calculates area, diameter and center in X and Y coordinates. The next step would be to scan four smaller frames that would be positioned to cross the limb in each of four directions for more accurate measurement. The digital computer would command each of these in sequence and retain the results for a precise determination of object relative position. During scans, the digital computer is free for other tasks while the VP is collecting data.

The basic functions required in the VP, of course, depend on the particular task, but it would appear the following are adequate for most and are surprisingly easy to accomplish in the analog hardware or microprocessor as well. The following functions are to be calculated over one frame of scan.

Ave	Integral of the video signal
S_X	First moment of the video signal in the X direction
S_Y	First moment of the video signal in the Y direction
I_{XX}	Second moment of the video signal in the X direction
I_{YY}	Second moment of the video signal in the Y direction
I_{XY}	Cross Moment

Figure 7 shows a block diagram of the VP. As shown, some thresholding and filtering of the video is required. The system shown is a small analog version of the processor, commanded directly by the digital computer. It is also possible to mechanize these functions in a microprocessor.

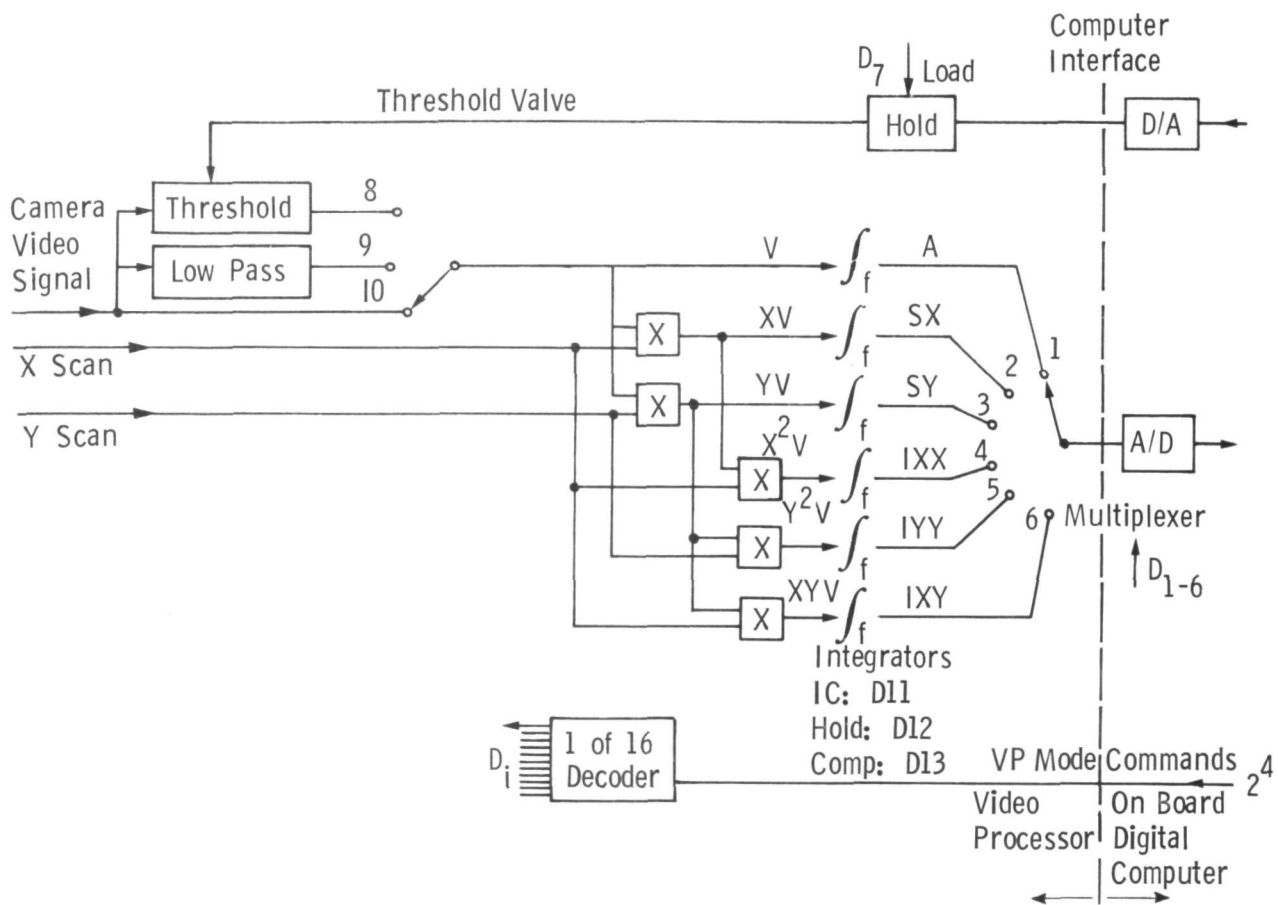
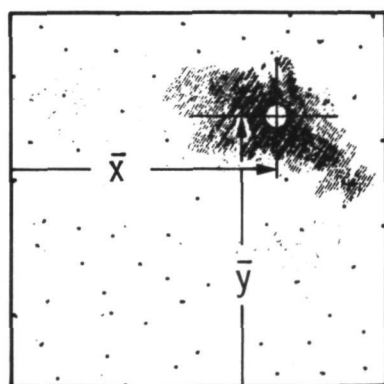


Figure 7 Video Processor Block Diagram

A hypothetical mission would proceed as follows directed by the digital computer logic.

- (1) Far Steering
- (2) Near Steering
- (3) Feature Detection and Inspection
(Track Intermittently)
 - (a) Spacecraft Sizing
 - (b) Axis Orientation Determination
 - (c) Spin Rate Determination
 - (d) Home on Predetermined Features
 - (e) Determine Whether Dock Is Feasible
 - (f) Docking Maneuver

Figure 8 shows a simplified scene and the associated video functions required for far steering. The guidance equations determine when the object is within range and field of view. Then a frame is scanned and the VP takes A , S_X , and S_Y . The digital computer then calculates \bar{X} and \bar{Y} in camera coordinates and translates these to steering signals. At the appropriate distance, determined from A (proportional to size) or a ranging device, the system changes to near steering logic, as shown in Figure 9.



Scene

VP Functions per Frame of Scan

$$\begin{aligned}
 A &= \int_f \text{Video}^* dt \\
 S_X &= \int_f \text{Video} X_S dt \\
 S_Y &= \int_f \text{Video} Y_S dt.
 \end{aligned}$$

Then the Object Center is Defined by

$$\begin{aligned}
 \bar{X} &= S_X/A \\
 \bar{Y} &= S_Y/A
 \end{aligned}$$

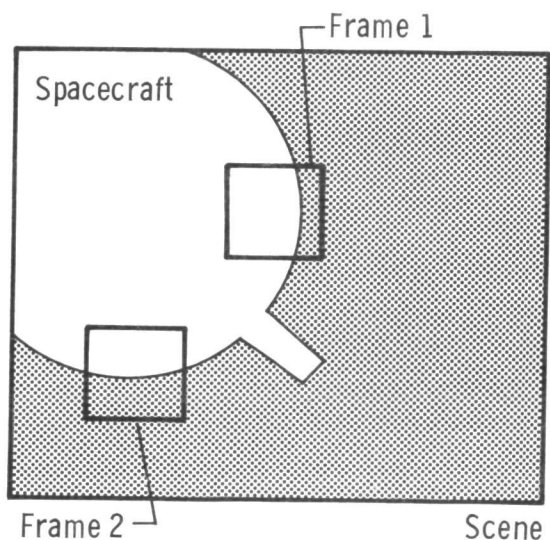
* It May be Required for Low-Pass Filter to Remove Starfield and Modify the Gray Scale for Contrast Enhancement

Figure 8 Far-Steering Video Functions

Figure 9 shows one possible method of near steering and stationkeeping to be performed while doing other tasks. This approach may be used while taking pictures, looking for pre-determined features, or performing surveillance maneuvers.

Following are a few of the functions that may be performed with appropriate software additions and the same basic hardware.

- Geometric Area
- Average Brightness
- Object Center in the Field of View
- Major and Minor Axes of an Equivalent Ellipse
- Angular Orientation of Major Axis
- Search for Predetermined Feature
- Track Feature (i.e., automatic docking)
- Determine Spin Axis and Spin Rate



Given Approximate Data from Previous Scans, Accurate Relative Position Is Obtained by Scanning an Area Covering Object Boundaries in Two or More Places. By Knowing the Commanded Scan Coordinates and the Relative Placement of the Camera, Frame 1 Yields Data on the X Position of the Spacecraft Edge, While Frame 2 Shows What the Y Coordinate Is.

Figure 9 Near-Steering and Stationkeeping

PHYSICAL SIMULATOR AND VIDEO SYSTEM ELECTRONICS

The Video Guidance, Landing, and Imaging Systems simulator hardware is described in detail in the following paragraphs. This subsection contains a description of the physical layout of the simulator, and the remainder of the section deals with functional characteristics and surface models.

Physical Simulator

Based on physical location, the VGLIS simulator may be divided into four major subsystems--the simulator carriage, control console, computer, and surface model.

Figure 10 (6-D simulator) shows the simulator carriage. The long horizontal boom moves along vertical tracks at each end. This degree of freedom is defined as the Z axis. The smaller horizontal boom moves left and right along the larger boom for the $\pm X$ motion. A third assembly moves along the small boom to provide the third degree of freedom, $\pm Y$. Mounted on this third assembly are the camera electronics and a set of attitude gimbals which provide the remaining three degrees of freedom: pitch, yaw, and roll. The camera head and motorized lens are placed within the roll axis ring gear. The entire carriage is precisely counterweighted to offset any biased load on the Z-axis motors. In the right rear of the laboratory, the solar simulator can be seen.

Figure 11 depicts the control console, which is situated on an elevated platform in the same laboratory as the simulator carriage. The left section of the console contains the sweep control panel and video filters. The video monitor can be seen in the center section, and on the right are the simulator control panel and a digital voltmeter used for various monitoring functions. The simulator control panel includes the manual controls for the carriage and lens, the master and servo power controls, and the switches that control whether operation is in the manual or automated mode. The power supplies and camera control unit are below the desk surface of the console. To the right of the console is the teletype used for computer input.

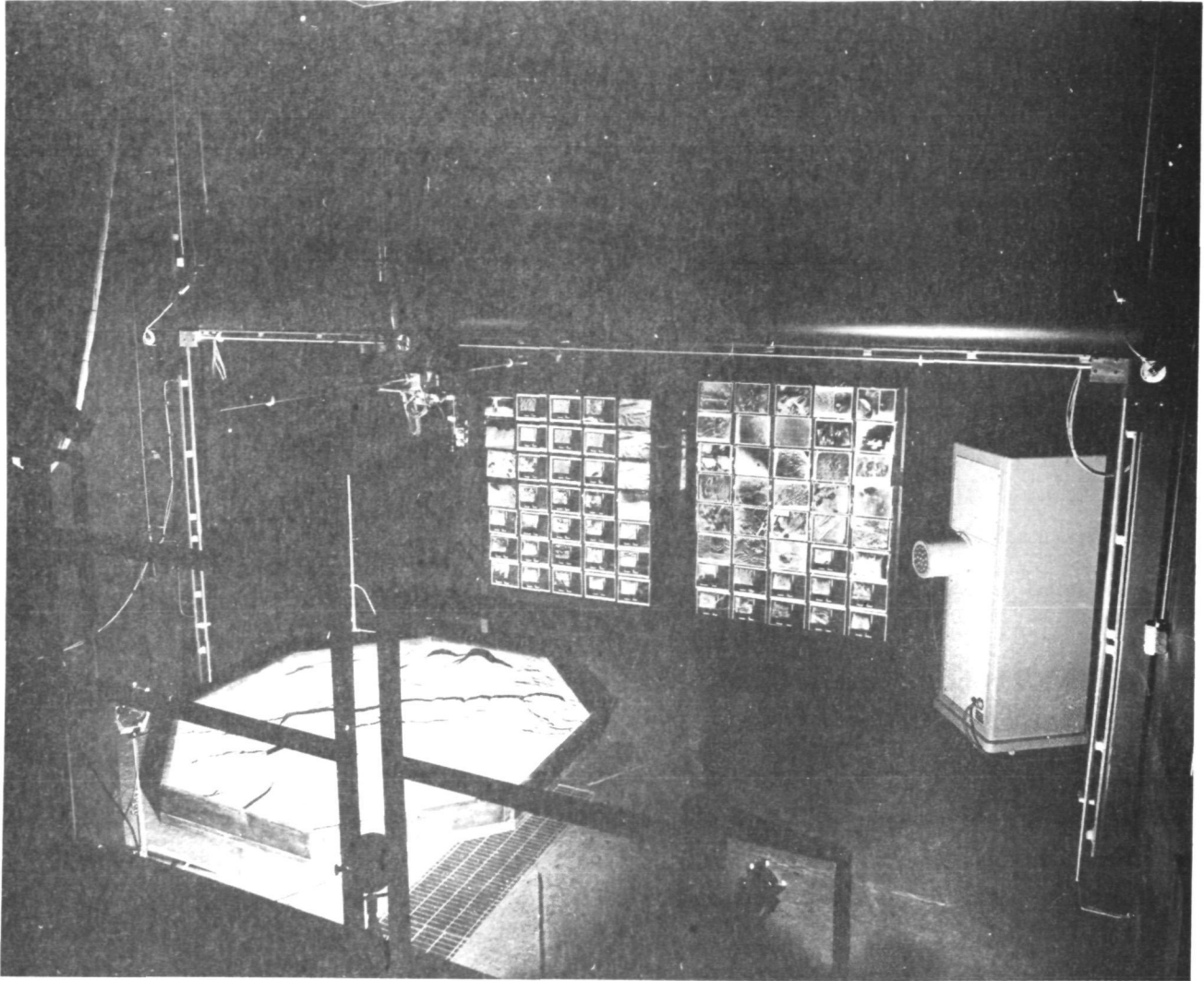


Figure 10 Six-Degree-of-Freedom Laboratory Simulator



Figure 11 Control Console

Figure 12 shows the Digital Equipment Corporation PDP-9 digital computer. The computer is the large unit on the right. The smaller unit at the left is the printer. During an experiment, the computer (1) configures the sweep control circuits in the control console to generate the desired sweep pattern, (2) processes the resulting video signals, and (3) directs the simulator servosystems to move to a new location based upon the results of the video signal analysis.

During the performance of this study, extensive modifications were made to the video scan electronics, processing electronics, PDP-9 software, and surface models. This resulted in the implementation of a flexible simulator usable for a wide variety of missions. This section provides a discussion of the entire laboratory setup that was used in acquiring the experimental results appearing in the next section. An interesting aspect

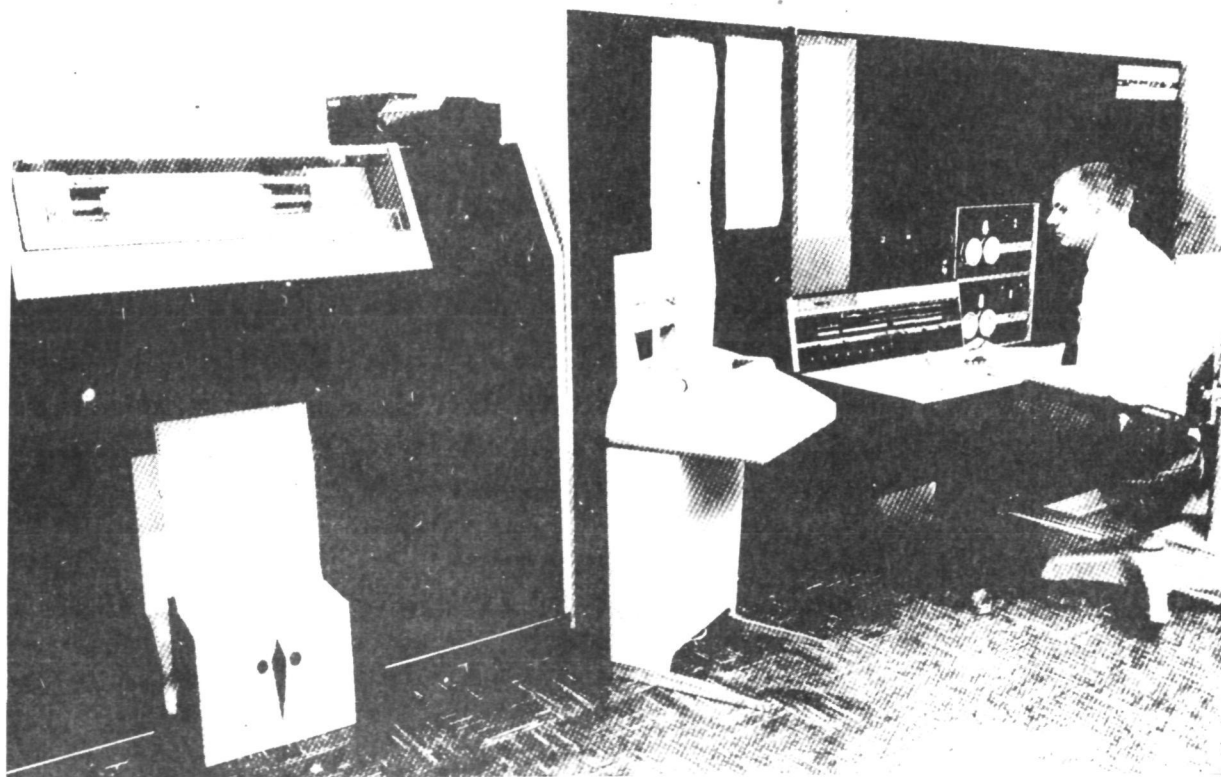


Figure 12 PDP-9 Digital Computer

of this laboratory is that in many cases algorithms can be programmed on the PDP-9 computer, which then emulates the actual hardware and is tied into the physical simulator, sensor head, and scaled targets or surface models. The results are significant savings in time and cost and added confidence in eventual breadboard hardware.

General Description

The preceding discussion treated the system as comprising four separate entities. The system will be described in detail in the following paragraphs grouped by functional characteristics rather than physical location.

Figure 13 shows the complete block diagram of the VGLIS simulator. Signal flow and physical location of the elements can be seen. By function, the blocks can be grouped into four categories: (1) video system, (2) simulator servosystems, (3) special circuits, (4) computer interface circuits. Each of these categories will be discussed in still further detail in the sections to follow. The discussion here will deal with their relationship to the total system.

Video System

The video system makes use of a vidisector camera that is trained on a target such as a surface model. For the camera to produce the desired video signal, it is necessary to cause the electron beam to sweep across the vidisector cathode in the desired pattern. This pattern is produced by the digital sweep control circuits under either manual or computer command. The sweep control circuits in conjunction with the sweep control panel and computer are capable of producing virtually any kind of sweep configuration from a standard TV raster to a helical scan pattern. The primary outputs from the digital sweep control circuit are applied to the console monitor and to the camera sweep amplifiers in the camera electronics module via the camera control interface. The camera control interface is little more than a junction box that serves to supply power and sweep signals to the camera electronics module and route the incoming signal to the video processing circuits. The camera electronics module is located near the camera head and attitude gimbals on the simulator carriage. It serves to modify the sweep signals so that they are capable of driving the deflection coils on the vidisector tube. It also provides a high voltage for the electron multiplier. The camera head contains the vidisector tube,

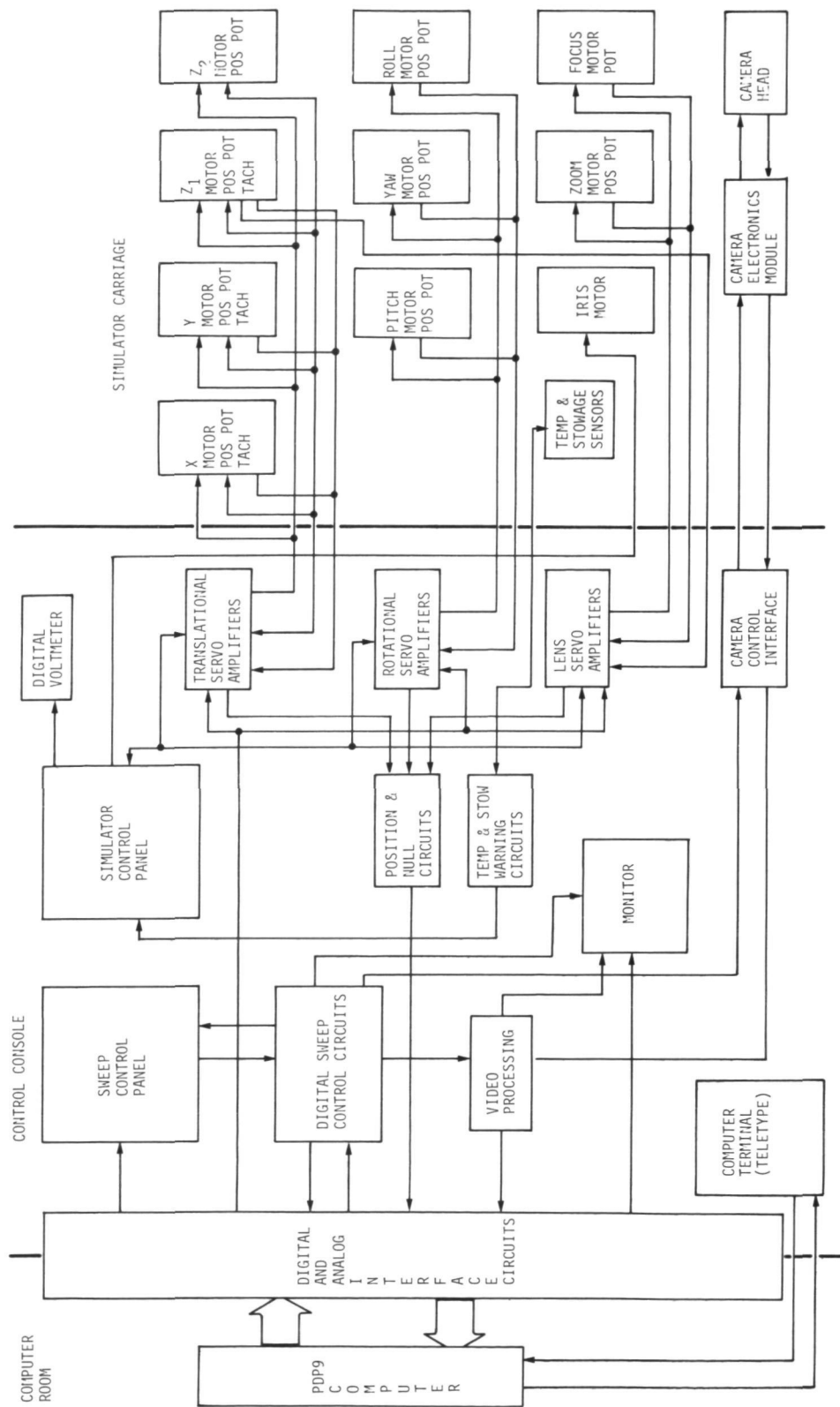


Figure 13 VGLIS Simulator System Block Diagram

deflection coils, and a video preamplifier to boost the video signal before it is sent back down the cable to the camera control interface. The video is not further modified until it reaches the video processing circuits. There, the video is first amplified and sent to the monitor. Next, it is filtered to separate a middle band of frequencies, rectified and integrated to yield two outputs that reflect the energy content at low and middle frequencies. This information is then sent to the computer for the decision-making process.

Simulator Servosystems

The simulator servosystems for the translational and rotational axes are standard d-c servomotor loops. The vertical (Z) axis has two motors, Z_1 and Z_2 . Two motor drives were necessary because the ends of the long boom are widely separated and travel on two vertical tracks at opposite ends of the simulator room. X and Y have only one drive point each and, therefore, have only one motor. Position and rate signals are fed back to the servoamplifiers to allow position control and enhance stability. The rotational servoamplifiers are similar except that the motors are smaller, require less drive power, and do not employ rate feedback. The lens servoamplifiers control only zoom and focus. Precise iris control was believed unnecessary so the only control over the iris is a switch on the simulator control panel, as illustrated in Figure 14. Zoom and focus are servo controlled, but the circuits are not quite so straightforward. Focus varies with height so a nonlinear transfer function is generated within the servo loop to enable focus to track variations in the Z axis. A similar process is used in the zoom amplifier to make focal length vary linearly with the input voltage. The simulator control panel has controls that allow the servoamplifiers to be driven by computer commands or manual commands. In the manual position, the six simulator axes are driven in the rate mode while focus and zoom have manual position controls. The simulator control panel also controls master power and has an array of switches to allow a number of system functions to be monitored in a DVM located directly above the control panel.

Special Circuits

The position and null circuits tell the computer when the servo circuits have moved the carriage and lens to a commanded position. The computer has the option of using the individual position plot outputs or of using a special signal (null)

generated when all position pot outputs are within a narrow range around the commanded position.

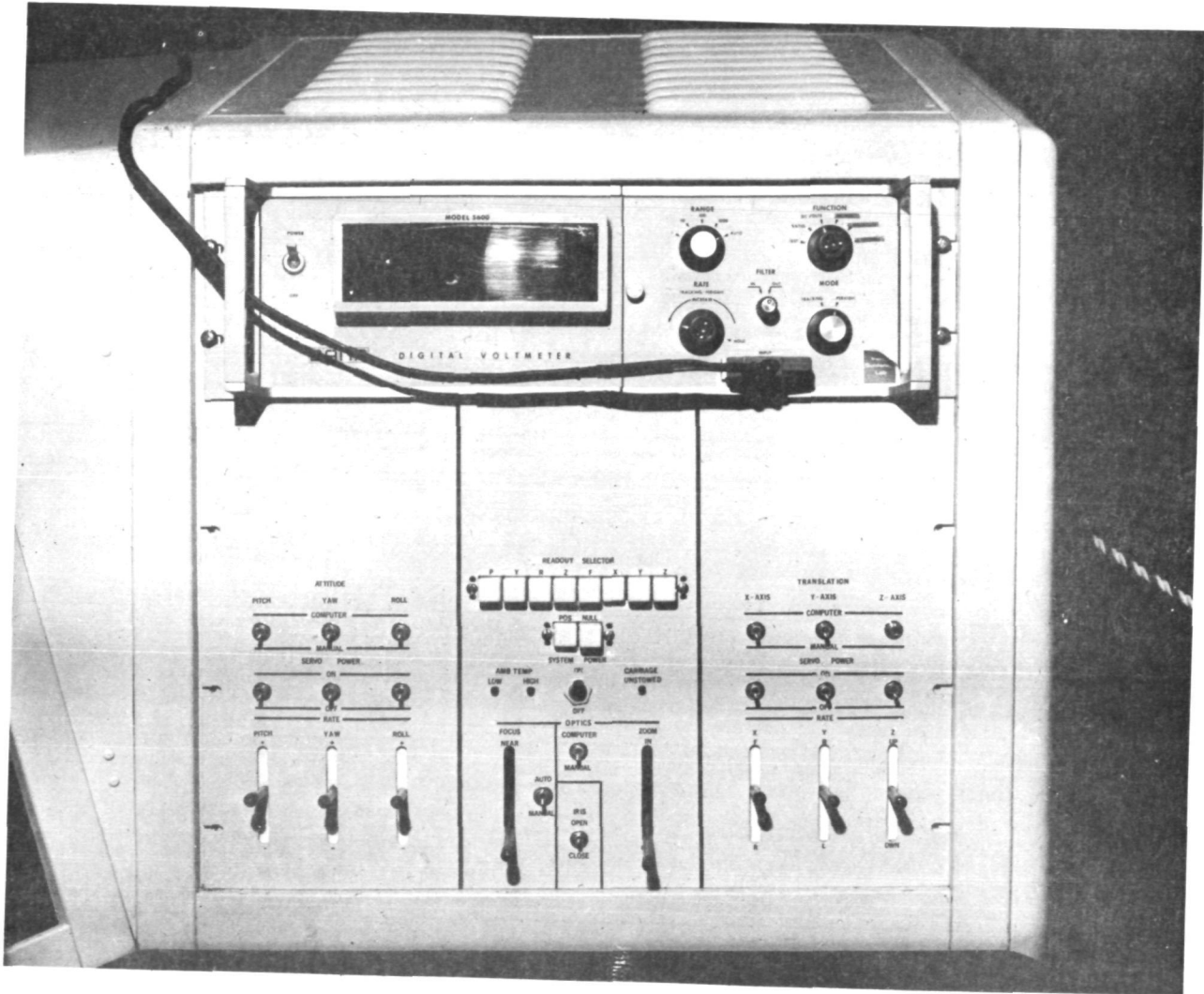


Figure 14 Simulator Control Panel

Computer Interface Circuits

The PDP-9 digital computer operates on voltage levels that are not always compatible with the digital and analog inputs and outputs of the simulator electronics. Both digital and analog interface circuits are employed to eliminate communication difficulties with the computer. Through the interface, the computer sends signals to: (1) control the sweep configuration; (2) restart or reset the sweep; (3) control the servosystems; and (4) blank the monitor. Through other interface circuits, the computer receives: (1) processed video; (2) position and null signals; and (3) sweep segment complete signals. Ultimate control of the computer is accomplished through a teletype terminal next to the control console.

Functional Description

The primary objective of the VGLIS concept is to generate algorithms for valid decision making based upon the information contained in a video signal. Since the requirements can vary quite widely, the video system should be versatile enough to accommodate most processing schemes with little or no modification. This section describes a sophisticated and versatile video system using a vidisector camera, an X-Y monitor, and a computer controlled digital sweep system.

The image dissector (Figure 15) was used in the breadboard system because of its adaptive sensing ability, photometric output, and controlled scan, which permits adapting to a change in scan position or lighting conditions on an instantaneous demand. Basically, it is a photomultiplier with a small, electronically movable photocathode area. An electron lens accelerates and focuses all electrons emitted from each point on the photocathode to a corresponding single point (or small area) in the plane of a dissecting aperture. The resulting electron image, which is a direct measure of the optical input radiation pattern, is then electronically deflected across the aperture. The aperture consequently samples, at any instant of time, the photocathode. Following the aperture, the sampled photoelectrons are multiplied in an electron multiplier by a large factor (commonly 10^5 or 10^7), and emerge as a current in the output anode circuit. Therefore, the detector output is a direct function of the light flux incident on the photocathode (image plane), and hence is a direct function of the illumination from the projected sample area on the surface.

Digital Sweep Circuits

The sweep circuit was designed to have all parameter variables

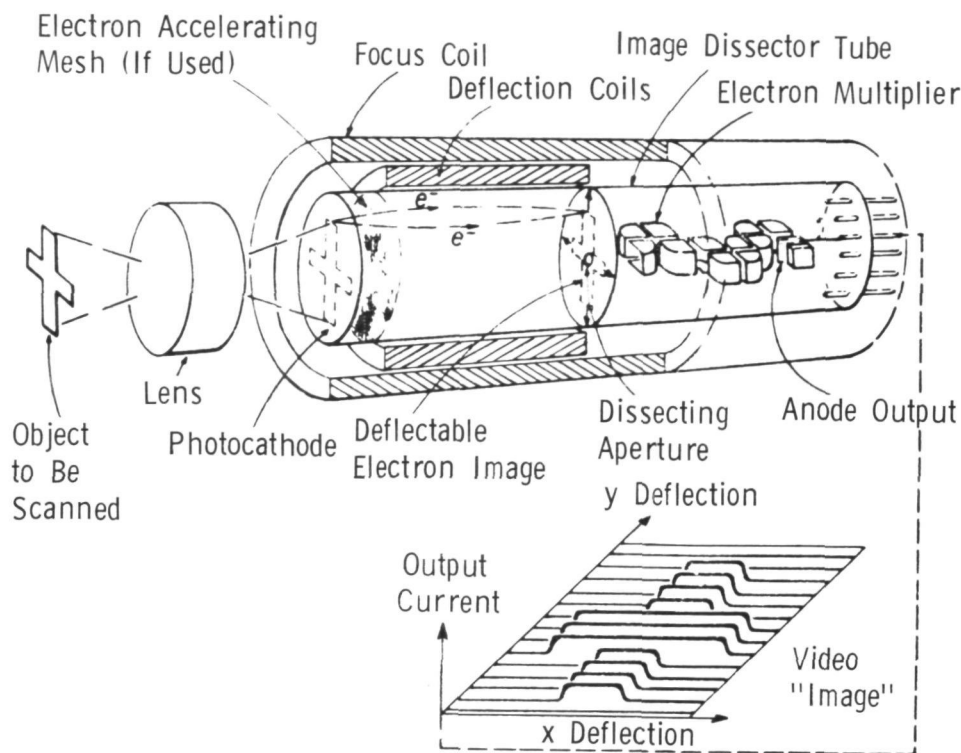


Figure 15 Image Dissector

with the capability for nearly instantaneous reconfiguration under computer control. The controllable parameters are the following: (1) frame rate, (2) frame partitioning, (3) horizontal and vertical electronic zoom (field-of-view), (4) raster orientation, (5) horizontal and vertical raster displacement, and (6) monitor blanking as illustrated in Figure 16.

The system timebase is a free-running 1.966 MHz crystal oscillator. The clock frequency allows a raster of 256 by 256 points to be scanned at a maximum rate of 30 noninterlaced frames per second. Although this rate allows for a good flicker-free picture on the monitor, it is somewhat above the system characteristics for best resolution. Therefore, a "max range" switch is provided on the control panel. In the 30 fps position, the 1.966 MHz signal is used directly; in the 10 fps position, a fixed divide-by-three counter is inserted to yield a clock frequency for a ten frame-per-second maximum.

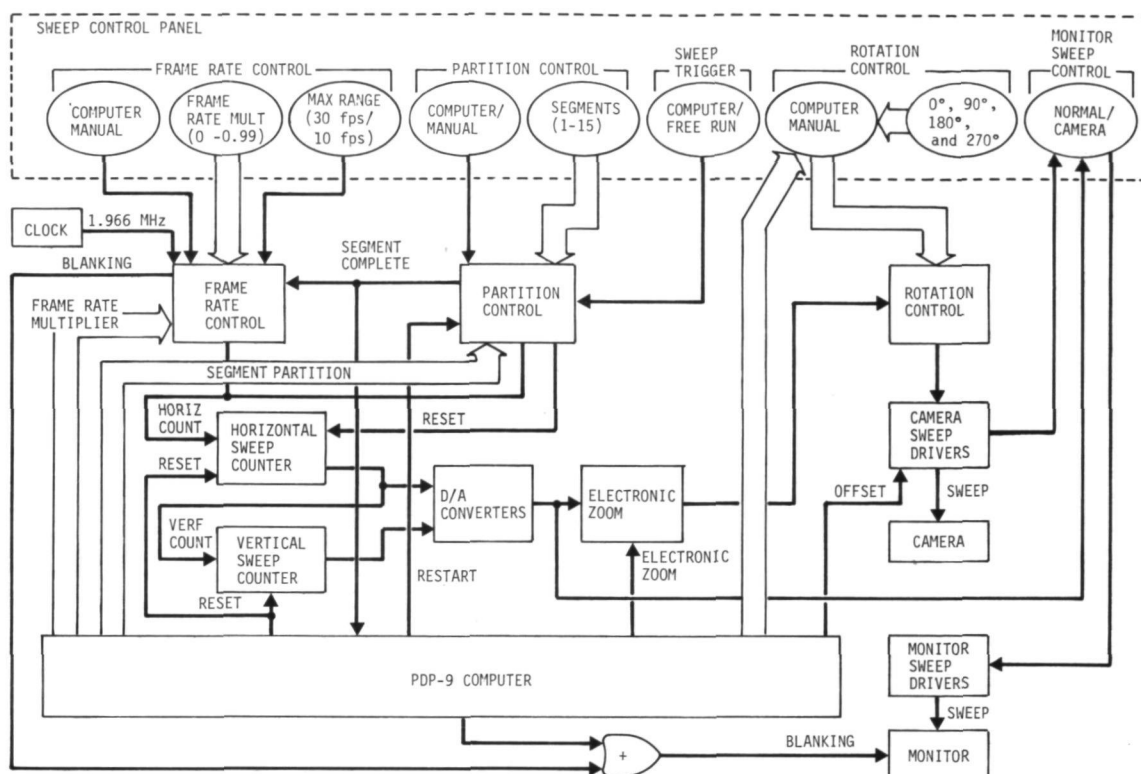


Figure 16 Digital Sweep Control System Block Diagram

The clock signal can then be multiplied by a multiple of 0.01 from 0 to 0.99. The multiplier can be set by a thumb-wheel switch on the control panel illustrated in Figure 17 or inserted by computer command with the computer/manual switch in the computer position. The total range in either case is 0.1 fps to 9.9 fps with the range switch on "10".

To break the total scan up into smaller areas (e.g., for figure-of-merit computation of each area for planetary landing simulations) the partition control circuitry can be used. That is, each horizontal line may be broken up into line segments and the video from each segment may be processed separately. The number of segments can be set from 1 (full line scan) to 15 in increments of 1. Again, the partitioning may be set by the computer or manually, depending upon the setting of the comp/man switch. Each segment is always exactly equal in length to the next regardless of the number of segments in a line. Although the maximum possible number of points scanned in a line is 256 (because the sweep is produced by an 8-bit counter), a line may consist of fewer points

depending upon the number of segments. For example, the highest multiple of 15 which equals 256 or less is 17. With the segment control at 15, the number of points scanned will be $15 \times 17 = 255$. Thus, the counter will produce 15 line segments of 17 points each and reset after 255 counts instead of 256.

The sweep trigger control permits either computer-controlled sweep or a free-running sweep. In the free-run position, a full-raster scan runs continuously at a rate specified by the frame rate control.

At this point, let us consider the generation of an analog sweep voltage. We will assume the sweep is free-running and not under computer control. The differences will be shown later. The clock signal is altered by the frame rate control.

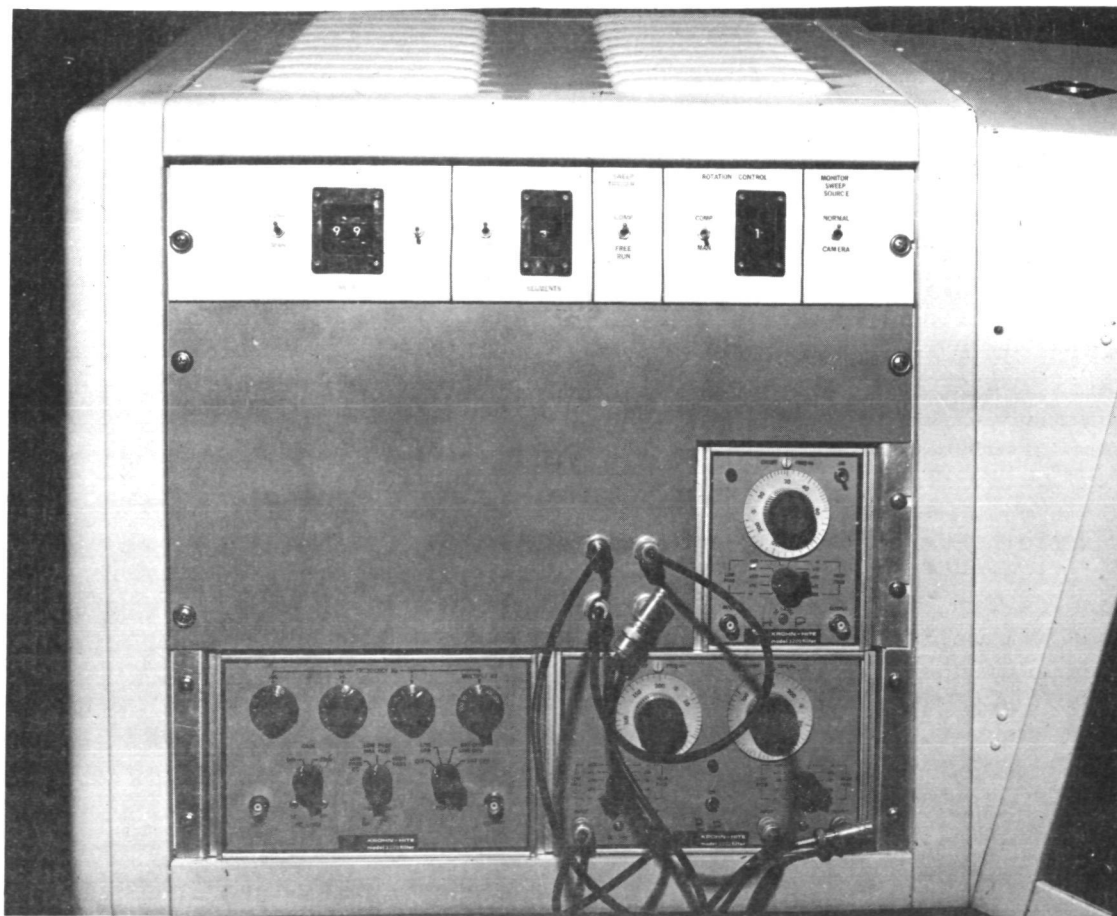


Figure 17 Sweep Control Panel

Each output pulse from the frame rate control causes the horizontal sweep counter to step one count. A horizontal D/A converter changes the count to an analog voltage that approximates a sawtooth sweep waveform. The sawtooth rises until the 8-bit counter reaches a count of 255. On the 256th count, the counter returns to zero as does the sweep waveform output from the D/A converter. Also, as the horizontal count resets to zero, the vertical sweep counter is incremented by one. The vertical sweep counter output also goes to a D/A converter that produces a vertical sweep sawtooth waveform in exactly the same way. In this manner, a raster of 256 by 256 points is generated. The D/A converter outputs are buffered and sent directly to the monitor when the normal/camera switch is in the normal position. The camera switch, however, undergoes three more modifications. First, the camera sweep amplitude is multiplied by an analog voltage from the computer. This sweep amplitude modification varies the camera field-of-view. If the monitor receives the full amplitude sweep (normal/camera switch in normal position), the effect on the screen will be that the camera lens appears to zoom in or out. Moreover, separate control of horizontal and vertical field-of-view is provided and the multiplication factors do not have to be equal in both axes. Next, the orientation of the image may be rotated in 90-deg steps. This is accomplished by interchanging the horizontal and vertical sweep signals and/or changing their signs. This rotation can be controlled by the computer through the rotation control's computer/manual switch or by a thumbwheel switch on the control panel. Third, the displacement of the sweep signals may be changed under computer control. Normally, the camera sweep is centered around 0 volts. However, with the introduction of analog offset voltages from the computer, the camera sweep will be centered around a different part of the photocathode presenting a different image. Following these three modifications, the camera sweep is buffered and sent to the camera. At this point, the second position of the monitor sweep source can be explained. If the switch is placed in the camera position, the monitor sweep will be identical to the camera sweep including the final three modifications. Thus, it is possible to see the results of these modifications by observing the monitor raster.

Monitor blanking is accomplished under computer or circuit control. Either source can produce blanking. If a visible trace or spot is to appear on the screen, neither source may command blanking.

To explain the computer-controlled sweep, assume that a 3x3 matrix (9 sub-frames) at 1 frame/second is to be scanned. The computer first sets the frame rate multiplier at 0.10 (range switch is on 10). Next, the partition control is set to 3. The computer then sends a reset pulse to set both the horizontal and vertical sweep counters to zero. To start the sweep, the computer sends a restart pulse to the partition control circuit. The activated partition control now causes the frame rate control to allow 1 count in 10 of the clock to appear at its output. These pulses are counted in two places. The horizontal sweep counter begins to count the pulses and produces an input to its D/A converter. At the same time, the partition control counts the pulses to determine when the end of a segment has occurred. In this case, the partition control is looking for the highest multiple of 3 less than 256. Since $3 \times 85 = 255$, the partition control will allow the sweep counter to count to 85. At this point, the partition control stops the frame rate control from producing pulses and signals the computer that it has reached the end of a segment. The computer then processes the video for that line segment and sends a restart pulse to continue the scan. The restart pulse resets the counter in the partition control but does not reset the horizontal sweep counter. During the second segment, the partition control counts from 0 to 85 and the horizontal sweep counter counts from 86 to 170. The process proceeds for the third line segment in the same manner and at the count of 255, both counters are reset and the vertical sweep counter is incremented. The computer counts the number of steps in the vertical sweep for vertical partitioning.

The above discussion shows the versatility of the system and the generation of a 3x3 subframe matrix. Any combination is possible from 1x1 to 15x256. The 3x3 matrix could also have been produced at higher resolution by shrinking the raster through the field-of-view control to 1/3 the full sweep in each direction, then scanning nine 1x1 matrices and using the offset control to place the small raster into the areas occupied by each 1/9th frame in the example. It is also possible to reduce the field-of-view to zero so that the raster becomes a "spot." Using the offset capability as an X-Y control, the spot may be moved anywhere on the photocathode.

Video Processing Electronics

A block diagram of the video processing electronics is shown in Figure 18. The video is applied to a differential

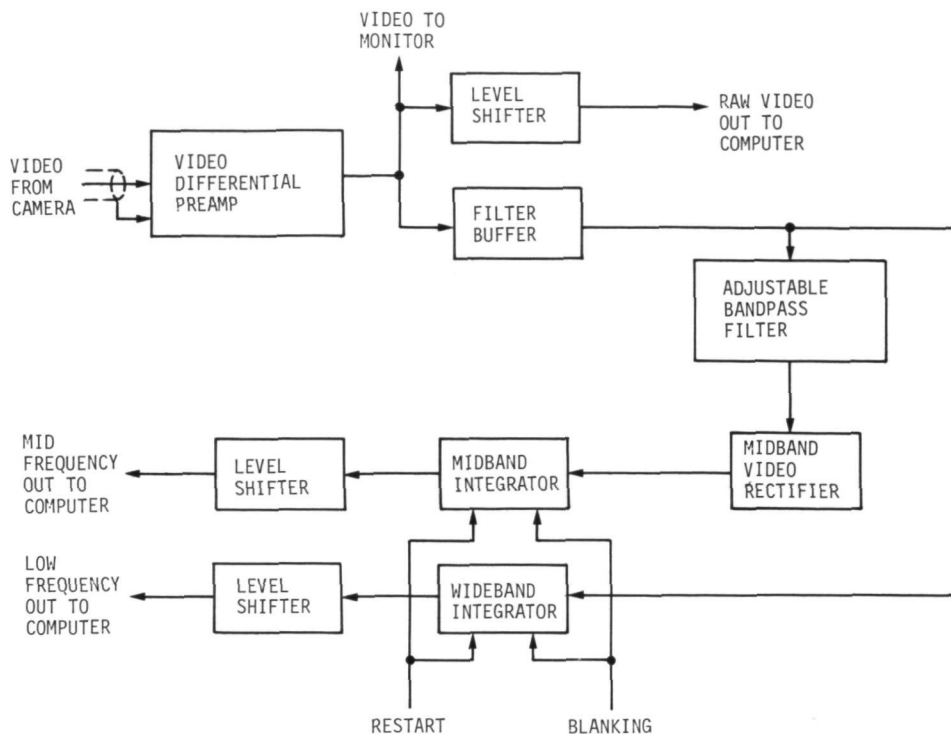


Figure 18 Video Processing Electronics

preamplifier to remove any common-mode noise produced on the relatively long cable run from the camera head. The amplified output is routed to the monitor video input for display. It is also offset and applied to the computer for applications requiring full bandwidth video. A third output from the preamplifier is buffered through a voltage follower. The buffer output is applied to an adjustable bandpass filter to remove the dc component and provide a selected range of frequencies for determination of spectral energy content. The filter output is then rectified and applied to an integrator. A second output from the filter buffer is sent to a second integrator. This raw video still contains the dc components of the camera signal. The integrators are operated in parallel by external signals. Integration takes place while the sweep circuits are scanning a line segment. At the end of each line segment, the sweep halts and a blanking signal is generated in the sweep control circuits. The blanking signal effectively disconnects the integrator inputs and the integrators go into a hold mode. The integrator outputs now are a dc level depending on the spectral content of the video from the preceding line segment.

The midfrequency output is proportional to the video signal components in the range of frequencies selected by the filter. The low frequency output is proportional to the average dc component of the video since the unrectified higher frequency components are effectively averaged out by the integrator. These outputs are level-shifted and sent to the computer for evaluation. Finally, a restart signal to begin the sweep again resets the integrators and the process begins again for the next segment.

Simulator Servosystems

The simulator carriage has a total of six degrees-of-freedom: Z (up/down), X (fore/aft), Y (port/starboard), yaw, pitch and roll. All degrees-of-freedom except for Z are moved by a single dc servomotor. Movement of the large boom ($\pm Z$) is accomplished by two servomotors, one at each end. The Z axis can maneuver the camera image plane between 1.52 and 3.35 m from the model surface. The X and Y axes have sufficient range to cover all parts of the surface.

Figure 19 is a simplified block diagram of a single axis of the carriage servosystem. Each translational axis has a position loop served by a single-position potentiometer and a rate loop, for improved stability, is provided by a tachometer.

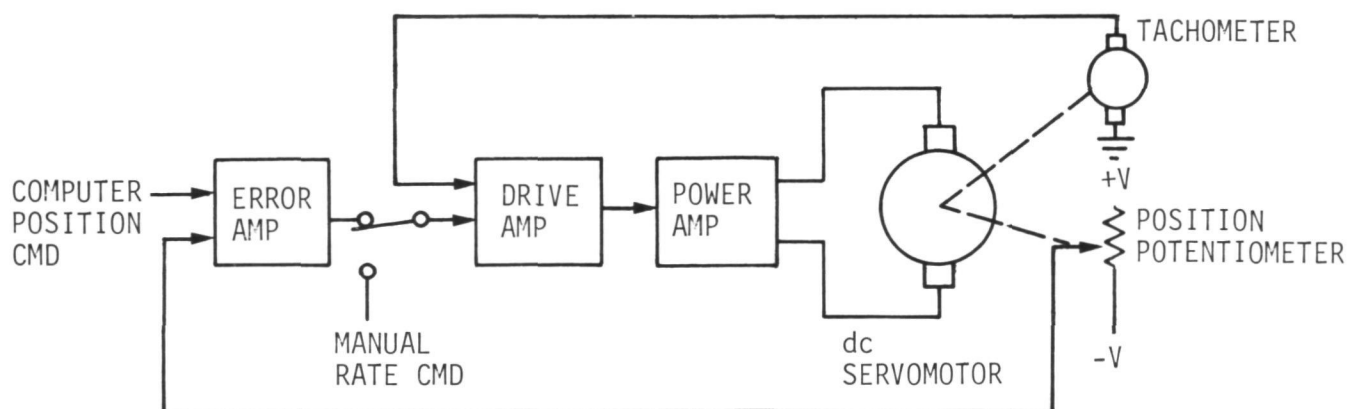


Figure 19 Carriage Servosystem Single-Axis Block Diagram

The Z-axis, having two motors, is operated as a parallel circuit with each amplifier receiving its position and rate signals from a single position potentiometer and tachometer. The Z-axis position potentiometer signal is also fed to the focus servosystem. The computer inputs to the carriage servosystem are position commands and manual control is by rate commands from the simulator control panel. The rotational servosystem is identical except that the rate feedback is not used and less powerful servoamplifiers are used due to the lower inertia and smaller motors employed.

The lens control system allows remote operation of iris, focus and zoom. The iris control is simply a manually operated front panel switch on the control console. No provision is made--or is necessary--for automatic iris operation. The zoom and focus servosystems differ from the carriage servosystems in one major respect: They contain diode function generators in the forward loop as shown in the block diagram in Figure 20. These function generators use a diode/resistor ladder network in the feedback loop of an operational amplifier to generate the desired nonlinear characteristic. The zoom network produces a linear change in focal length with input voltage. The focus network is coupled to the Z-axis potentiometer so that in the automatic mode the scene remains in focus regardless of altitude. The zoom and focus may also be operated manually through position controls located on the simulator control panel. The amplifiers are provided with electrical limits to prevent driving the lens beyond its normal end points.

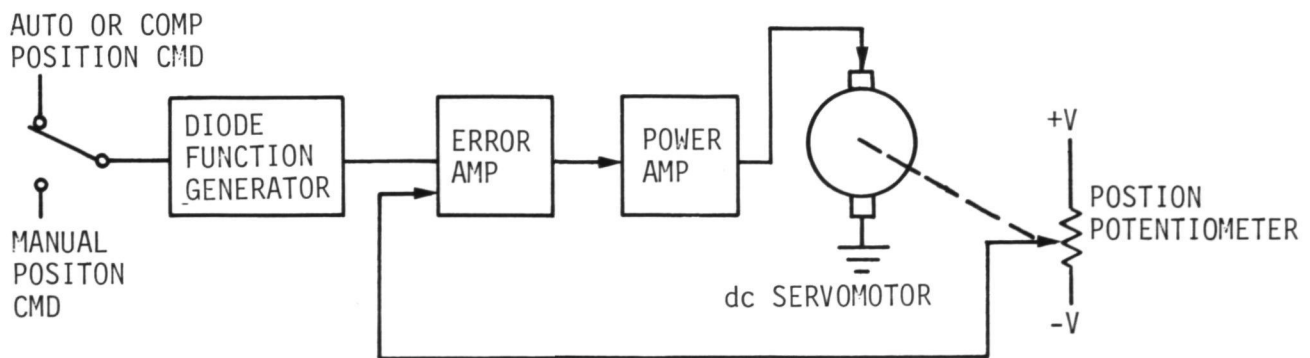


Figure 20 Lens Servosystem Single-Axis Block Diagram

Null Detector Circuits

This circuit is used to advise the computer that its commands to the simulator servosystem have been obeyed. Each servosystem provides a "null" signal that is the output of its error amplifier. This output will be near zero when the position potentiometer and the command input are in close agreement. In the null detector circuit, each null signal is compared to a reference of 0.6 V generated by a forward biased diode. When each of the seven null signals (X, Y, Z, pitch, yaw, roll, zoom) is within ± 0.6 V of zero, a null output will be generated.

Temperature and Stowage Warning Circuits

The VGLIS simulator is temperature-sensitive due to differing coefficients of expansion of dissimilar metals. Too low or too high an operating temperature can cause binding at the ends of the long boom. The laboratory is normally air-conditioned during operation to maintain a suitable temperature. Temperature warning circuits are used to indicate when the boom temperature is beyond normal limits. Thermistors, used as the temperature sensors and their voltage drops, are compared with an adjustable reference. If the temperature is too high, the upper-limit comparator will produce an output that lights a high-temperature limit LED on the simulator control panel. It also turns on a Sonalert for an audible alarm. A low-temperature alarm turns on a low-temperature LED and the Sonalert. To prevent temperature changes from causing damage during unattended periods, the Sonalert alarm is turned on if the main power is turned off when the long boom is not in its stowed position.

Computer Interface

Computer interface circuits are used on the ends of the computer/simulator cabling to ensure that signals are properly transmitted and received. Interface circuits are used for analog and digital signals.

Transmitting Interfaces

The VGLIS/PDP-9 digital interface takes a single-ended digital logic level and converts it to a pair of complementary, low-impedance drive signals. The VGLIS/PDP-9 analog interface circuits use an operational amplifier to invert the signal and offset it so that the output varies between 0 and -10 V, which

is the input range of PDP-9. If the analog signals are greater than ± 5 V, the input resistor would be increased to prevent the output from overdriving its range. The PDP-9/VGLIS digital interface uses a DM8820 line receiver to convert the unorthodox computer data bus output levels to the more standard 0 to +5 V. A DM8830 is then used to provide complementary line drive signals.

Receiving Interfaces

The digital input buffers use LM339 quad comparators. Since the lines are driven by complementary signals, the comparators switch states when the inputs switch states. The differential input eliminates problems due to ground potential offsets and common mode noise. The comparator outputs go from -15 to +15 V. To restrict the range of 0 to +15 V, a forward biased diode prevents the output from going more than 0.6 V negative. The 0 to +15 V range is compatible with the CMOS logic used in the sweep circuits. The analog input buffers are simply unity-gain stages with a differential input to reject common mode noise.

Simulator Software

A computer program was designed to allow the experimenter to control most of the system parameters through convenient data input formats and straightforward computer/simulator interfaces that were described in the previous section. The parameters that the experimenter can vary are illustrated in Figure 21, a sample of the teletype output. Following is a description of the variables.

XXXX	}	- Initial position, scaled meters
YYYY		
ZZZZ		
SEGS	- Partition selection, SEGS=3 means use 3x3 subframes partitioning	
RATE	- Scan rate multipliers	
SITC	- Site selection mode	
	SITC = 1 use minimum figure of merit	
	SITC = 2 use minimum row and minimum column figure of merit sums	

- FMNO - Figure of merit scheme number
- FOVU - Camera field-of-view (degrees)
- SCAN - Scan mode. This flag controls the display during an experiment. It permits a data taking only mode for rapid experiment performance or a variety of visual displays for demonstration, observation, and photographic recording.
- NOSC - Number of scans, variable to accommodate monitor photographs for recording experimental results.
- PRNF - Print flag to allow tabulation of video and position data for an experiment.
- STPS - Number of site selection decisions.
- CSTP - Step number to change from maximum figure of merit (scientific site selection) to minimum figure of merit (obstacle avoidance).

Once the landing commences, any of these variables, with the exception of initial position, can be changed to affect subsequent decisions or permit observation and data tabulation. This is accomplished by pressing the manual interrupt button on the console and following the teletype instruction. This program was then modified to include a Monte Carlo capability. The initial positions are selected by the computer. This Monte Carlo program served as the basis for most of the landing site selection experiments.

CURRENT INITIAL VALUES AND CONTROL DATA

XXXX	250.00	FMNO	6
YYYY	0.00	FOVU	17.24
ZZZZ	900.00	SCAN	0
SEGS	3	NOSC	25
RATE	20	PRNF	0
SITC	1	STPS	20
CSTP	0		

ENTER A 10-DIGIT RANDOM NUMBER

7645235476

WHAT IS FILE NAME

DATA 3

ENTER A 3 LINE TITLE

MONTE CARLO RUN 9/27/75 13:25

LIGHT ON GRATING 38 IN HIGH

3x3 min ROW, min COLUMN FIGURE OF MERIT

RUN NUMBER 1

INPUT DATA CHANGES

SCAN 3.

SITC 2.

CONT

LANDING NO. 1 INITIAL POSITION

430.85 -147.07 538.59

PUSH MAN INT TO CONTINUE

LANDING NO. 2 INITIAL POSITION

382.59 -187.83 567.64

PUSH MAN INT TO CONTINUE

LANDING NO. 3 INITIAL POSITION

400.12 -107.42 870.29

PUSH MAN INT TO CONTINUE

WHAT WOULD YOU LIKE

DATA

INTERMEDIATE DATA MODS

RUN NUMBER 1

SCAN 0.

CONT

WHAT WOULD YOU LIKE

CONT

LANDING NO. 4 INITIAL POSITION

444.55 -131.22 578.10

LANDING NO. 5 INITIAL POSITION

523.42 - 65.43 527.44

Figure 21 Monte Carlo Run

SURFACE MODEL

A typical surface model used in the feasibility demonstration consisted of a 2.44-m diameter octagonal box filled with 10.16 cm of lunar nominal NASA-furnished material, as shown in Figure 22. Another larger model used is shown in Figure 23. Surface morphology variations were implemented via the formation of craters, channels and channel outlets, volcanic structures, dunes, ripples and knolls. Multiple variations in surface granularity were accomplished by screening the model material to control obstacle distribution and to effect albedo variations. Subsequent sessions with members of the Viking Site Certification Group resulted in further refinements to the surface model. An attempt was made by Dr. H. Masursky, et al., to arrive at earth analogies of Martian features such as might be found in the dry valleys of South Victoria Land, Antarctica, or in the coastal desert of Peru.

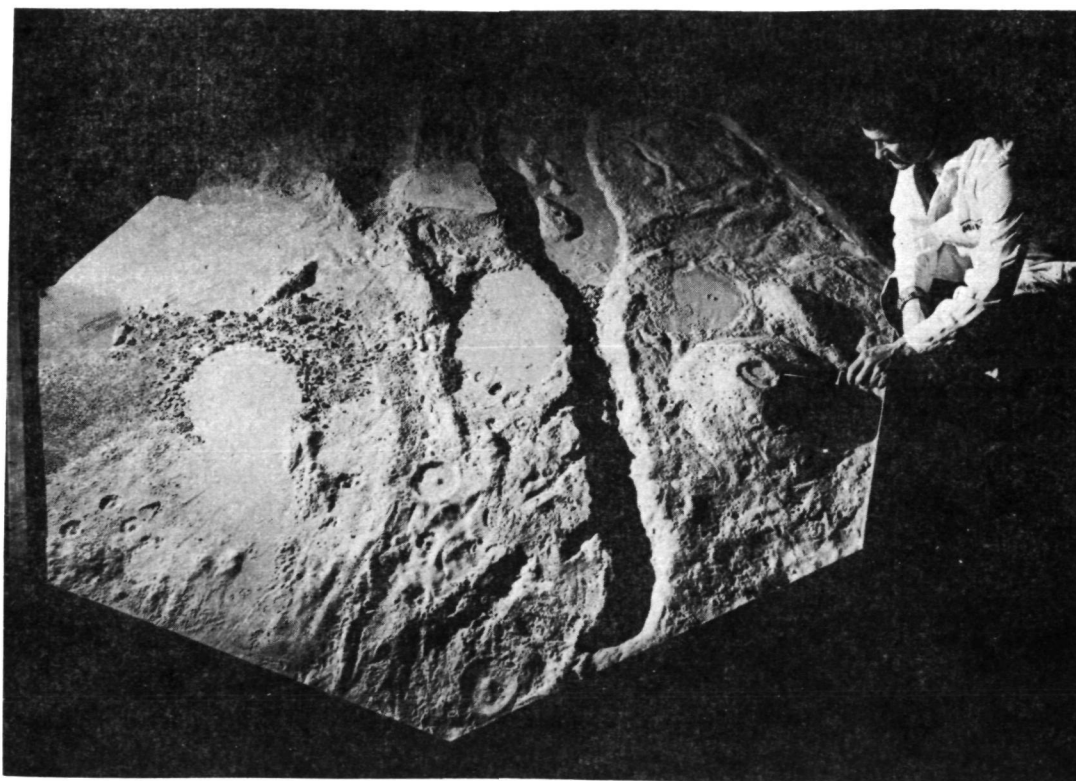


Figure 22 Scaled Surface Model

As an example, six of the seven types of wind erosional land forms recognized on Mars are present in the Peruvian desert. The clearly aeolian light and dark plumes on Mars have Peruvian counterparts. The morphology of the Martian dunes resembles that found in Peru. It has been inferred that both small- and large-scale sand and possibly granule ripples also exist on the surface of Mars, but were not seen because they were below the limit of the Mariner 9 cameras. Dark lag gravels of desert pavements are almost surely present.* Selected photographs of areas of interest are shown in Figure 24.

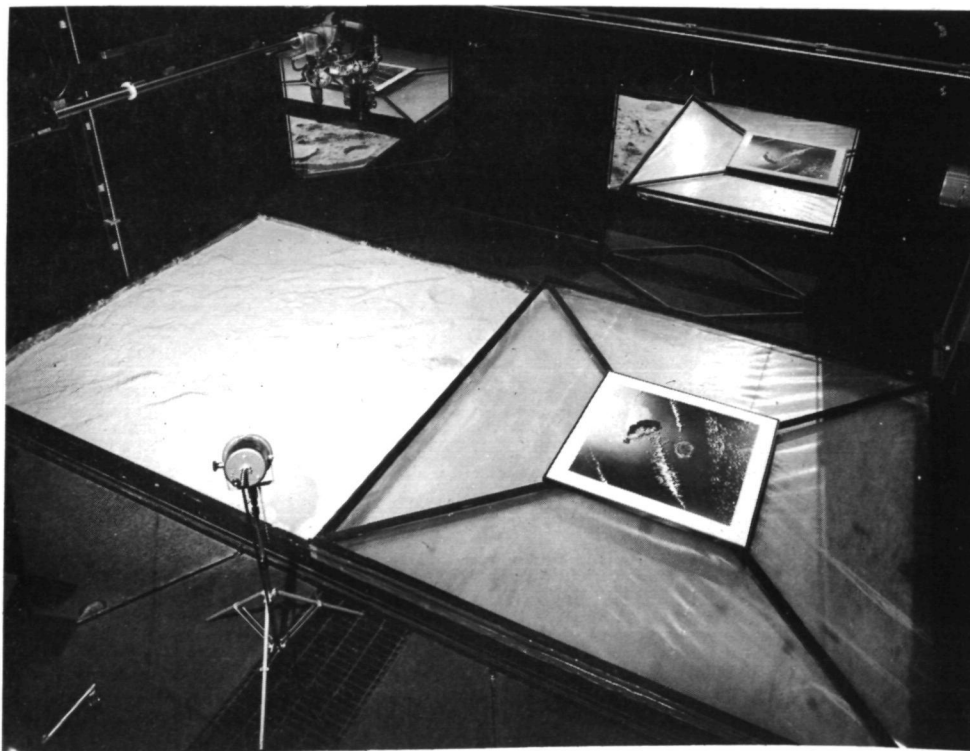


Figure 23 Scaled Surface Model and ERTS Photograph

*Grolier, J. J., Ericksen, G. E., McCauley, J. F., and Morris, E. C., "The Desert Land Forms of Peru: A Preliminary Photographic Atlas." U. S. Department of the Interior Geological Survey, Interagency Report, Astrogeology 57, February, 1972.

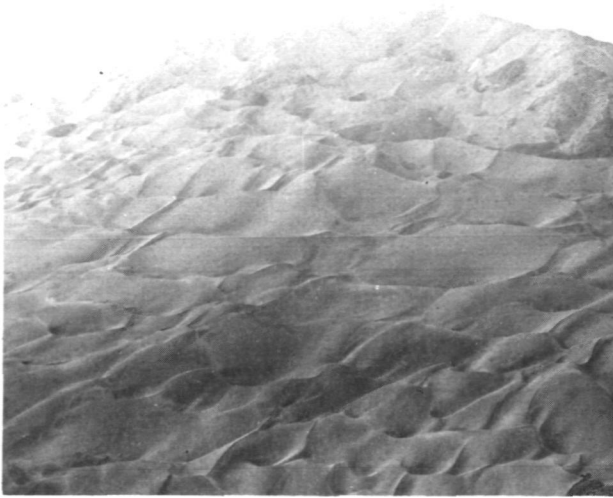


Figure 24 Desert Land Forms of Peru

Still other Martian analogies can be made to the Dry Valleys of South Victoria Land, Antarctica. Implications for a Viking-type lander are as stated by Morris, Mutch, and Holt.*

*Morris, E. C., Mutch, T. A., and Holt, H. E., "Atlas of Geologic Features in the Dry Valleys of South Victoria Land, Antarctica.: U. S. Department of the Interior Geological Survey, Interagency Report, Astrogeology 52, September, 1972.

"Various features seen in the Dry Valleys may be similar to features that might be encountered on Mars." Having some understanding of this terrestrial cold desert region, our capability for prediction and interpretation is increased. Some examples are as follows:

- (1) Cavernous weathering of boulders produces strange forms that, in low-resolution photographs, could easily be taken for artifacts or biologic forms;
- (2) Cavernous weathering characterizes a cold, windy environment, but similar erosional forms can be produced in a variety of terrestrial environments.
- (3) Ventifacts can be formed in brief periods of time--months to decades. Orientation of facets provides a record of prevailing wind direction;
- (4) Erosional and depositional features in the vicinity of boulders provide a record of recent wind direction;
- (5) Cavernous weathering occurs in coarse-grained rocks. Fine-grained rocks form classical ventifacts;
- (6) Winds in the vicinity of 200 km/hr can form pebble ridges;
- (7) Armored pavements of coarse fragments, formed by deflation of fine materials, are common in the Dry Valleys and in many other desert regions. The pavement can be easily penetrated to obtain underlying finer sediment;
- (8) Antarctic soils are very poorly sorted with a marked deficiency of fine clay material relative to most other terrestrial soils and sediments;
- (9) Physical disaggregation of rocks to produce the forms observed in the Dry Valleys probably involves frost shattering;
- (10) Patterned ground is produced when an ice layer is situated within several meters of the surface;
- (11) The size of ice wedges and the amount of ground deformation adjacent to them is related to their age;

- (12) Moist soil overlies permafrost, even though little or no moisture is derived from the atmosphere;
- (13) Concentrations of salts occur throughout the soil in this cold desert region;
- (14) The geochemical significance of the salts is difficult to establish;
- (15) Weathering of bedrock involves little chemical modification;
- (16) Interbedded aeolian sand and snow produce lithified strata that closely resembles more common bedded sedimentary rocks;
- (17) Sand dunes accumulating when temperatures are slightly below freezing are characterized by snow-sand cornices building out over the lee slopes of dunes;
- (18) Most of the large boulders observed throughout the Dry Valleys have been transported to their present sites by glaciers. (There is no evidence for a similar transportational environment on Mars, at least in the Viking zone of interest.)

EXPERIMENTAL RESULTS

This section summarizes the calibration technique and experimental data resulting from multiple flights to the surface via the laboratory system described in the preceding section.

The optical calibration phase consisted of several experiments designed to characterize actual system performance. These experiments resulted in an estimate of video system performance; i.e., a measure of the system's ability to "see" a given target.

Feasibility was demonstrated by applying statistical analysis, where applicable, to the experimental results discussed in this section. A Monte Carlo approach was used, with "flights" starting with random initial conditions. This provided a quantitative basis for evaluation of performance capability.

Camera Calibration and Checkout

Tests of the VGLIS camera system and of its components have been made for the purpose of determining their operating parameters, checking their performances, and predicting the overall operation of the system in its various configurations. These tests will be described briefly in the following paragraphs.

Modulation Transfer Function (MTF) - The modulation transfer function, as applied to the VGLIS, is a curve that shows the modulation transfer of the system or one of its components (lens, imaging tube, electronic circuits, or complete system) as a function of the spatial frequency of information in the scene viewed by the camera. The modulation transfer for any specific spatial frequency is determined by viewing a target that is produced and calibrated to present a known contrast at that spatial frequency. The modulation transfer for that frequency is then the ratio between the contrast indicated by the system's or component's output and the known contrast of the target.

Several of the elements that affect the MTF are as follows:

- (1) Zoom lens - The performance of the laboratory system compared to what could be achieved in the flight situation is considerably degraded by the necessity to employ the servo-controlled zoom lens. Such a lens possesses an infinitely large family of MTFs that

depend on the zoom focal length, position in the field, and object distance. Aperture vignetting is also a problem that varies with focal length. Finally, there are practical problems in precisely mounting the lens on the camera so an optimum focus exists over the full range of focal lengths, and then to correctly adjust the analog function generator to maintain focus as the camera moves up and down;

- (2) Camera - The MTF performance of the image dissector camera is primarily governed by the size and shape of the scanning aperture, with the electron optics being a secondary influence. Although the MTF of the camera also varies with radial position off-axis, in the present case, the maximum radial offset is only about 60% of the capability of the tube so this variation is minor;
- (3) Signal processing electronics - Video signal amplification by the image dissector multiplier section is very broadband, as are the current-to-voltage and line-driving voltage-follower amplifiers contained in the camera assembly. The MTFs of these stages can be ignored. Each spectral band of the contrast avoidance logic will be represented by a different MTF, but as far as the signal delivered to the logic is concerned, the rolloff of the initial low-pass filter is the dominant factor electrically.

The influence of the above factors is shown in Figure 25. Because much of the experimental work in this phase of the program was performed at an optical object distance of about 3.35 m, the scale of the abscissa has been chosen appropriately. All MTFs have been projected back into object space (i.e., the plane of the terrain model) using a magnification that reflects the 3.35 m object distance and the maximum focal length used (about 120 mm). All of the component MTFs shown (for camera, lens, and low-pass filter) are estimates. In the lens case, the estimate is not the worst case because it does not affect the maximum radial off-axis position.

The estimated system performance shown is the product of the other three MTFs. Also shown, is a curve representing appropriately scaled high-contrast 22-cm target as seen by a possible flight camera from a distance of 50 m.

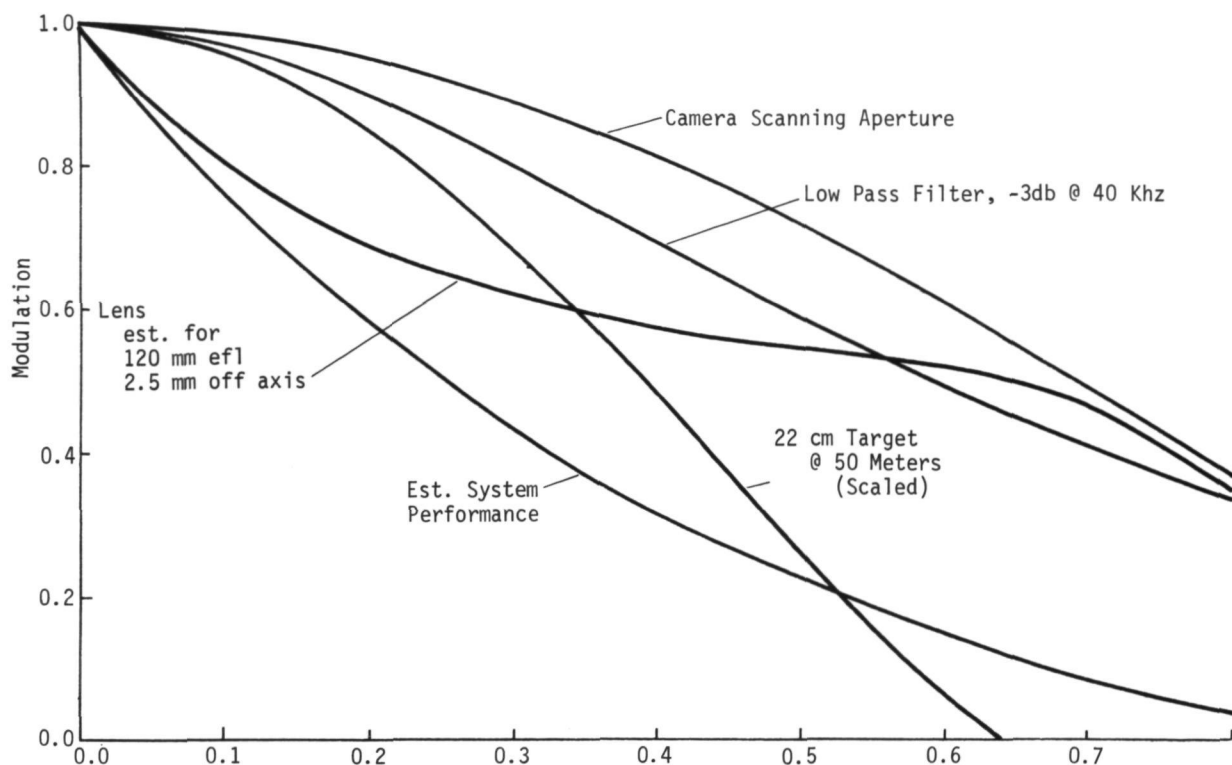


Figure 25 Spatial Frequency in Object Space, $l\ p/mm$

Camera and Preamplifier - The television camera used in the VGLIS is an image-dissector camera produced in October, 1973 by International Telephone and Telegraph Corporation, Fort Wayne, Indiana. During the course of the VGLIS experiments, it became desirable to check for possible degradation of the performance of the camera itself.

To accomplish this purpose, the lens assembly was removed from the camera, and the photocathode of the image dissector tube was flooded with a uniform light whose intensity was measured to be about 36.5 ft-c. With this illumination and with the proper input voltages and scanning currents applied to the camera, the voltage appearing at the output of the camera's preamplifier was measured. The output was found to be 0.049 V/ft-c illumination. This output agreed with the results of a nearly identical test performed before delivery of the camera to Martin Marietta. No camera degradation was found.

An additional test performed in the same setup, confirmed that the camera is essentially shot-noise limited, as expected, and that its signal-to-noise ratio has not varied appreciably since its manufacture and is within design limits.

Camera Photocathode Uniformity - In another test, the photocathode of the camera's image dissector tube was uniformly illuminated and the amplitude of the camera's video signal was measured as a function of the location of the scanning spot on the photocathode. It was found at the time, that there was a coupling between the current in the scanning circuits and the video signal. This coupling has since been removed, and the sensitivity of the camera appears uniform within design limits over the scanned area of the photocathode.

Zoom Lens Operation - Since the laboratory VGLIS camera is equipped with a zoom lens, and it is used in a setup where the viewed scene is relatively close to the camera and its lens, the actual magnification obtained for a given scene depends on both the object-to-image distance and the effective focal length of the lens at the time. In order to allow approximate calculation of the actual magnification, the locations of the two nodal points of the zoom lens were determined as functions of the lens effective focal length, for object-to-image distance of 99 in. (2.51 m). The result is shown in Figure 26.

Algorithm Evaluation Experiments for Planetary Landers

The basic technique of comparing the ac portions of the video signal in various parts of the spectrum, with the dc portion of the signal allows for an infinite variety of algorithms for rating each scene with a "figure of merit" for landing site suitability. Several questions must be answered before the technique can be reduced to hardware. The questions are as follows:

- (1) How should the signal components be compared?
- (2) Into how many bands should the spectrum of the video signal be divided?
- (3) How should the spectral components of the signal be measured--peak-to-peak, rms, absolute average, or some other way?

- (4) How should the comparisons at different parts of the spectrum be combined to get one figure of merit-- linearly or nonlinearly? And, if the combination should be nonlinear, how should it be done?
- (5) What weighting factors should be attached to the various spectral components? Should the weighting factors be a function of altitude?
- (6) Does an "optimum" system for distinguishing good areas from bad offer any significant advantage over a significantly simpler system? At what point do further improvements cease to be cost-effective in terms of mission success probability?

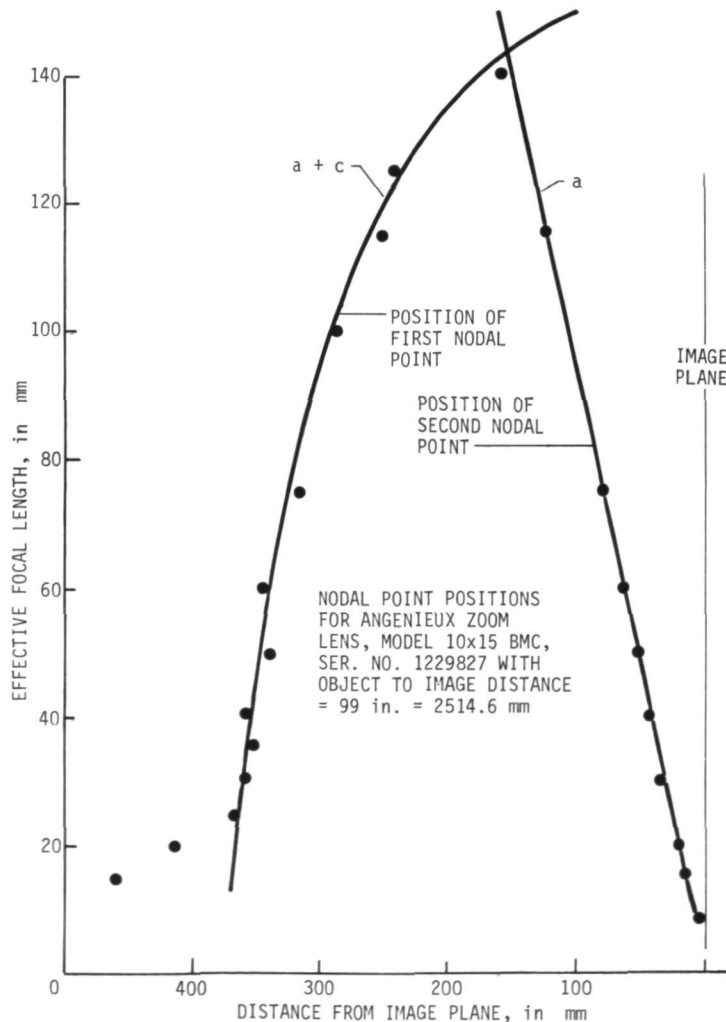


Figure 26 Zoom Lens Characteristics

Although it was not possible to give definitive answers to all these questions, each was addressed in designing the breadboard system. As will be shown later, the experimental results suggest that good results can be obtained even when these questions are answered in terms of practicality, cost, flexibility, and impact on existing spacecraft and laboratory hardware.

Having calibrated the system, the algorithm evaluation experiments were performed to establish site-selection feasibility. In performing these experiments, consideration was given to spectral band selection, weighting factors, altitude versus resolution effects, combining of filtered outputs, and scan mechanization.

The first approach considered was a time-domain technique in which an ac component was monitored to determine the amount of time the voltage was above a threshold compared to the amount of time it was below the threshold.* Under near-ideal lighting conditions, the approach worked well with fairly simple hardware; but when lighting variations were introduced on a three-dimensional model, the ratings did not always correlate well with site desirability. When methods for reducing sensitivity to lighting were considered, the required hardware became significantly more complex; therefore, the approach was modified.

When a camera with a linearly responding photocathode is used, the ratio of the ac component in the video signal to the dc component is approximately constant for a given scene over an "illumination" range of more than 4 to 1. The ratio of the ac and dc voltage output then would provide an index of surface roughness that is independent of scene brightness. This is the approach used in the following experiments.

Experiments were conducted to determine what frequency ranges best distinguished high-contrast targets from low-contrast targets.† Preliminary results indicated that certain rough areas

*Schappell, R. T., and Johnson, G. R., "Experimental and Simulation Study Results of a Planetary Landing Site Selection System," J. of Spacecraft and Rockets, Vol. 10, No. 4, April, 1973.

†Schappell, R. T., Knickerbocker, R. L., Tietz, J. C., Grant, C., Fleming, J. C., Video Guidance, Landing, and Imaging Systems for Space Missions, Final Report, NASA-CR-132574, February, 1975.

were best distinguished from others in the bands from 30 Hz through 9 kHz and from 1 through 30 kHz. These bands were, therefore, used in the experiments. The ac components of the signal were measured with circuits that respond to average absolute value because of the circuit simplicity. Therefore, the figure of merit (FOM) was derived in the following manner:

$$\text{FOM} = a \left(\frac{\left| \bar{V}_M \right| - b}{\left| \bar{V}_L \right| - c} \right) + \left(\frac{\left| \bar{V}_H \right| - d}{\left| \bar{V}_L \right| - e} \right)$$

where \bar{V}_M , \bar{V}_H , and \bar{V}_L are the midband, highband, and dc-component average absolute values. The constants b, c, d, and e were introduced to correct for noise and offset voltages so that the ratio would be constant for a given scene regardless of light level variations caused by laboratory limitations.

Figure 27 illustrates actual experimental results using this algorithm and a 3x3 subframe scan. This sequence of pictures was taken from the console television monitor. In actual operation, the nine subframes were scanned sequentially. After each scanning sequence of nine subframes, the subframe with the least amount of contrast was selected as the desired landing site.

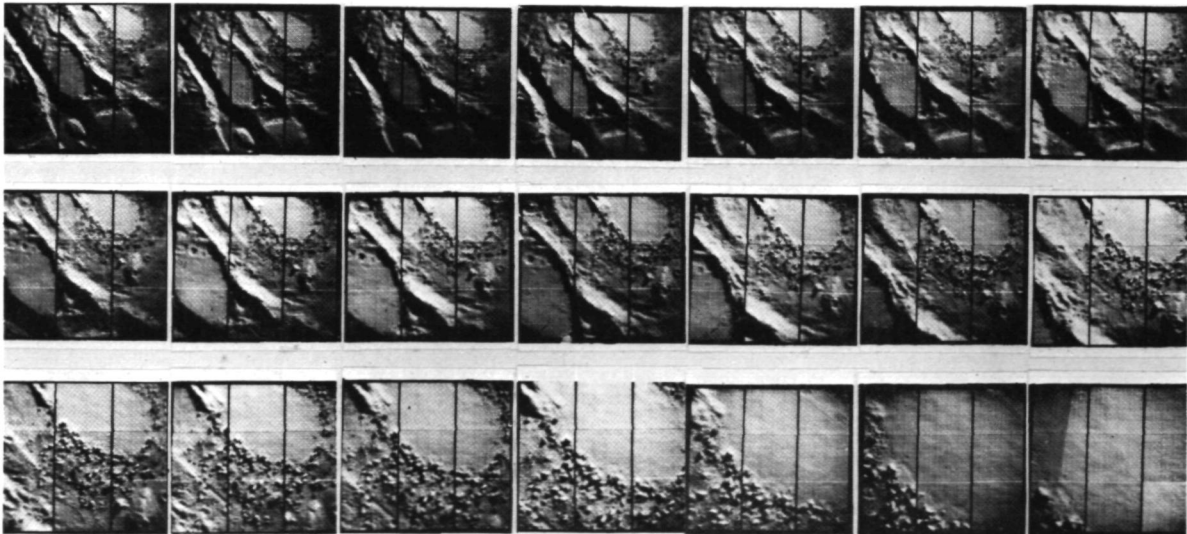


Figure 27 Monitor Observations for a Typical Experiment at 1-sec Intervals

The final site (the center of the last photograph) was the result of 20 observations and decisions.

The next series of experiments was a Monte Carlo experiment in which the system computer was programmed to select an initial simulated altitude between 500 and 900 m and an initial X, Y position above the three-dimensional Martian surface model at random using a random number generator. It then calculated altitudes and predicted impact points for the lander as it approached the surface under system guidance. The computer received guidance information 20 times during the descent. When the simulated altitude reached 100 m, the predicted impact point was recorded on tape. The 50 landing sites selected during a Monte Carlo run are indicated by the small ovals in Figure 28.

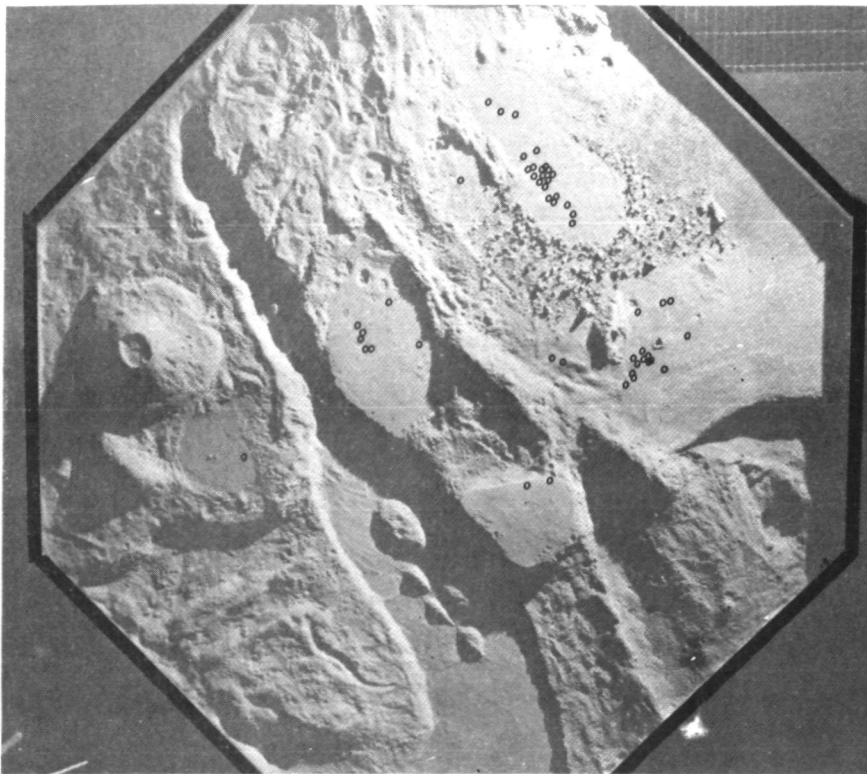


Figure 28 Monte Carlo Experiment

To provide a comparison for estimating success probability, unguided simulated landings were also run. The total experiment was automated and set up in a manner that eliminated experimenter bias through the use of additional experimenters. The results obtained from the initial preliminary experiments indicated that, without the VGLIS logic in an unguided situation, nine out of 48 landings would have been successful, but with the VGLIS logic in a guided mode, the system always avoided extremely rough sites even though initial position and altitude did not always provide a field-of-view with a distinctly smooth area. For these experiments, Sun angle was 60 deg from normal to the surface, and the guidance mode limited the landing site to the area defined during the first high-altitude observation.

Experiments conducted using the model shown in Figure 28 indicated that system performance was very insensitive to weighting factors in the figure of merit equation. No advantage was found in dividing the signal spectrum into segments, but a ratio of ac signal voltage to the dc component provides an excellent figure of merit. Therefore, a new signal processing circuit was designed and built to allow simultaneous scanning of all subframes in a row. The new circuitry was more flexible because it permitted the user to select the number of subframes per scan with up to 225 subframes per picture. Selection could be made manually with a front-panel switch or by computer control. The principle of operation, however, remained the same.

As previously discussed, a larger surface model was built based upon suggestions from scientists involved in planetary geology and site selection. Compared with the previous model, it is a relatively benign surface in the sense that it has fewer gross geologic features and a much larger percentage of the surface devoted to fairly good landing sites. The model was designed to represent typical terrain in an area of scientific interest as far as current knowledge of features at this scale permitted. To scale, the model represents an area approximately 500,000 sq m on Mars. This model is shown in Figure 23.

Using this model and the new signal processing electronics, experiments were performed to answer the following questions:

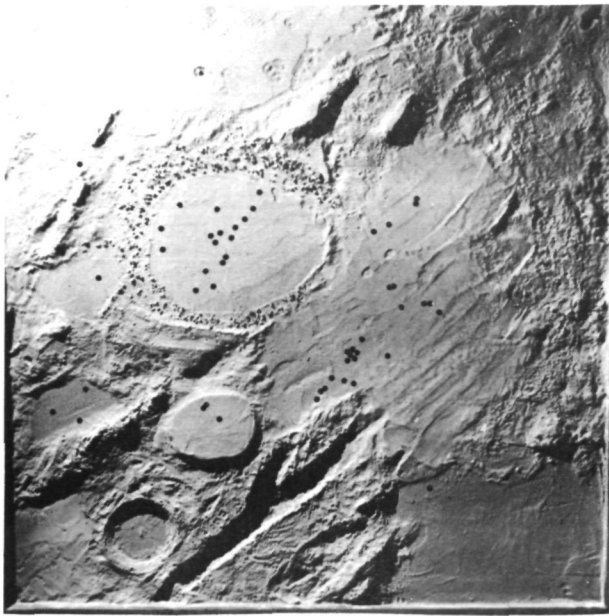
- (1) How many subframes should be used in making each guidance decision?

- (2) Should the guidance decisions favor the best subframe of each complete scanning or should the lander aim instead at the intersection of the best row of subframes and the best column of subframes? The latter would provide acceptable alternative sites if a site that looked good at high altitude proved to be poor on closer inspection.
- (3) Can the system increase the probability of landing in a scientifically interesting area if the first five guidance decisions steer toward the worst area and the remainder of the decisions avoid contrast in the normal manner? Will this greatly reduce the probability of mission success?
- (4) What field-of-view maximizes success probability?
- (5) What sun angle maximizes the probability of mission success with this guidance technique, and how does success probability vary with sun angle?

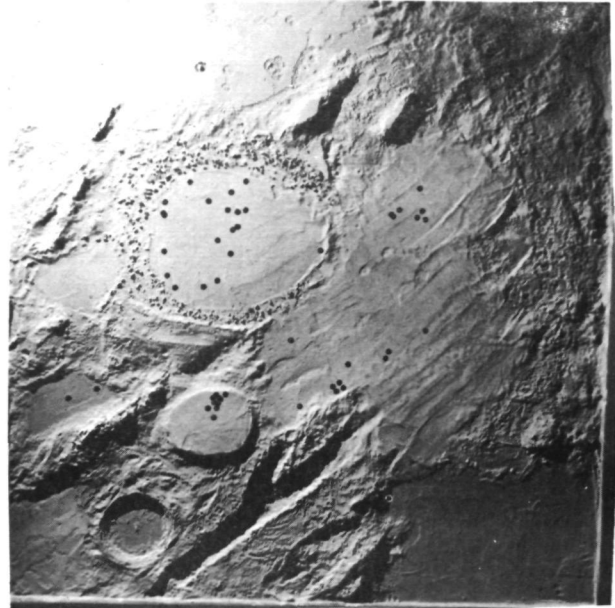
A Monte Carlo technique was used to answer these questions because an analytical solution was a formidable task that would require a number of gross assumptions about surface conditions and other unknown factors. The Monte Carlo technique also includes factors such as camera noise and other physical equipment limitations that might have to be left out of an analytical model to make the solution manageable or which might incorrectly be assumed to be inconsequential. In all cases, the computer used a random-number generator to select an initial location over the model and an initial simulated altitude between 500 and 900 m for each simulated landing.

Subframe Size and Best Row/Column versus Best Area Experiments

To assess the effects of varying matrices of subframes, 50 landings were simulated using 9 subframes, and another 50 landings were simulated using 25 subframes per decision. The sites selected are shown as black dots in Figure 29 (a) for 9 subframes and Figure 29 (b) for 25 subframes. At each decision, the lander was steered toward the best subframe. Figure 30 shows a second set of experiments in which the lander was steered toward the intersection of the best row and best column of subframes. Performance appears to be somewhat better when the lander is simply guided to the best single subframe. More successful results were achieved by selecting the best single subframe, since it does not

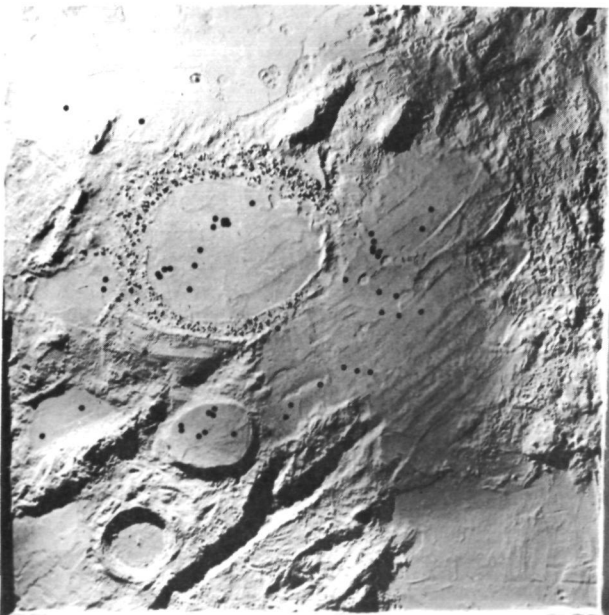


(a) 3x3 Matrix

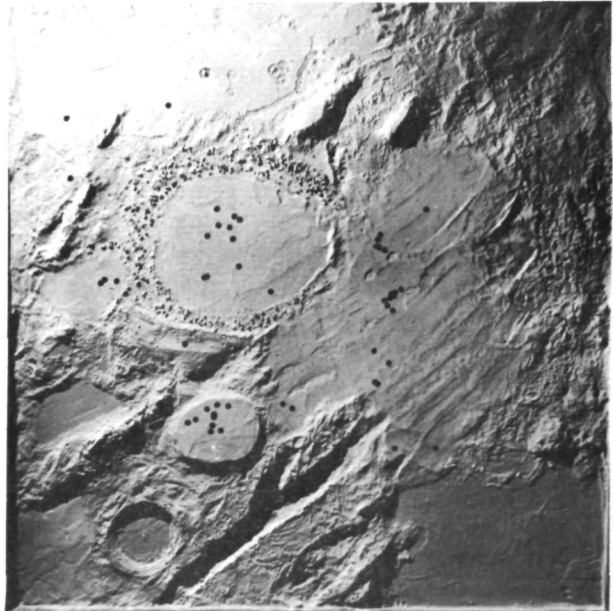


(b) 5x5 Matrix

Figure 29 Monte Carlo Run - Subframe Size
Experiment with Best Area Selected



(a) 3x3 Matrix



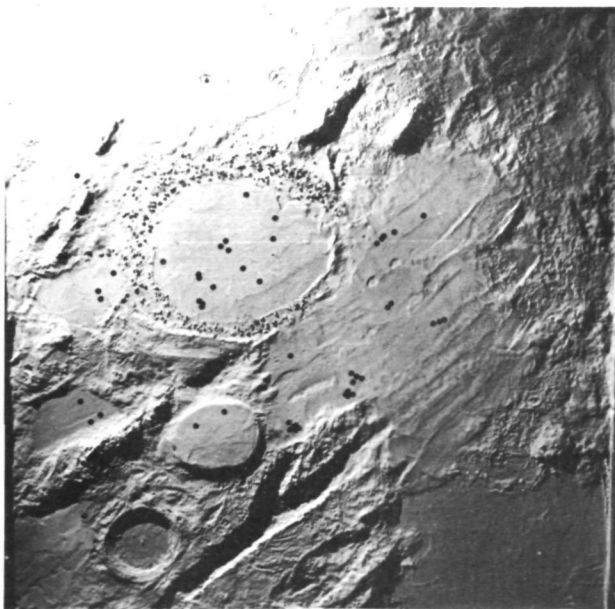
(b) 5x5 Matrix

Figure 30 Monte Carlo Run - Minimum
Row/Column Steering

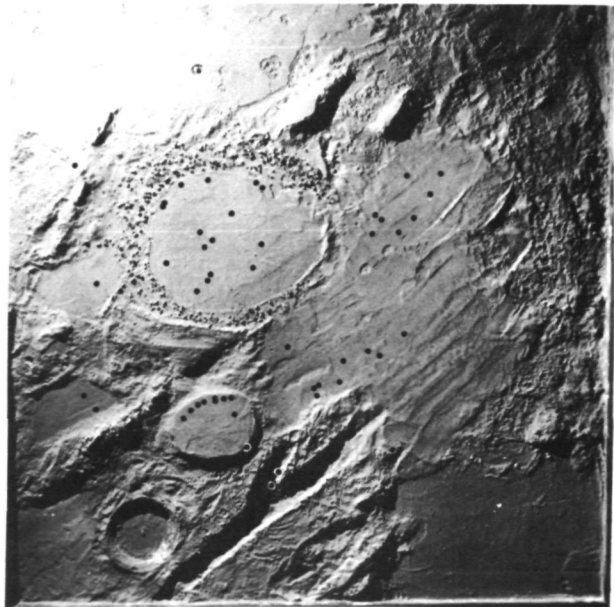
necessarily follow that the intersection of the best row and column will be a good site itself and since the experiment does not show that sites selected at high altitude frequently prove to be poor on closer inspection.

No clear advantage was found in increasing the number of subframes beyond nine. In both cases, when guidance was toward the best subframe, one questionable landing site was selected out of 50, and this site was poorer where 25 subframes were used. Since increasing the number of subframes tends to make the system more complicated, increase the burden on the lander computer somewhat, and slow down operation of the system, it appears that the optimum system would use no more than nine subframes per decision.

Scientific Site Selection Experiments - Figure 31 shows the results of an experiment in which the first 5 observations result in guiding the lander toward the worst subframes, and the remaining 15 observations aimed toward the best subframes. The intent was to increase the percentage of landings in scientifically interesting areas, which tend to be somewhat chaotic.



(a) 3x3 Matrix



(b) 5x5 Matrix

Figure 31 Monte Carlo Run - Scientific Site Biasing

As expected, especially when 25 subframes were used per decision, there was an increase in the number of scientifically interesting sites selected. However, the lander tended to get so far into bad areas that it could not find a good landing site. This resulted in a marked increase in the number of marginal sites selected. In many cases, sites nowhere near "scientific" terrain were selected because of maneuvering distance limitations. The results of these experiments suggest that the system could best be used to increase success probability in an area known *a priori* to be interesting.

Field-of-View Experiments - All the experiments discussed so far used a 17.36 deg field-of-view. To find out what would happen with a smaller field-of-view, one experiment was conducted with an 8.68 deg field-of-view. The results were dramatic--since navigation was constrained to the area seen in the first scanning of the subframe, many landings resulted in crashes. The lander simply could not find an acceptable site with this small a field-of-view. This suggests that the field-of-view should be as large as possible, consistent with other requirements such as resolution, electronic gimbaling, etc. The 17.36 deg field-of-view was based on these criteria, but the exact upper limit would depend on the characteristics of the vehicle used. Success probability for a given field-of-view depends on the size of gross terrain features with respect to the lander. The data sent back from Viking '75 should be invaluable in refining the estimated optimum field-of-view, but it is expected that 17.36 deg will not prove to be greatly in error. Selected sites with the narrow field-of-view are shown in Figure 32.

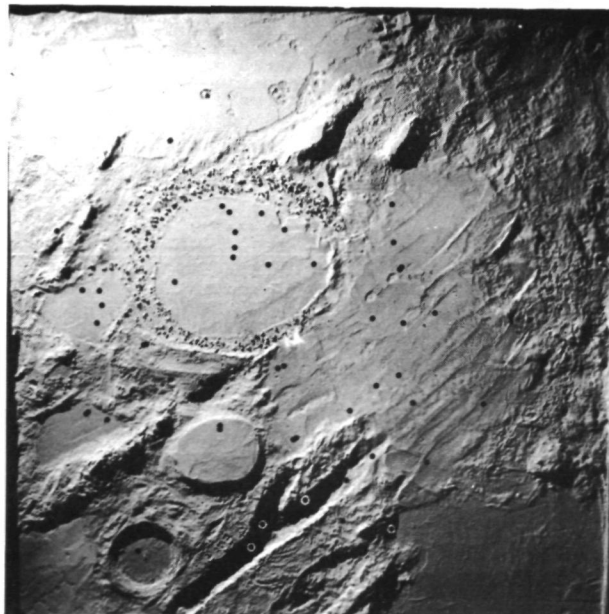


Figure 32 Monte Carlo Run (Field-of-View = 8.68 deg)

In summary, it has been established that the optimum system would probably have the following characteristics: (1) nine subframes per decision, (2) guidance toward the best single subframe at every decision, and (3) a field-of-view on the order of 17.36 deg.

To answer the question regarding how success probability varies with sun angle, quantitative data was required. The computer memory was too small to hold ratings for all possible landing sites, and it would have taken several months to rate all sites and store the ratings on tape. Practical constraints, then, required that an experimenter must rate the selected sites selected after the fact. Since the rating was, to some extent, subjective, a technique was devised to minimize experimenter bias either for or against the system. After each landing, the computer recorded the selected site on magnetic tape. The experiment ran automatically, so the experimenter did not see what sites were selected by the system. Then, at a later date, the experimenter used a second computer program to rate the sites. This program positioned the system camera at all the selected sites recorded on tape and asked for a rating. It also positioned the camera at sites it selected totally at random and asked for a rating. The random number generator was used to determine whether to present a random site or a site from the tape each time, so the experimenter never knew whether a given site he was rating was system-selected or randomly-selected. For each site, the probability was 50% of rating a system-selected site. This removed experimenter bias and provided an index of his optimism or pessimism, since a success/failure record was produced for both random and selected sites. Somewhat unexpectedly, these random sites showed that the success/fail judgment was not as subjective as one might think.

Ratings were given in terms of the experimenter's estimate of the probability of success, in percent. On the basis of this rating, the computer used the random number generator to complete the landing by determining whether or not the lander crashed. For example, if the experimenter rated the site as having 70% survival probability, the computer selected a random number between 0 and 100 and counted the landing as a success if the number was less than 70. As it turned out, the surface had very few sites that were neither very good nor very bad. Figure 33 is a histogram showing the ratings given to the 208 randomly selected sites rated in the sun angle experiments. Because the model had very few sites that called for really

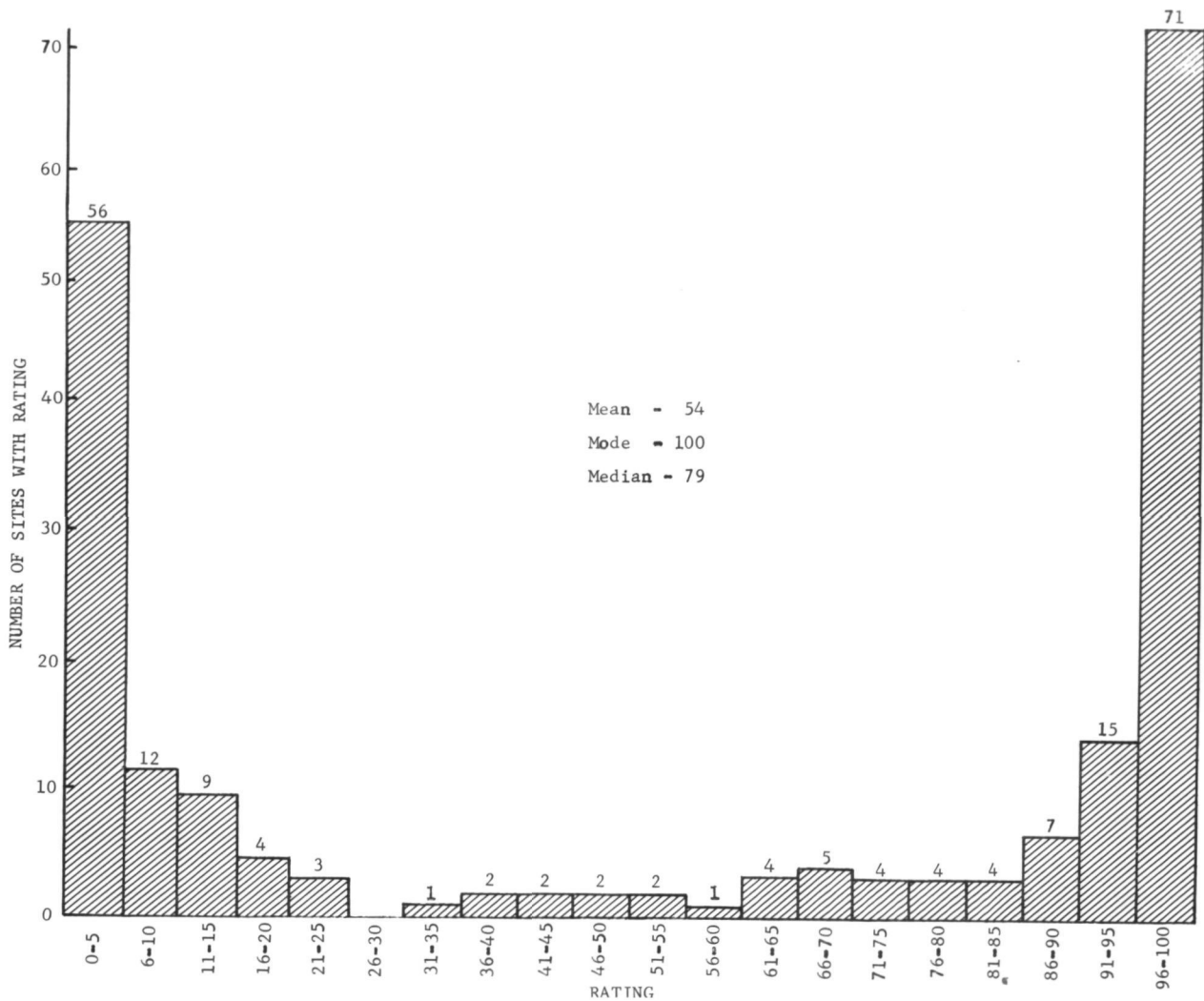


Figure 33 Distribution of Ratings for 208 Randomly-Selected Sites on Model

subjective ratings, the experiment was more objective than one might expect.

Figure 34 shows the results of the sun angle experiments. The vertical bars show the 50% confidence intervals for crash probability in the four experiments for both system-selected and randomly selected sites. The circles on the bars show the actual percentage of the landings in each experiment that were crashes. The x's on the bars show the percentage corrected for experimenter optimism or pessimism as revealed by the corresponding ratings for randomly selected sites. If the experimenter had been consistent, the random samples should all have about the same average, as they were not influenced by sun angle. The curve is the estimated crash probability curve based on the

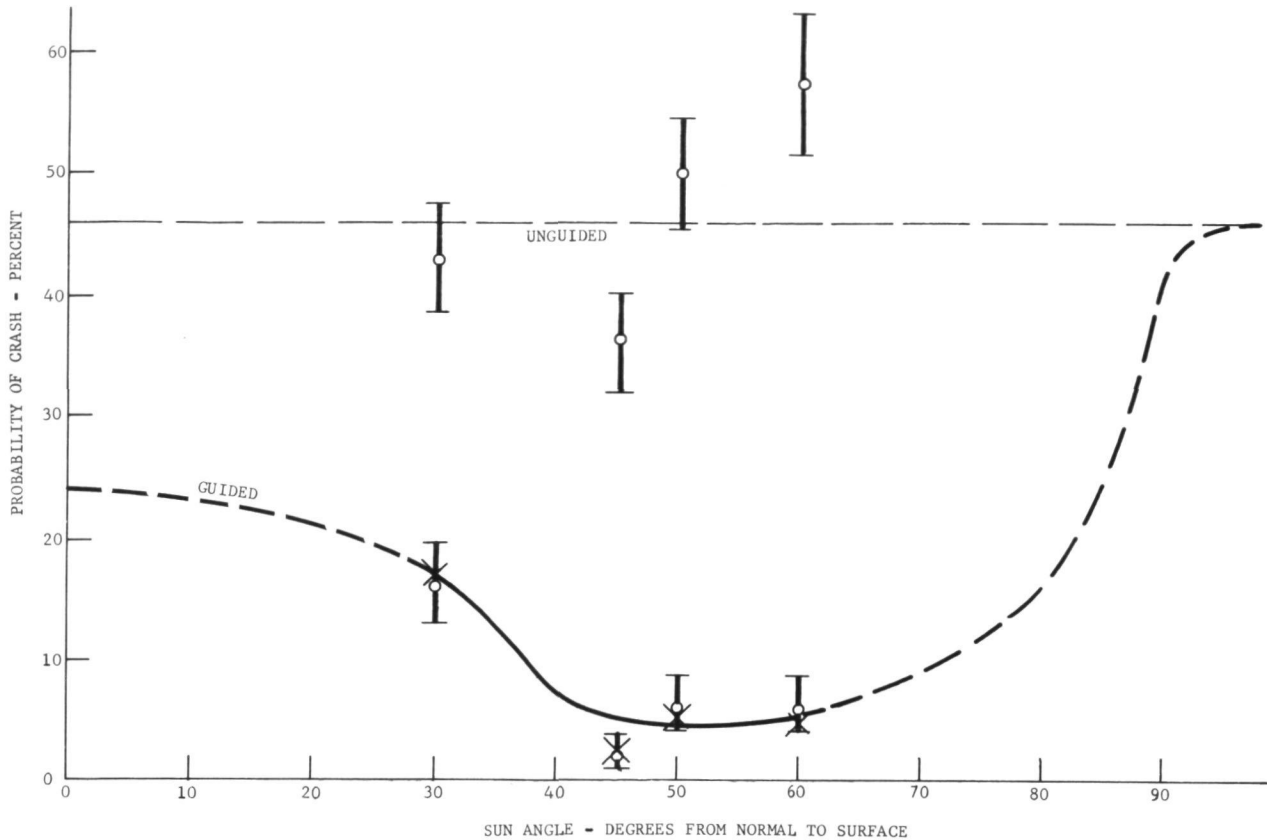


Figure 34 Crash Probability versus Sun Angle

experimental data, on knowledge that the curve should merge with the "unguided" line when the sun is beyond the horizon, and on the fact that there must be symmetry about 0 deg, as a negative angle from normal to the surface falls on the same cone as a positive angle.

The experiment shows that for this model, crash probability is 46% with no guidance and negligible with system guidance with an optimum sun angle of 45 to 55 deg from normal to the surface. As the sun approaches the zenith, shadows become less distinct and decisions become more random as good and bad sites begin to look more and more alike. The reduced performance appears also to be caused in part by the system's tendency to move back and forth between good sites until it crashes halfway between them when the sun is high. This is shown in the wider

dispersion of selected sites. This tendency could be corrected by appropriate decision logic. It should be emphasized, however, that even with the worst sun angle tested, the system reduced crash probability about 63%.

Sites selected in the four sun angle experiments are shown in Figures 35, 36, 37 and 38.

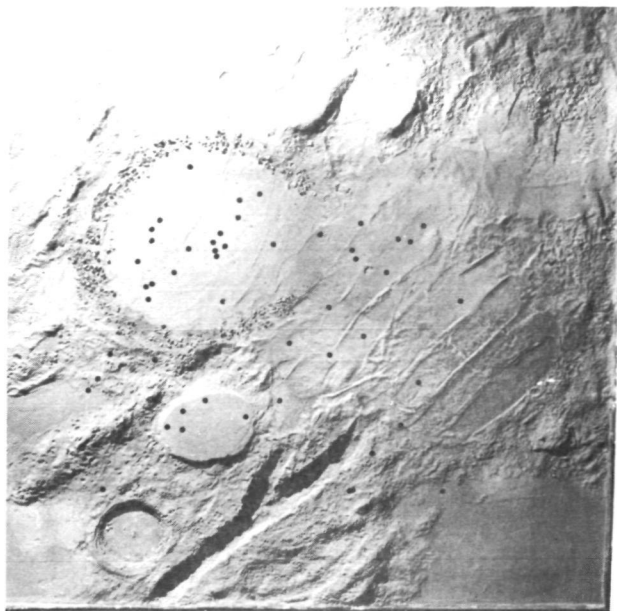


*Figure 35 Monte Carlo Run -
Sun Angle = 30 deg
From Normal to Surface*

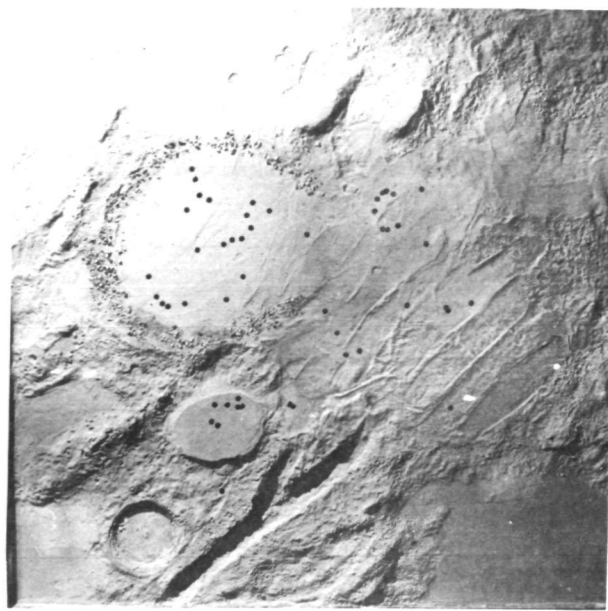


*Figure 36 Monte Carlo Run -
Sun Angle = 45 deg
From Normal to Surface*

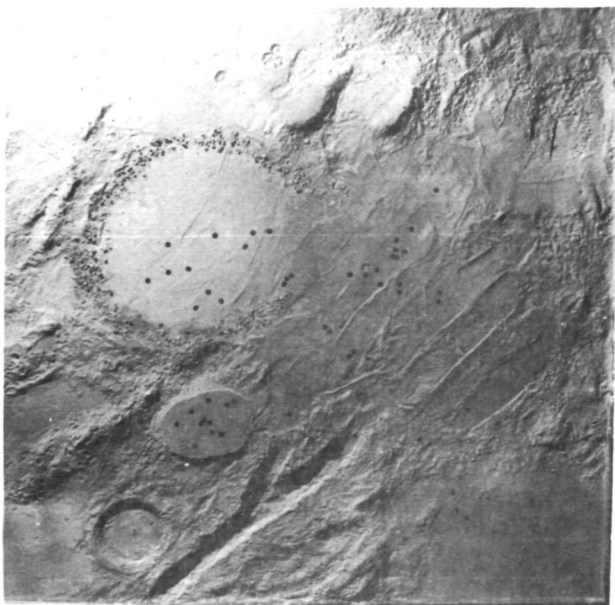


*Figure 37 Monte Carlo Run -
Sun Angle = 50 deg
From Normal to Surface*

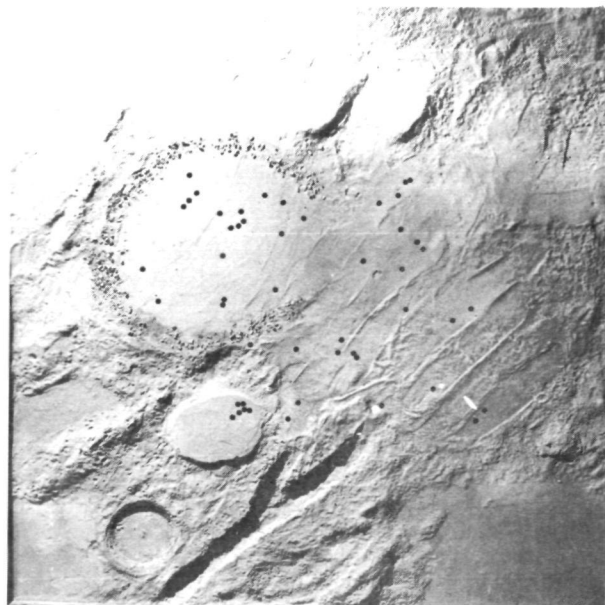


*Figure 38 Monte Carlo Run -
Sun Angle = 60 deg
From Normal to Surface*

Pointing and Tracking For Earth Resources Applications

The usefulness of earth resources satellites for monitoring water pollution is limited by the pointing uncertainty and data rate of the satellite. Since detailed pictures are usually required, the approach generally used employs high resolution and the accumulation of vast quantities of imagery data. The former greatly increases instrumentation cost, and both techniques require tedious data reduction and assimilation. It would be very desirable to build into the satellite a simple device that could autonomously look for coastlines, rivers, or whatever constituent is of interest, point the satellite imaging system to record them, and suppress registration of scenes that do not have the desired features. It was the objective of this part of the study to develop and test an algorithm for such a device. Therefore, a water pollution imager was selected as the example to be studied.

To be useful, the algorithm should autonomously:

- (1) Find coastlines and rivers and distinguish them from other features;
- (2) Track these features as the satellite moves over them while pointing and enabling the cameras;
- (3) Turn off cameras when there is no coastline or river in the field-of-view and resume the search for another coastline or river.

A satellite with such a system could accomplish the same work as current imaging techniques but with significantly less information handling requirements.

The algorithm described below has the following capabilities. It looks along a line perpendicular to the path of the satellite for a high contrast edge and determines the orientation of the edge. It then predicts, from knowledge of the edge orientation, where a nearby point on the edge should be found and moves to that point. If it finds that it is still on the edge, it centers itself on the edge at the new position and finds the edge orientation there. The process of predicting and recentering continues as the detector tracks the edge until the contrast becomes so low as to indicate that it is no longer viewing a coastline or river, or until the tracking leaves the detector's field-of-view. It then returns to search for a new edge.

Preliminary calculations indicate that a device using the algorithm could find an edge in about 1/30 sec and keep up with satellite motion while tracking rivers as narrow as 800 ft (244 m) in a field-of-view 1 to 10 mi wide (1.6 to 16 km).

In initial experiments, the system sometimes mistook a cloud-land boundary for a coastline; however, a modification of the algorithm shows promise of cloud recognition by employing optical filters.

Coastline Detection Algorithm - If a television camera scans in a circular pattern over a high-contrast edge in an image (see Figure 39a), the video signal will be, to a first approximation, a periodic square wave of the same frequency as the scanning rate (Figure 39 (b)). The scanning is accomplished by adding a voltage $V_x = V_m \sin(\omega t)$ to the horizontal deflection voltage, and a voltage $V_y = V_m \cos(\omega t)$ to the vertical deflection voltage, where $V_m \ll$ deflection voltage is required to cover the width of the photocathode.

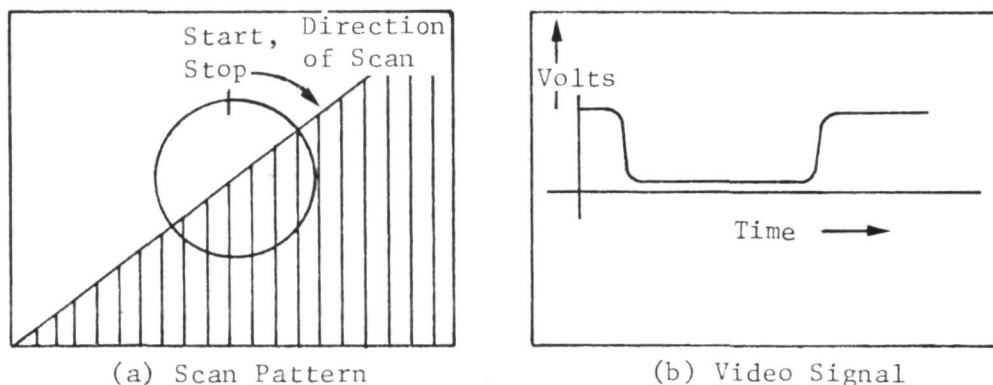


Figure 39 Scan Configuration

If we find the fundamental frequency sine and cosine coefficients of the Fourier series expansion of the video signal and interpret them as the horizontal and vertical components of a vector, we find that the vector is always perpendicular to the edge and points to the brighter side of the edge. The vector length is greatest for sharp high-contrast edges and is maximum when the circle is centered on the edge. If the vector length is divided by the video signal dc component, the result is independent of scene brightness, provided the camera responds linearly to illumination.

The required coefficients are readily found with the circuitry in Figure 40, which uses analog computer techniques to compute the Fournier coefficients:

$$a_0 = \frac{1}{\pi} \int_0^{2\pi} f(t) dt$$

$$a_1 = \frac{1}{\pi} \int_0^{2\pi} \omega f(t) \cos(\omega t) dt$$

and

$$b_1 = \frac{1}{\pi} \int_0^{2\pi} \omega f(t) \sin(\omega t) dt, \text{ directly}$$

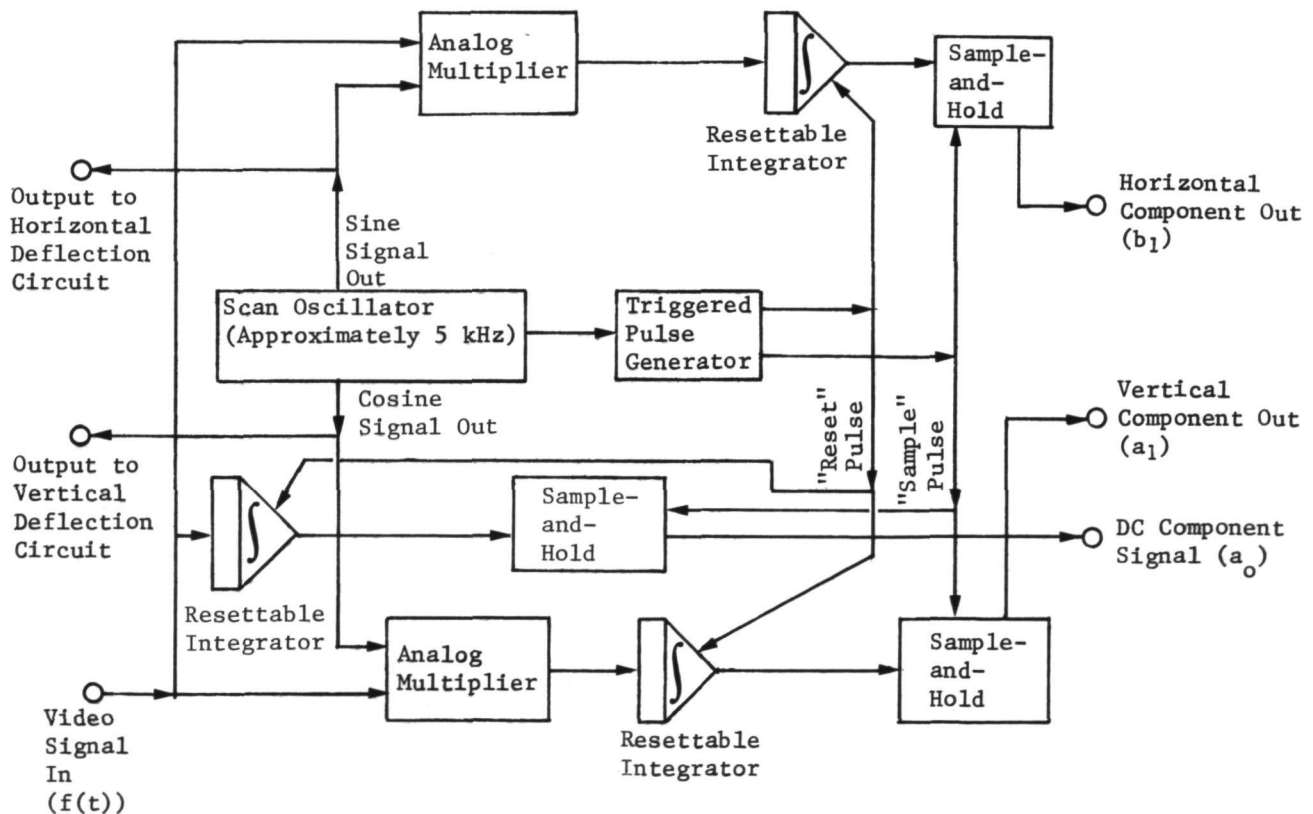


Figure 40 Circuitry for Computing Vector Components

The circuitry can be used to seek a coastline by sweeping the center of the circle back and forth across the middle of the image on the camera photocathode at a rate much slower than the circular scanning.

If the largest normalized vector length $2\sqrt{b_1^2 + a_1^2}/a_0$ is greater than 0.14, a high-contrast sharp discontinuity has been found and the tracker switches from acquisition mode to tracking mode.

In the tracking mode, the circle is displaced on the photocathode after each decision, starting at the position with maximum normalized vector length as found above. Decisions are made by the following algorithm, which may be implemented with analog or digital electronics, or by an onboard computer if one is provided for other functions. In the algorithm, the "y" direction is assumed to be in the direction of satellite travel, and x_0 and y_0 are voltages to position the scanning. Initially, scanning is positioned at the point determined above. Then proceed as in the following steps:

- (1) Clear flip-flop A. This flip-flop passes a_1 and b_1 when cleared and multiplies them by -1.0 when it is set;
- (2) Let $\ell = \sqrt{a_1^2 + b_1^2}$ (this can be computed with analog circuitry if this is most convenient in the particular system);
- (3) If a_1 is greater than zero, we will be tracking in the opposite direction from the satellite's motion so we set flip-flop A to reverse the polarity of a_1 and b_1 ;
- (4) Let $y = -a_1 k/\ell$, where k is a gain factor selected for best system performance, chosen during equipment design so that $\sqrt{(\Delta y)^2 + (\Delta x)^2}$ is approximately one-fourth the circle radius;
- (5) Let $\Delta x = b_1 k/\ell$;
- (6) Let $d_x = \Delta y$;
- (7) Let $d_y = \Delta x$;
- (8) Scan circles centered at $(x_1 = x_0 + d_x + \Delta x, y_1 = y_0 + d_x + \Delta x)$, $(x_2 = x_0 + \Delta x, y_2 = y_0 + \Delta y)$, and $(x_3 = x_0 - d_x + \Delta x, y_3 = y_0 - d_x + \Delta y)$ and determine new Fourier coefficients for each.

(8) (Continued)

The centering producing the maximum value of $\sqrt{(a_1')^2 + (b_1')^2} / (\frac{1}{2} a_0')$ is taken as the new x_0, y_0 , and a_1, b_1, a_0 , and ℓ are now the values for this centering;

(9) If the procedure has not caused tracking off the photocathode and $2\ell/a_0 > 0.14$, go to step (4);

(10) Otherwise, return to acquisition mode.

Drift in analog circuits can be tolerated if an analog approach is used to implement the algorithm because the procedure is self-correcting with reasonable drift rates. Correction for satellite motion is required if a very narrow field-of-view is used.

The high-resolution camera is positioned by the tracking camera voltages (x_0 and y_0 in the preceding algorithm). Pictures are taken periodically when the system is in tracking mode. This should produce a high percentage of coastline and river photographs.

Cloud Detection - A sharp contrasting edge is not necessarily a coastline. The edge might be the boundary between forest and bare rock or soil, between irrigated land and desert, between cloud and land, or between cloud and water. To be most useful, the algorithm should distinguish between shorelines and other types of edges. Two approaches show promise.

One approach involves restricting the spectrum the camera "sees" to a part of the spectrum where coastlines tend to produce vectors much longer or much shorter than other edges. Deep red appears to be the best part of the spectrum for this. At 7500 \AA , for example, the reflectance of coniferous forest and granite are very nearly the same so the "vector," that the edge between these two terrain types would produce, would be quite short. Water, however, has very little reflectance at this wavelength; and a water-granite or water-forest interface would produce a long vector.

Unfortunately, interfaces between clouds and nearly all terrain types would produce long vectors also. This is shown in Figure 41.

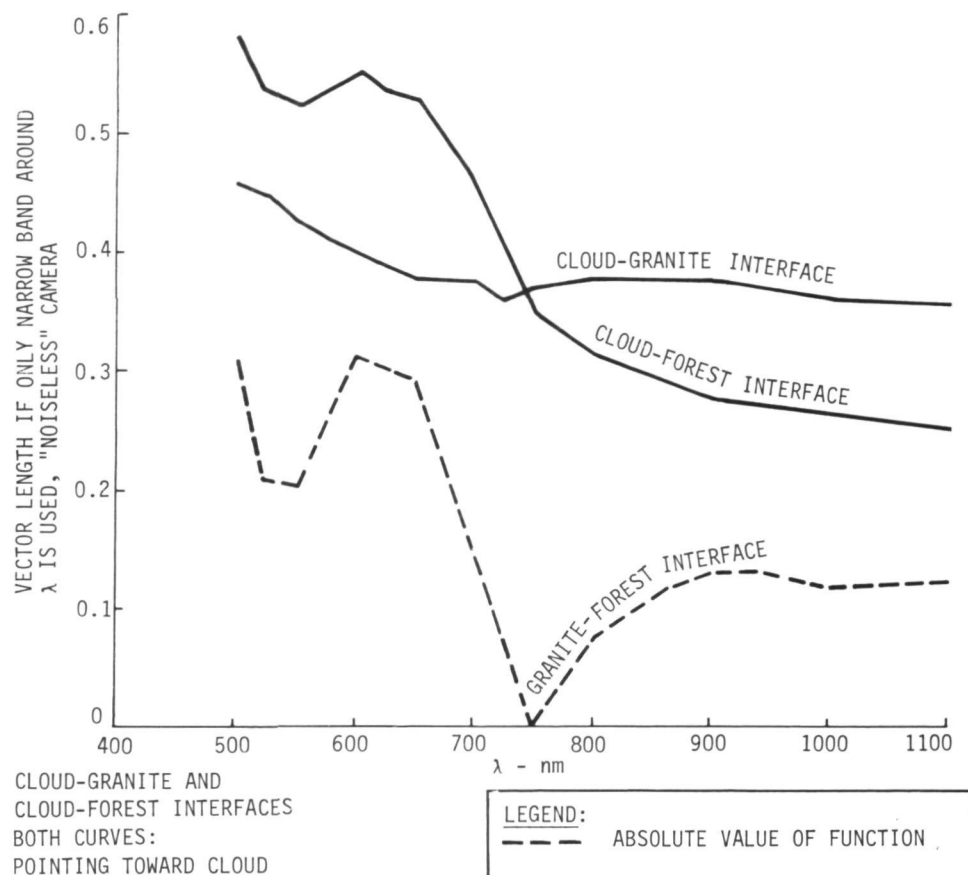


Figure 41 Vector Length as a Function of Wavelength for Various Interfaces

At a single wavelength, a cloud-land interface might produce a vector length very much like that produced by a land-water interface. The confusion can be resolved by computing the vector length again at, say, 4000 \AA where a land-water edge would produce, typically, a shorter vector--in some cases even opposite in direction--while a cloud-land vector would tend to be near the same length at both wavelengths or actually be longer at the shorter wavelengths.

Since the algorithm requires that the photocathode be wide but not particularly long in the direction of satellite motion, this two-color measurement might be done with one camera, using one half for the same image filtered for about 7500 \AA as illustrated in Figure 42. For example, if a multi-aperture image dissector camera were used, the electronics package would simply switch in whichever image was desired. Alternately, a bias would be added to the deflection voltage or current of a single-output camera to scan the second image.

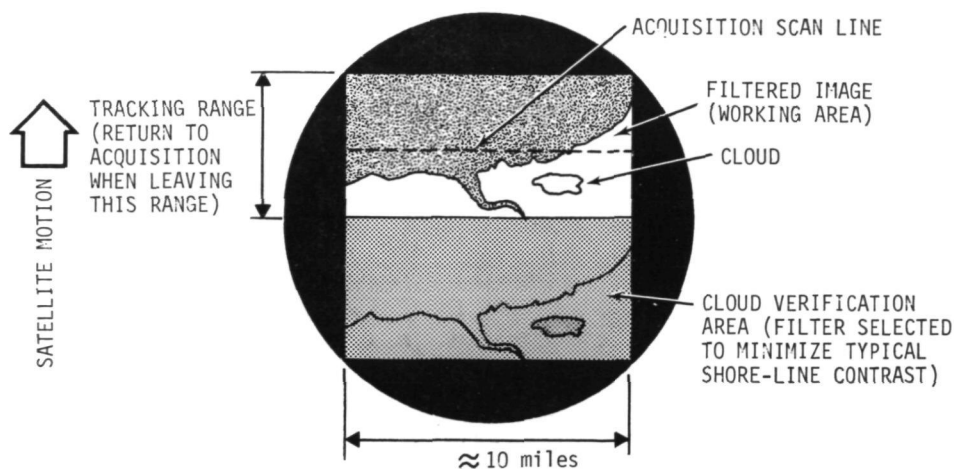


Figure 42 Multispectral Scanning Scheme

A laboratory experiment was conducted using a simulated cloud and a gelatin filter to verify that the vector length changes in the expected manner with filtering. Experimental results agreed with predicted results, wherein the vector length was changed over a 2.8:1 range by filtering.

The second approach to cloud detection requires more sophisticated electronics but simpler optics. It is based on the fact that, compared to land, clouds and water both tend to appear very smooth at 7500 \AA . If the electronics package compares the contrast on the "dark" side of the edge with that on the "bright" side, clouds might be recognized since the bright side has less contrast. This approach shows somewhat less promise than the multi-filter approach described above, but it would be smaller and lighter in weight. Laboratory experiments have not been conducted to test the second method; however, analysis indicates that it would be more apt to make errors than the other method. Good results might be obtained by combining the two techniques.

Experimental Results - The tracking algorithm has been tested. Figure 43 was produced by a PDP-9 computer from Figure 44 by implementing the algorithm with an image dissector camera and using an analog/digital interface to allow the computer to simulate the functions of some of the electronics. The computer produces a line printer plot of the scene and then, by means of a chart recorder, traces on the plot the path it tracked for a permanent record of the run. The scene used was a satellite photograph as illustrated in Figure 44. To the scale of these

Figure 43 Record of Track Produced by Algorithm

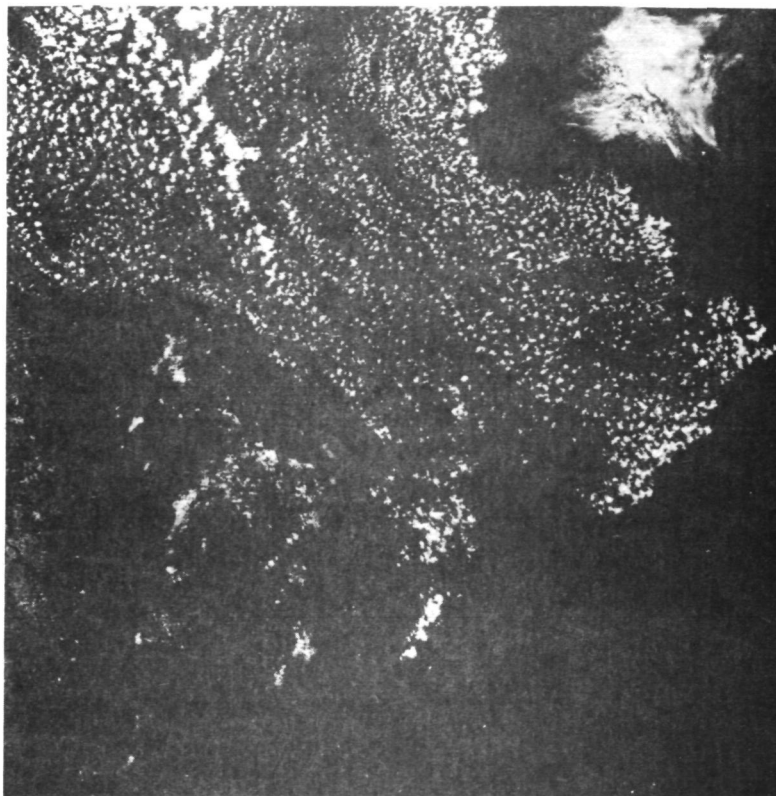


images, the "scanning circle" diameter was approximately 0.27 in (6.8 mm).

In this experiment, there were no confusion factors such as clouds or high-contrast features other than coastlines and no islands were encountered. More experiments were run to see what would happen when these factors were introduced. It was found that clouds over land were not frequently mistaken for coasts. This probably was due largely to chance and to the fact that the clouds were small with respect to the scanning circle. In one experiment, shown in Figures 45 and 46, tracking proceeded normally until a coastal cloud was encountered. Tracking then went around the cloud until the satellite motion (simulated by computer software) moved the cloud out of the field-of-view. The algorithm then relocated the coast and continued tracking properly. Similar problems have been encountered with islands. The latter should be a minor problem in a real satellite, however, since the field-of-view changes completely approximately once every 1.2 sec, representing about 6 mi (9 km) of satellite motion. This would automatically prevent continuous encircling of island. Analysis indicates that the clouds could be avoided by one or both of the cloud detection techniques described earlier. Extensive experimentation has not yet been conducted.

The minimum vector length for tracking in step 7 of the algorithm on page was determined experimentally. Real coastlines in the pictures used produced vector lengths on the order of 0.25 and few other features produced lengths over 0.10. When the threshold was set to zero, the tracker wandered randomly over the photograph after coming to the end of a river. When the tracker again encountered a coast, it went back to tracking the coast properly. Where picture brightness increased or decreased as a function of distance from the coast, the tracker tended to track a constant-brightness contour parallel to the coast for a considerable distance. The experiment (Figs. 45 and 46) used a threshold of 0.14 to track a feature and 0.03 to cause a return to the acquisition mode. A wide range of threshold settings between 0.03 and 0.25 seem to work well. The optimum setting is difficult to determine using photographs, since it is dependent on what optical filtering is used and perhaps on sun angle and other factors. The maximum length possible is 0.6366.

In conclusion, experiments have been performed indicating that the tracker is capable of distinguishing coasts and rivers from other terrain features and that it would allow the use of



14072-30 14072-001 14071-301 14041-00 14071-00
28JUL72 C N41-52/14071-28 N N41-51/14071-26 MSS 5 7 D SUN EL57 RZ125 192-0068-N-1-A-D-L1 NASA ERTS E-1005-15005-# 01



Figure 46 Tracking Experiment Results

lower-resolution cameras for water-pollution imaging and increase the percentage of usable photos returned. This would result in the secondary benefits of lowering the data rate in radio transmissions to ground and, therefore, potentially lower transmitter power requirements for a given signal-to-noise ratio. The system could use an onboard computer if one is available, but it is simple enough to be constructed with a reasonably small amount of dedicated electronics.

The technique used for these experiments was a sequential edge-tracking algorithm typically employing an image dissector television camera and a small analog circuit to compute three Fourier coefficients from the video signal. This results in a small logic circuit being able to derive tracking information.

Rendezvous and Docking Experiments

Figure 47, the rendezvous and docking experimental system, involves a camera and electronics mounted on a 3-degree-of-freedom translation servo. A PDP-9 computer commands the scan position of the camera and samples the video signal at that point in the field-of-view.

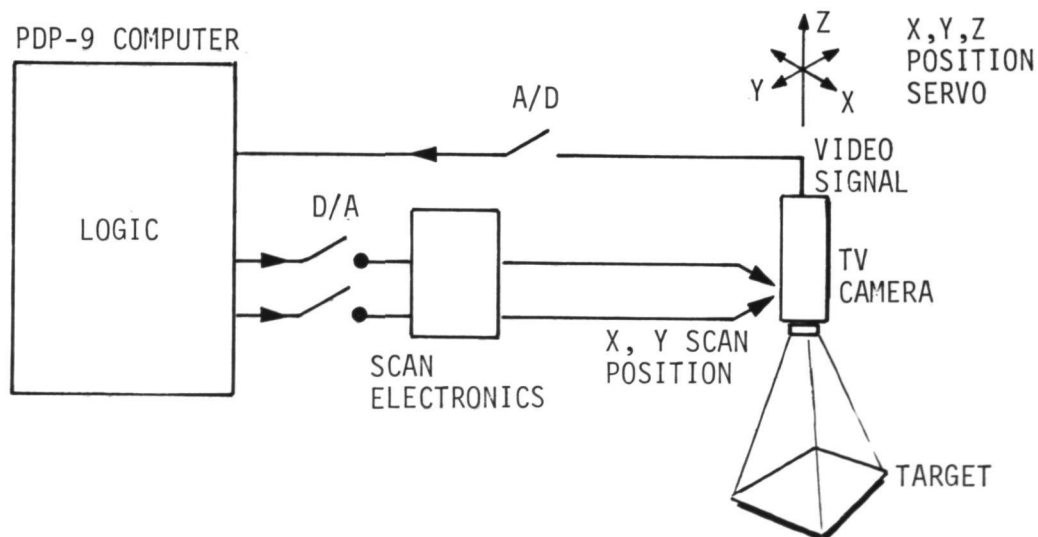


Figure 47 Laboratory Setup

The following algorithms were tested in the laboratory with representative scenes: (1) calculations for area, (2) object center, (3) angular orientation, and (4) ranging. A means of recording the scene scanned by the camera was developed. The actual scene is shown in Figure 48. Figure 49 is essentially a brightness map with the video signal quantized on a scale of 0-9. Each number represents a sample point brightness. In this case, the frame is composed of 5000 points; 100 in the X direction and 50 in the Y. The printout is dimensionally distorted due to the fixed printer spacing.

In order to calculate area and centers more accurately, thresholding was used on the video signal. This sharpens edges and excludes background clutter. We assumed that the object of interest will be brighter than the background. The logic used is: If the video signal is larger than the threshold, a "one" is assigned to the pixel; if it is less, a "zero" is assigned. Figure 50 is a threshold version of Figure 49. In the following, only threshold signals are used.

Several targets of known areas were placed in front of the camera. Repeated measurements of the 1 in² objects were

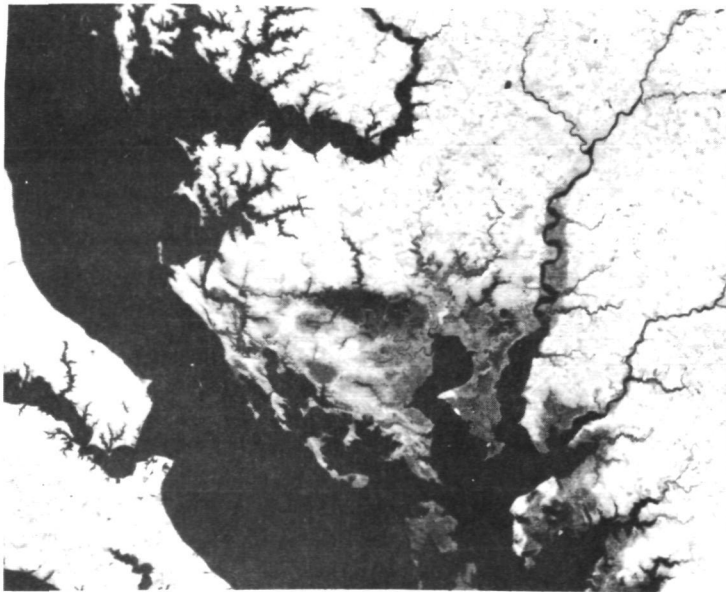


Figure 48 Test Scene

```

BRIGHTNESS HISTOGRAM
NO. SAMPLES      AVE      STD.OFV.
5000      7.5652      2.9143
LEVEL  NO. OF POINTS
0
1      171
2      701
3      415
4      286
5      184
6      201
7      202
8      279
9      2561

```

[illegible]

73

used for calibration. Tables I and II show the system calculations of the object areas. We believe that the larger errors on the small object are due to the coarseness of sample points. Repeatability was checked with several other objects of varying size. Experimental results for a simulated satellite are shown in Figure 51.

Table I Area Calculation

<u>Shape</u>	<u>Actual Area</u>	<u>System Calculation</u>
Square	0.25 in ²	0.313 in ²
Square	1 in ²	0.996 in ²
Rectangle	2 in ²	1.918 in ²
Rectangle	2 in ²	1.882 in ²
Satellite	---	2.837 in ²

Table II Area Measurement Repeatability

<u>Object Shape</u>	<u>Area Measurements (1.000 = Frame Size)</u>	<u>Mean</u>	<u>Std. Dev.</u>
Dot	0.0072, 0.0070, 0.0042, 0.0034, 0.0054, 0.0056	0.0055	0.0015
Ats	0.088, 0.0918, 0.0928, 0.091, 0.0912	0.0910	0.0018
Oval	0.2084, 0.2088, 0.2070, 0.2124	0.2092	0.0023

There is a sizeable dispersion on the smaller object measurements in relation to its area calculation.



Figure 51 Area Test of Simulated Satellite

Geometrical center calculation tests were performed to simulate conditions of small far-off objects and near objects with discernible shapes. Figure 52(a) illustrates a small bright dot that was moved around in the field-of-view. The equipment-calculated center has been scaled and drawn onto the figure (marked X and Y) to show how well the hardware worked. The area of the dot is approaching the coarseness of the sample points, hence, the area calculations are poor. Nonetheless, the center was calculated correctly. Figure 52(b) shows some bias in the Y direction. Figures 53(a) and 53(b) show the images for a representative spacecraft in different orientations. The algorithm appears to have found the same point on the object in each test.

The orientation algorithm was used to calculate the angle from local horizontal to the major axis of an oblong object.

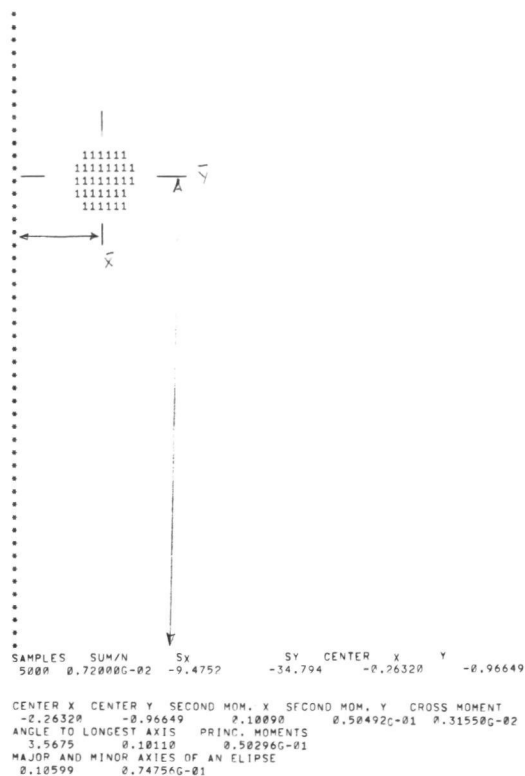


Figure 52(a) Object Center Test

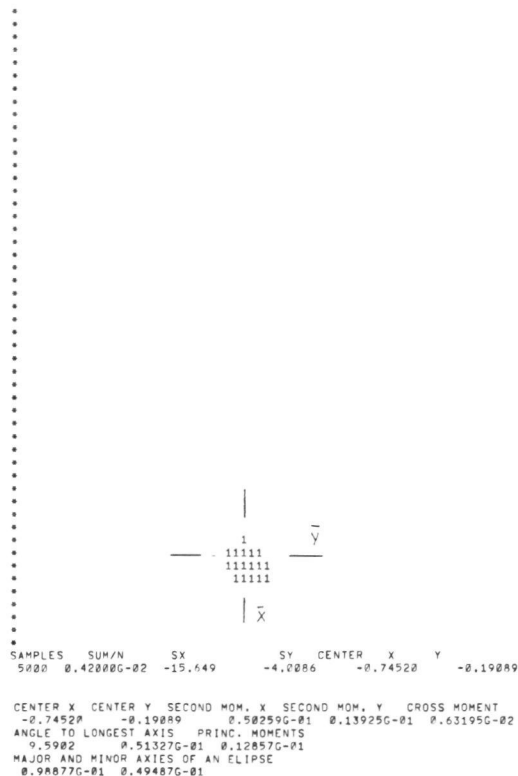


Figure 52(b) Object Center Test

Figure 54 shows two images produced by these tests. The calculated angles and centers have been drawn on the printouts for reference. The angles range from -90° to 90° since the algorithm does not distinguish one end of the object from the other.

Figure 55 illustrates the use of two cameras separated by a distance $2d$, plus center-finding calculations to find range data. To simulate this, the laboratory camera was translated in the X direction for the second picture. Using the formula derived in basic algorithms,

$$\text{Range} = \frac{2df}{X_L - X_R} = \frac{2 \cdot 1. \cdot 5.9}{1.2124 - .60546} = 19.4 \text{ feet}$$

Although it is not clear what this range means for a 3-dimensional object which may have projections toward and away from the viewer, this problem can be circumvented by viewing only a portion of the object of interest and ranging that small area alone. This would involve feature detection prior to ranging.

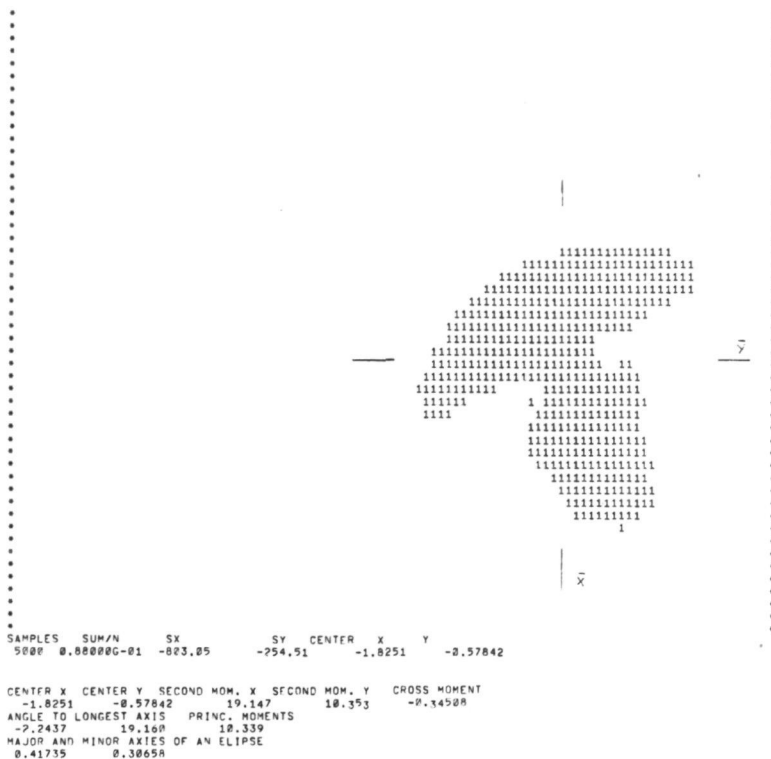


Figure 53(a) Center Test, Simulated Spacecraft



Figure 53(b) Center Test Simulated Spacecraft



Basic Algorithms - The integral of the video signal over a frame provides the average brightness of the scene. This signal is useful for automatically setting camera iris. If the video signal is thresholded such that if it is below a certain level a zero is produced, and if it is above that level, a one is produced, then the integral of this signal over a frame is the sum of the geometric areas of the bright objects in the field of view. The trick is to set the threshold at a value which passes the object of interest and eliminates the background noise. Fortunately, if the object is large enough in the field of view, background noise (stars) will not contribute significantly to the area calculation.

In equation form, this area calculation is,

$$\text{AVE} = \int_F V \, dt$$

$$\text{AVE}_T = \int_F V_T \, dt$$

where T denotes a thresholded signal and V is the video signal.

Object Centroid - By calculating the first moment of brightness in both the X and Y directions, the center of brightness may be calculated as follows:

$$SX = \int_F V \cdot X \cdot dt$$

$$SY = \int_F V \cdot Y \, dt$$

then the centers are:

$$\bar{X}_B = \frac{SX}{\text{AVE}}$$

$$\bar{Y}_B = \frac{SY}{\text{AVE}}$$

where X is the X deflection on the image plane

Y is the Y deflection on the image plane

\bar{X}_B is the X coordinate of center of brightness, and

\bar{Y}_B is the Y coordinate of center of brightness.

To calculate the geometric centroid, a threshold video signal is used as follows:

$$\bar{X} = \frac{\int_F V_T X dt}{\int_F V_T dt}$$

$$\bar{Y} = \frac{\int_F V_T Y dt}{\int_F V_T dt}$$

Orientation

The orientation of an elliptical object may be calculated by using second moments and the cross product moment using a thresholded video signal in all cases.

$$I_{XX} = \int_F V X^2 dt$$

$$I_{YY} = \int_F V Y^2 dt$$

$$I_{XY} = \int_F V XY dt$$

These values are then changed to object-centered coordinates,

$$I'_{XX} = I_{XX} - AVE_T \bar{X}_T^2$$

$$I'_{YY} = I_{YY} - AVE_T \bar{Y}_T^2$$

The angle to the major axis of the object is then:

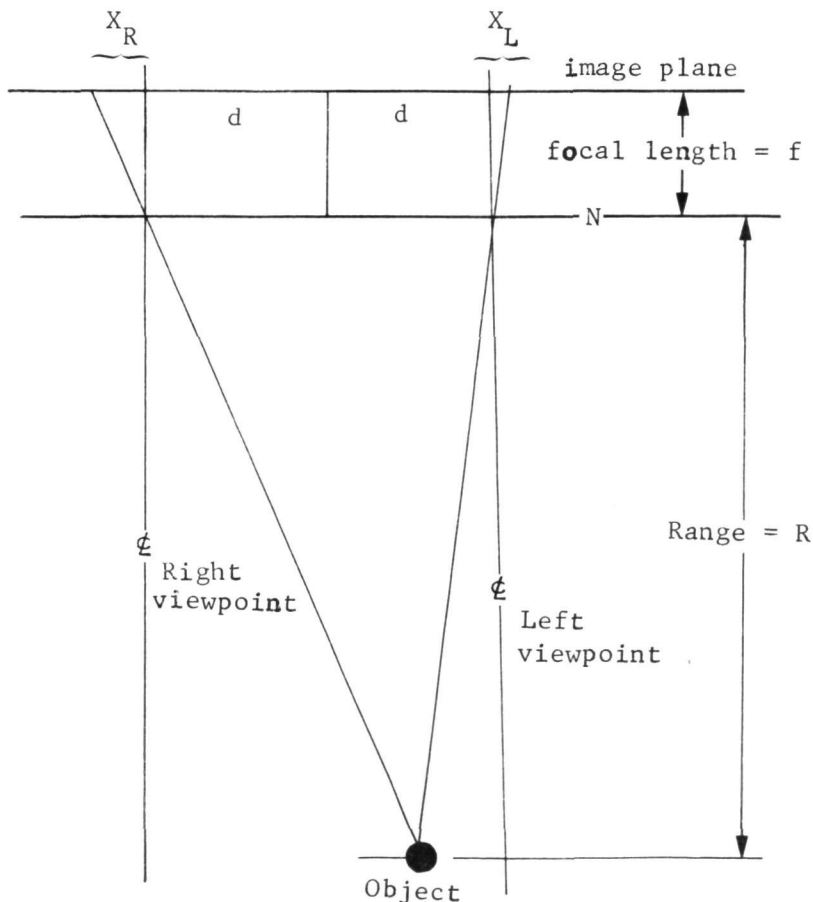
$$\sigma = \frac{1}{2} \tan^{-1} \left(\frac{2 I'_{XY}}{I'_{XX} - I'_{YY}} \right)$$

Range Calculation

The range of an object may be calculated by using the centroid algorithm and two separated views of the same object. The sketch below shows a configuration in which the two cameras (or mirrors and a single camera) are separated by an inter-ocular distance $2d$. The center of the object is found by the previously mentioned centroid algorithm for each viewpoint. These values appear on the sketch as X_L and X_R . By using the camera focal length f and the geometry of the configuration, the formula for the object range is:

$$R = \frac{2df}{X_L - X_R}$$

This simple calculation would be performed in the onboard computer. For this configuration, the cameras (or mirrors) are not gimbaled and it is assumed the camera field-of-view is large enough to accommodate the ranges of interest.



ANALYSIS OF ENTRY NAVIGATION FOR PLANETARY LANDERS

The goal of the scientific community is to be able to land unmanned planetary probes close to areas of high scientific interest. Unfortunately, current planetary landers develop large landing site dispersions because of orbit position errors, deorbit maneuver errors, vehicle L/D uncertainties and atmosphere uncertainties including winds. The Viking '75 Lander, for example, has a landing footprint 300x100 km in size that results from a statistical combination of the above errors. After the first Viking Mars landing, the atmospheric uncertainties should be largely eliminated. Aerodynamic uncertainties should be reduced and wind magnitudes somewhat better defined. Random wind variation will always contribute a dispersion effect. That leaves the orbital and deorbit errors that may be sensed by a landmark navigation system and hopefully removed by vehicle maneuvering during the entry phase.

The intent of this study is not to design the video guidance system as it would be used in this landmark navigation mode. Camera installation and look-angle requirements are not considered in detail. Rather, it is assumed that reference landmarks can be provided by the video guidance system imagery early in the entry phase after deorbit. These landmark position coordinates are then compared with predetermined position coordinates to compute a predicted impact point error. The vehicle maneuvering system, which may be either aerodynamic or propulsive, then seeks to reduce the impact point error to zero.

The Viking '75 entry vehicle is used in this study as a means of demonstrating the feasibility of such a system. The Mars atmosphere will be assumed to have been defined for future missions and is approximated by the current Mars Mean Atmosphere Model. The maneuver capability is aerodynamic; i.e., the vehicle lift vector is oriented by rolling the spacecraft with the reaction control system. This study includes a broad look at the roll control capability of the Viking vehicle based on point mass simulation of a rolled lift vector to establish what constraints might apply to the system. A detailed simulation of a roll maneuvering system in six degrees-of-freedom (DOF) will establish how well such a system can remove a wide variety of impact point errors. The six DOF landmark navigation and roll command simulation logic was incorporated in an unused

module of the MOD6MV Viking terminal phase simulator program, making it compatible with that technology.

System Operation

The video guidance system is assumed to provide the target or desired landing site planet latitude and longitude after comparing landmark position data. In reality, the target coordinates could be constantly updated during entry. In the simulation model, the target coordinates are input and do not vary during the run. The 6 DOF simulations are started at the beginning of dynamic pressure buildup (240,000 ft) and run down to parachute deployment altitude (30,000 ft). The airborne computer calculates the predicted impact point (in this case, the parachute deployment point) on a periodic basis based on its present state vector. The simulation model uses standard point mass trajectory equations for a spherical, rotating planet to compute the predicted impact point assuming a nonrolled lift vector. It computes where the vehicle would land if no further roll maneuvering were accomplished. The predicted impact point is updated every 2 to 5 sec in this study and is then converted to latitude and longitude for comparison with the target coordinates. The delta latitude and longitude between the predicted and target conditions are:

$$DLAT = TLAT - PLAT$$

$$DLON = TLON - PLON$$

These errors are then computed in down and crossrange coordinates using the impact point ground track inclination angle, INC.

$$DOWN = DLON * \cos(INC) + DLAT * \sin(INC)$$

$$CROSS = DLAT * \cos(INC) - DLON * \sin(INC)$$

A roll angle command is generated from the following equation and sent to the RCS system:

$$PHIC = C1 * DOWN + C2 * \text{ABS}(CROSS)$$

Gains C1 and C2 are selected to saturate the roll command as long as there is any appreciable down or crossrange error. Program logic must also zero out C1 when DOWN goes negative and assign PHIC the sign for CROSS for proper operation of the system. An adaptive limit is placed on the roll command based on the magnitude of the initial down range error, but is never allowed to be greater than +75 deg for Viking.

Simulation Results

Vehicle Characteristics

The study results pertain specifically to a Viking entry vehicle of 2060 lb entering the mean Mars atmosphere with a nominal L/D capability of 0.18. The vehicle moment of inertias in pitch, yaw, and roll are 297, 359, and 556 slug-ft², respectively. Rate damping control limits pitch and yaw attitude rates to approximately 1 deg/sec during entry, while the roll attitude is maintained nominally at zero so that the lift vector is in the trajectory plane.

Point Mass Studies

A parametric study of the effect of commanding nonzero roll attitudes during entry for a spectrum of entry flight path angles was conducted using a Viking point mass trajectory program, UD288. The results, in Figure 56, show the change in down and crossrange produced by rolling the vehicle lift vector from 0 to 180 deg.

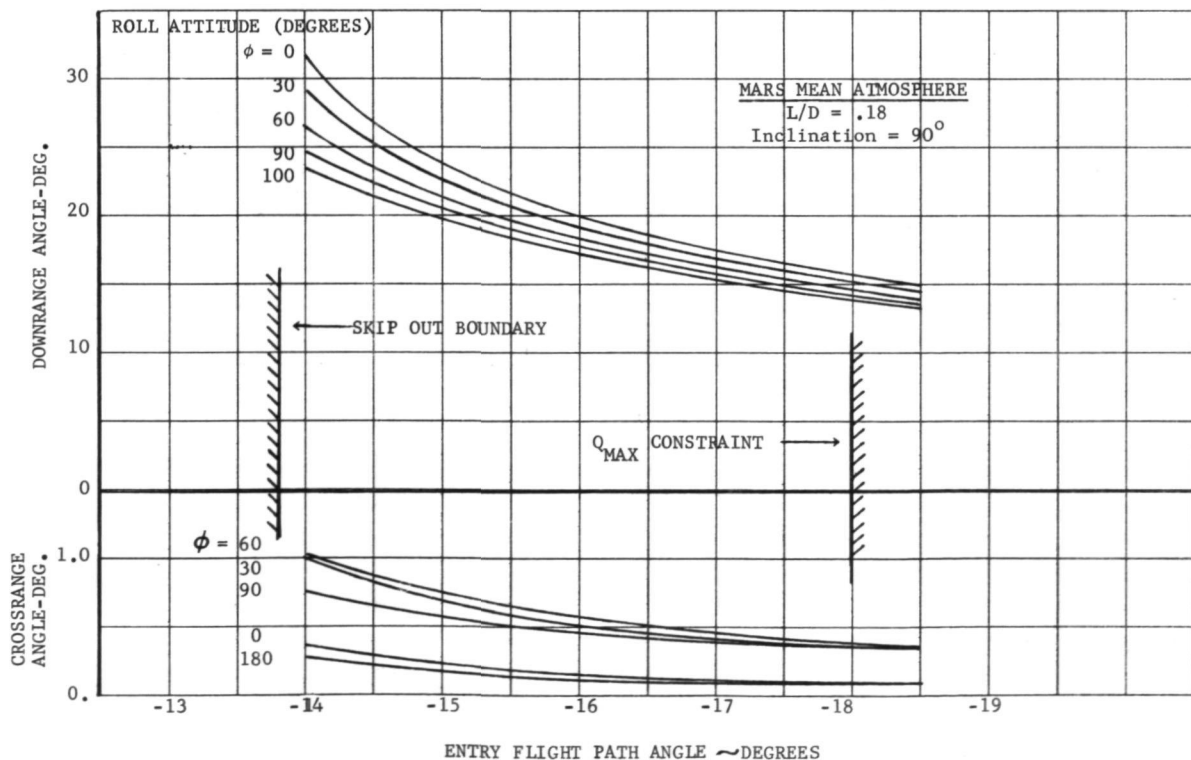


Figure 56 Spectrum of Roll Capability (Pt Mass)

The crossrange value at zero and 180 deg of roll is produced by planet rotation as the vehicle enters from polar orbit (inclination = 90 deg). The extent of roll maneuvering is seen to increase as the entry flight path angle approaches the skip out boundary of -13.5 deg. The Viking program arbitrarily defines entry as 800,000 ft above the mean surface level (MSL). A typical entry flight path angle of -15 deg is selected for more detailed examination of the effects of roll on trajectory parameters.

As might be expected, the effect of rolling the lift vector out of the trajectory plane steepens the descent through the atmosphere, causing the dynamic pressure and Mach number to be greater at any given altitude, see Figure 57.

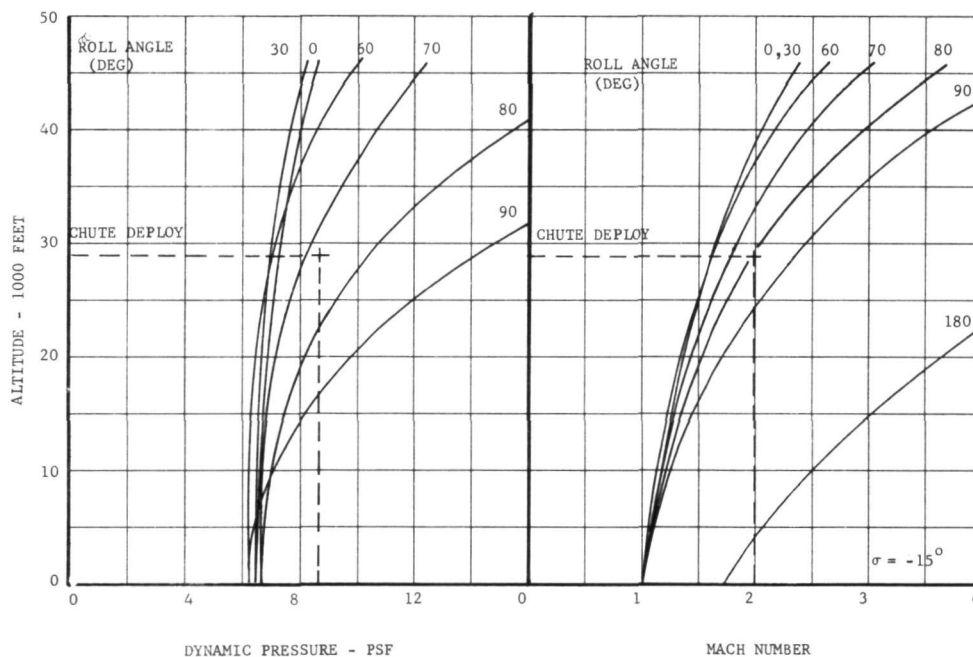


Figure 57 Mean Atmosphere Chute Deployment Constraints on Roll

This effect has serious consequences for the parachute, the propulsive terminal phase, and for the structural capability of the entry vehicle unless design limits are observed. Parachute deployment limits of Mach = 2.0 and dynamic pressure of 8.62 psf are seen in Figure 57 to limit the roll angle to 75 deg or less

for a deployment altitude of 29,000 ft above MSL. At higher entry flight angles, the roll limitation would be even more severe. This is one of the reasons for picking -15° as a nominal case for study. Figure 58 shows the effect of roll to be an increase in the maximum dynamic pressure during entry. The entry flight path angle and roll angle combinations must observe the vehicle dynamic pressure structural limit of 144 psf. The aerodynamic heating limit is very near the structural limit and observing the one will generally protect against a violation of the other.

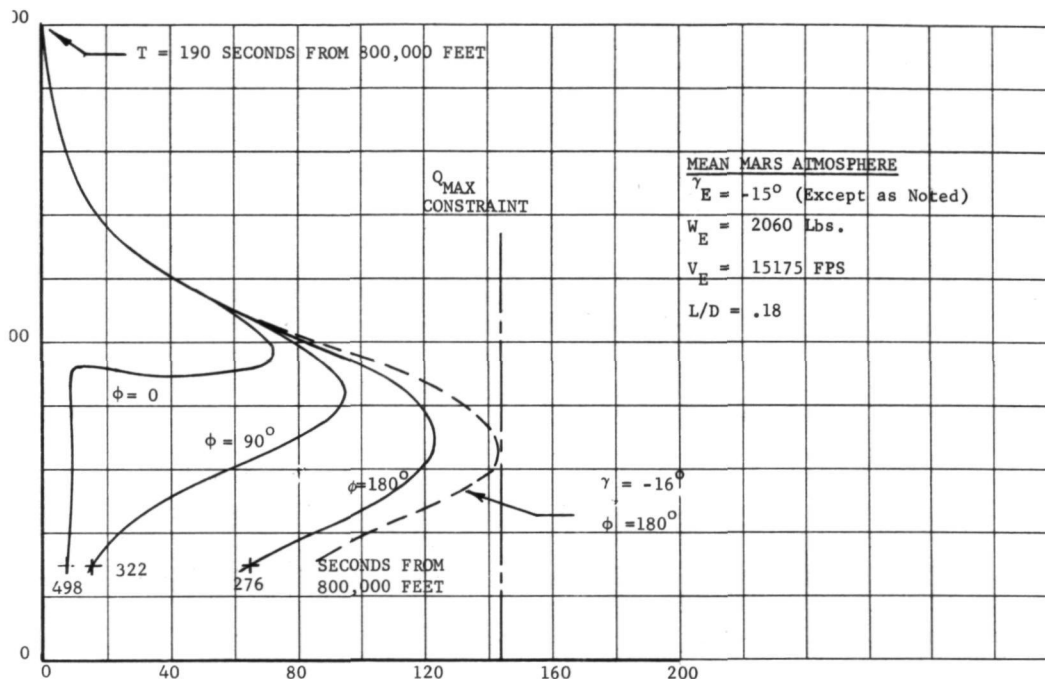


Figure 58 Roll Effect on Dynamic Pressure Profile

The point mass data show that the maximum down and cross-range changes possible through roll maneuvering are 2.75 deg (165 km) and 0.55 deg (33 km), respectively for Viking at a -15° flight path angle. Variation of this capability with roll angle is shown in Figure 59.

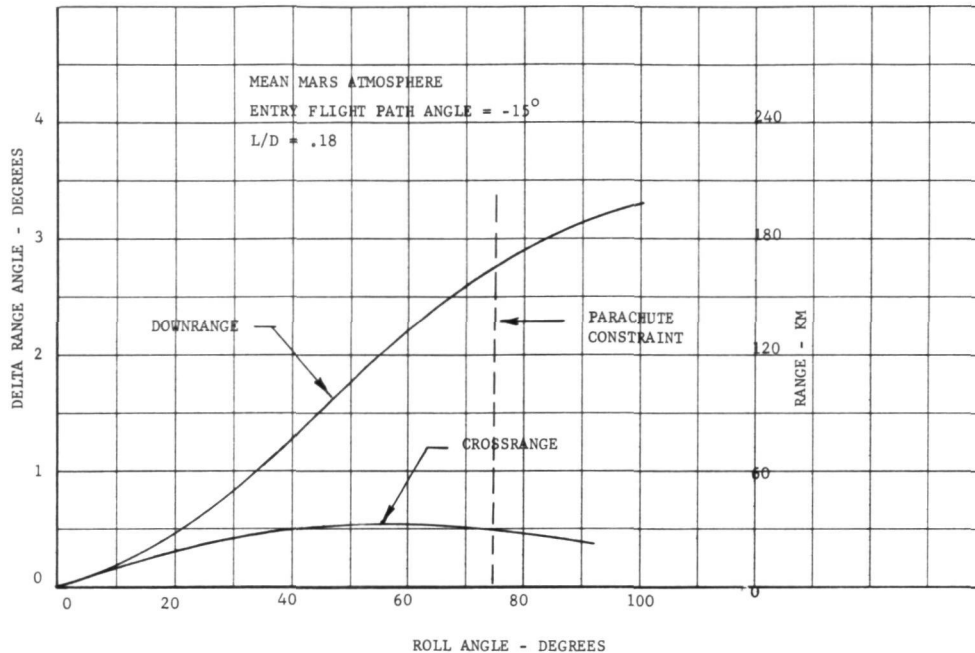


Figure 59 Down and Crossrange Capability (Pt. Mass)

Six-Degree-of-Freedom (DOF) Simulation

From the matrix of point mass data, a series of 6 DOF cases with widely varying down and crossrange errors were studied in detail. Maximum values of both down and crossrange errors were included to see whether real vehicle response to roll commands would affect the roll maneuvering capability. The five test cases are itemized in Table III along with the residual range errors that remained at parachute deployment.

Table III 6 DOF Landmark Navigation Test Cases

Target Coordinates		Initial Range		Residual	
LAT	LONG	Errors-Deg		Errors-Deg	
23.11	-1.19 (No Roll)	<u>DOWN</u>	<u>CROSS</u>	<u>DOWN</u>	<u>CROSS</u>
20.39	-0.55	2.75	0.5	0.21	0.087
20.36	-1.05	2.75	0	0.52	-0.044
22.11	-1.14	1.0	0	0.094	0.0062
22.13	-0.74	1.0	0.4	0.094	0.0165
21.12	-0.84	2.0	0.25	0.06	0.013

Range error histories of the five test cases are plotted in Figure 60. The case of maximum downrange with zero crossrange has the largest residual range error of 0.52 deg. This is an understandable limitation of the system and results from the loss of downrange capability as the vehicle rolls back and forth to keep the crossrange error near zero.

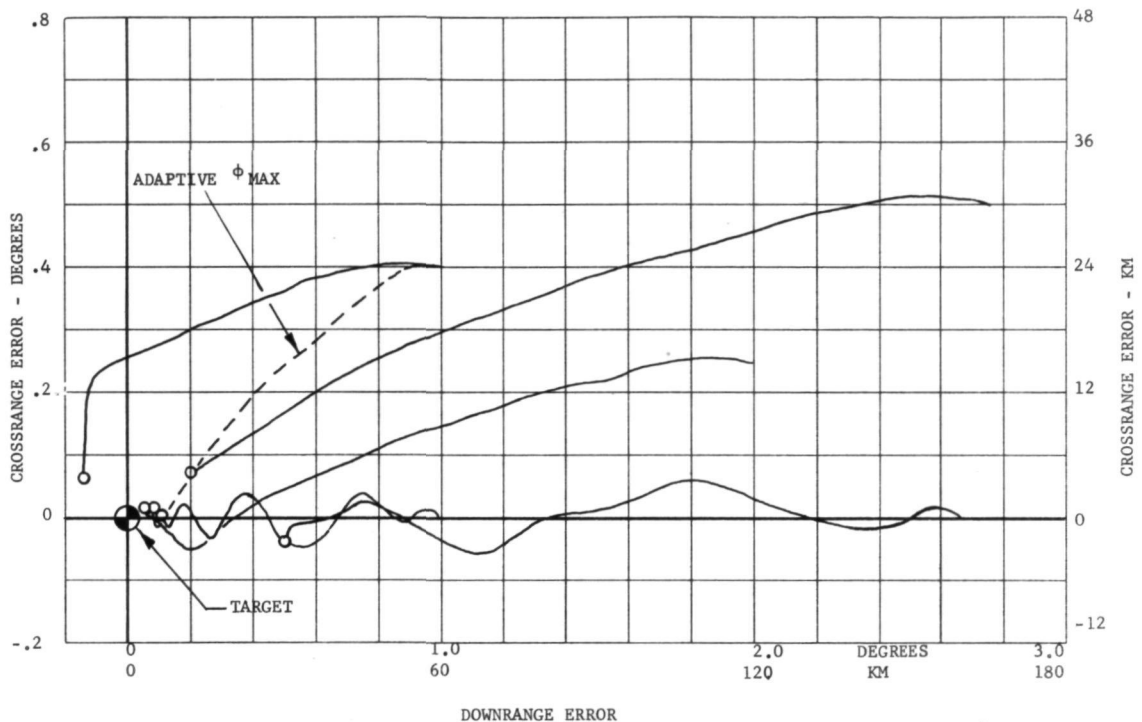


Figure 60 6 DOF Roll Capability

The present Viking vehicle roll rate is limited to 15 deg/sec to avoid excess overshoot. This results in good roll control but aggravates the above problem, which is not really a serious problem as long as it is understood.

Several important system characteristics were learned during the 6 DOF study. First, the roll command gains have to be made large enough so that the maximum roll angle is commanded until the range errors reduce to acceptably low values. This is true, because you have to take out the range errors while you have maximum maneuvering capability, since you run out of capability later in the trajectory and can't make up the difference. Second, the short downrange error cases consistently

overshoot the target (see case with 1 deg downrange and 0.4 deg crossrange in Figure 60). These cases were achieving their downrange target with a maximum roll angle of 75 deg right at maximum dynamic pressure. Before the roll attitude could be returned to zero, about 5 sec of downrange overshoot occurred. The use of adaptive gains and rate feedback in the roll command equation were considered until a very simple solution was discovered. The maximum roll command is limited to a value no higher than what is required to cope with the initial downrange error. In other words, the maximum roll command is made adaptive to the in-flight determination of the initial downrange error. This allows the vehicle to pass through the maximum dynamic pressure region before acquiring the target coordinates. The improved range error history with the adaptive logic is shown by the dotted trace in Figure 60.

Trajectory plots for the maximum downrange, zero crossrange cases are presented in Figures 61 through 65 as typical of the behavior of the system. The Mach number and dynamic pressure values of 2.0 and 8.5 psf at parachute deployment are seen in Figure 62 to agree with the values that were used to limit the maximum roll angle to 75 deg. In this particular case, a computing cycle of once every 5 sec was used to update the predicted impact point. This interval was used primarily as a means of reducing computer execution time, but probably represents the upper limit of suitability for this function.

Offset Aim Point Strategy

The technique of rolling the vehicle lift vector to obtain down and crossrange maneuvering has one important feature that should be incorporated into the targeting strategy. The lift vector can be rolled in either direction away from zero roll to shorten the downrange distance, but there is no way of increasing its range capability. Figure 66 shows the shaded area from which roll maneuvering can be used to arrive at the desired landing site or target. The upper portion (Figure 66) shows the normal situation where the desired landing site is also the aim point; i.e., the center of the 3σ dispersion ellipse. Since the dispersion pattern is a three dimensional normal distribution, one can reach the target area through roll maneuvering only 15 to 25% of the time. If, however, the aim point is moved approximately 80 km downrange of the desired landing site, as in the lower figure, one could maneuver to the desired landing site 87% of the time. This results from the fact that the central 1.5σ ellipse of the aim point dispersion contains 87% of the cases in the distribution.

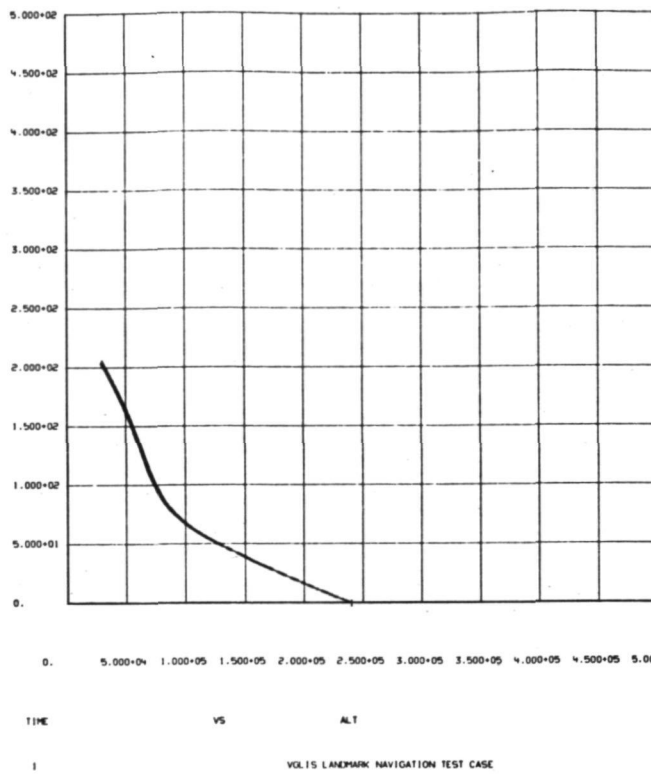


Figure 61 Altitude/Time Correlation

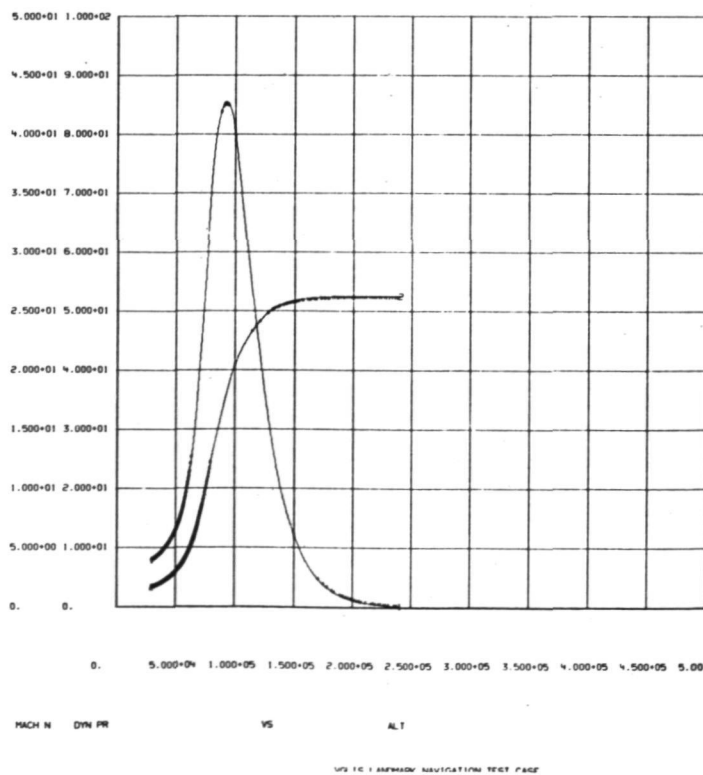


Figure 62 Mach Number and Dynamic Pressure

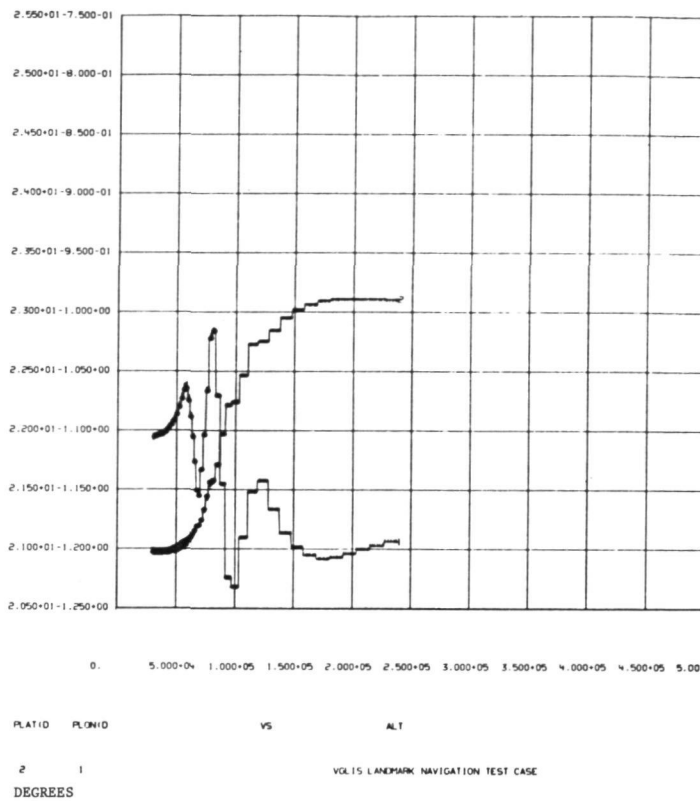


Figure 63 Predicted Impact Point History

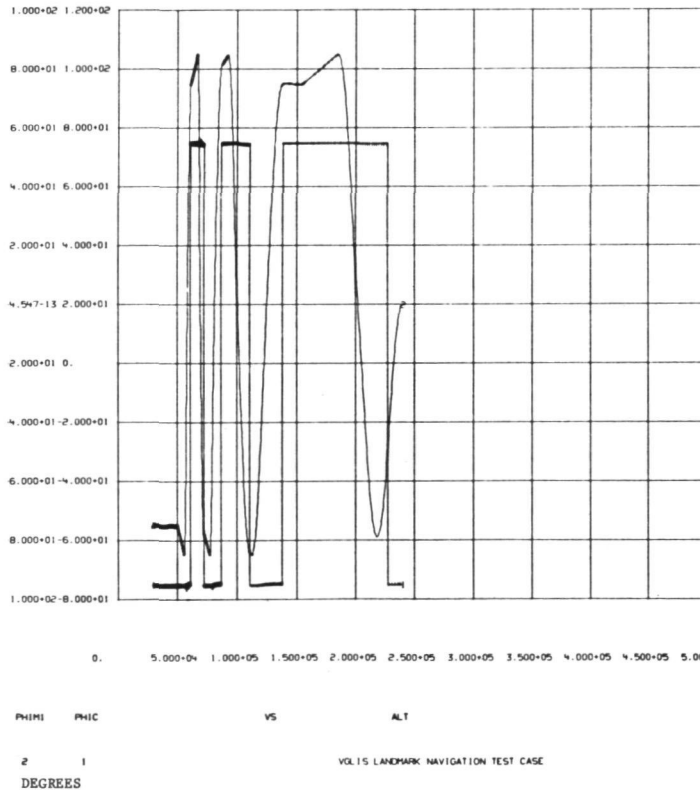


Figure 64 Roll and Roll Command

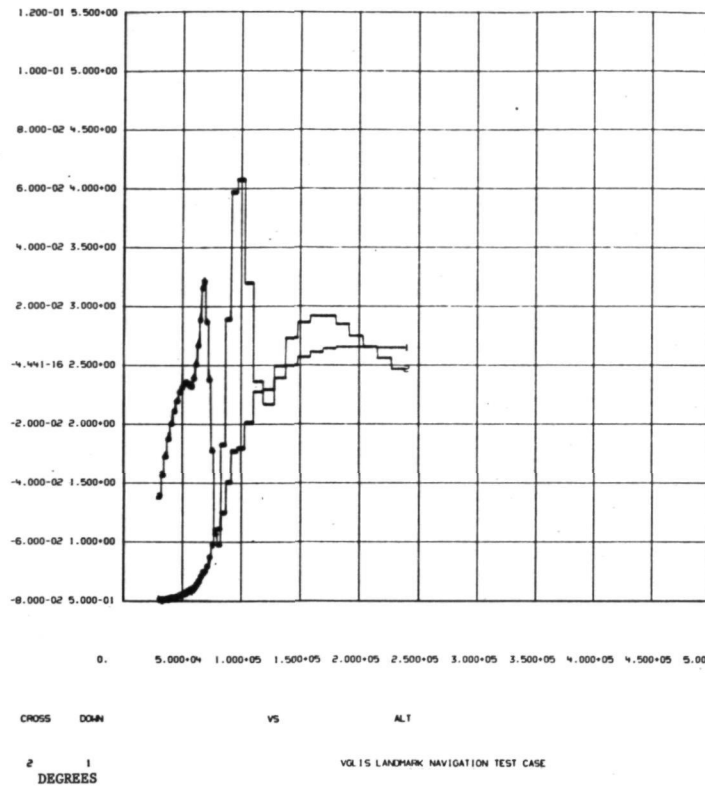


Figure 65 Down and Crossrange Errors

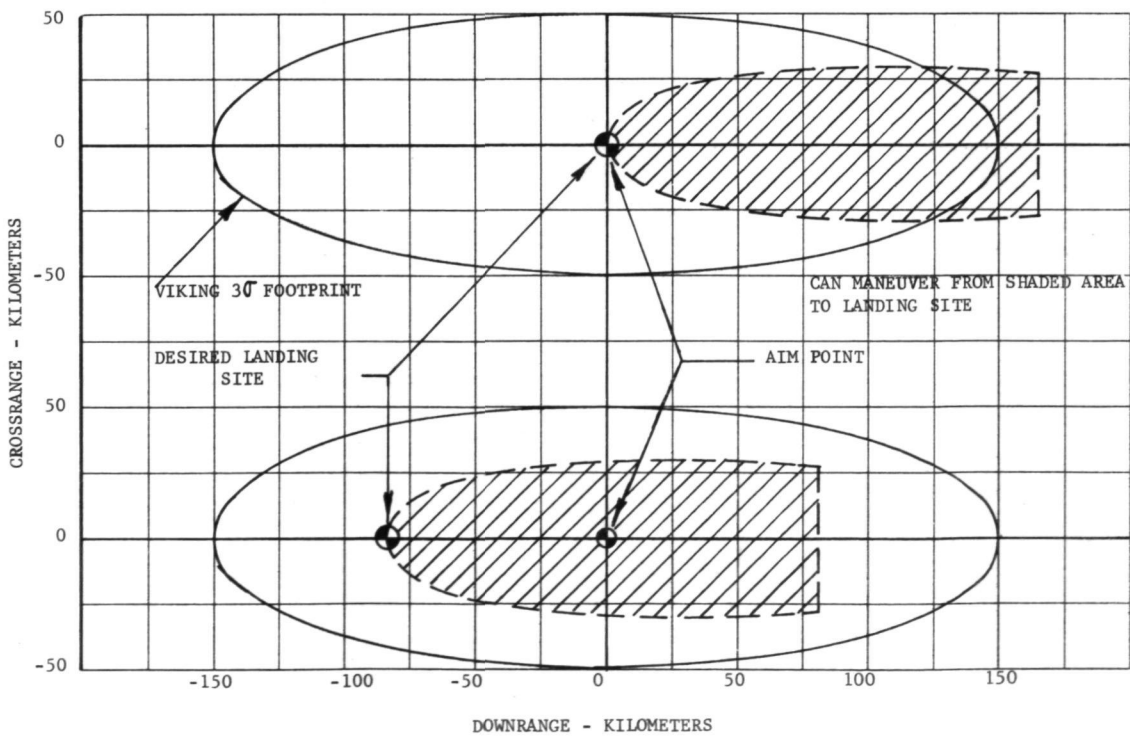


Figure 66 Offset AIM Point Used with Roll Maneuvering

A further clarification of the above probability statement must be made here. The total Viking 3σ dispersion ellipse is created by statistically combining many factors. We will divide these factors into two major categories; i.e., those that occur early in the entry can be sensed by landmark navigation and reduced through roll maneuvering, and those that occur in the atmosphere too late to be effectively eliminated. The first category includes orbit position errors and deorbit errors in direction and velocity amounting to a 288×86 km error ellipse. The second category, including L/D tolerances and atmospheric winds, produces an 80×50 km dispersion ellipse. These two major effects, when RMS'd create the total dispersion ellipse of 300×100 km. If the roll maneuvering area is assumed to be a 140×60 km ellipse, and is centered in the 288×60 km dispersion, which it is effective in eliminating, it represents 1.77σ or 92% of the distribution. The probability statement should read as follows: Ninety-two percent of the time the landmark navigation and roll maneuvering system will enable the Viking lander to land within a footprint of 80×50 km. This represents more than a 50% reduction in the size of the unguided impact dispersion.

Conclusions and Recommendations

1. The VGLIS must not only be able to recognize landmarks but must be able to compare these actual positions with pre-determined positions in order to generate range errors in the target area.
2. A maneuvering system using roll control of the lift vector on the Viking spacecraft can be successfully mechanized to remove approximately 50% of the current landing impact dispersions.
3. Offset aim-point targeting is a procedure optimizing the benefit that can be derived from landmark navigation and roll maneuvering.
4. Roll modulation of the lift vector causes significant changes in the entry trajectory Mach number and dynamic pressure history. The entry vehicle and subsystems must be able to survive this environment. The Viking '75 entry vehicle could not use roll modulation in the worst-case atmosphere because it is already up against design limits. The first Viking Mars Mission should greatly reduce the atmosphere uncertainty and open up the possibility of using a roll maneuvering system.

5. The maximum roll angle on the current Viking entry vehicle is limited to ± 75 deg in the mean Mars atmosphere because of parachute deployment constraints.

ANALYSIS FOR TERMINAL DESCENT PHASE GUIDANCE FOR PLANETARY LANDERS

Lander Constraints and Propulsion System

The Viking terminal descent system must accomplish navigation, guidance, and control functions to successfully land the capsule on the Martian surface with prescribed vehicle velocity and attitude. The velocities required at landing are:

- (1) Horizontal velocity - 0 ± 1.22 m/s (0 ± 4 fps);
- (2) Vertical velocity - 2.44 ± 0.91 m/s (8 ± 3 fps).

The lander roll axis must be oriented with 5 deg of local vertical at landing and an rss attitude rate of 0 ± 7 deg/s in pitch and yaw is required. To maintain radar lock, attitude rates of greater than 30 deg/s [rss (pitch and yaw)] are not permitted during terminal descent.

To accomplish a soft landing, the three components of the lander's velocity measured with respect to the surface must be controlled as a function of altitude measured with respect to the surface. Because lander system studies have shown that multiple, differentially throttled monopropellant engines are the most efficient retroengines, they were selected for propulsion during the descent. Following is a summary of Viking descent guidance laws.*

Gravity-turn steering was selected as the means of controlling the lateral velocity components. This law is mechanized by rotating the vehicle about its pitch and yaw axes until the lateral body-axis velocities are zero. This causes the thrust axis to point along the total velocity vector. This steering law is simple to mechanize, because local vertical sensing is not required. Gravity causes the thrust axis to rotate toward the vertical as the velocity is reduced. An arbitrary roll orientation is maintained by using an attitude-hold mode during the descent.

*R. F. Broderick, et al: Terminal Descent Simulation Study. NASA CR-66811. Martin Marietta Aerospace, Denver, Colorado.

If the components of vehicle velocity are denoted as u , v , and w along the roll, pitch, and yaw axes, respectively, then the steering signals are:

$$\text{Pitch: } a_c = G_a w/u$$

$$\text{Yaw: } \beta_c = G_\beta v/u$$

$$\text{Roll: } \phi_c = 0$$

where G_a and G_β are the pitch and yaw gains, respectively. These signals generate attitude commands that drive lateral velocities to zero.

The axial component of velocity, u , is controlled by modulating the vehicle thrust to follow the preprogrammed desired velocity/altitude contour shown in Figure 67.

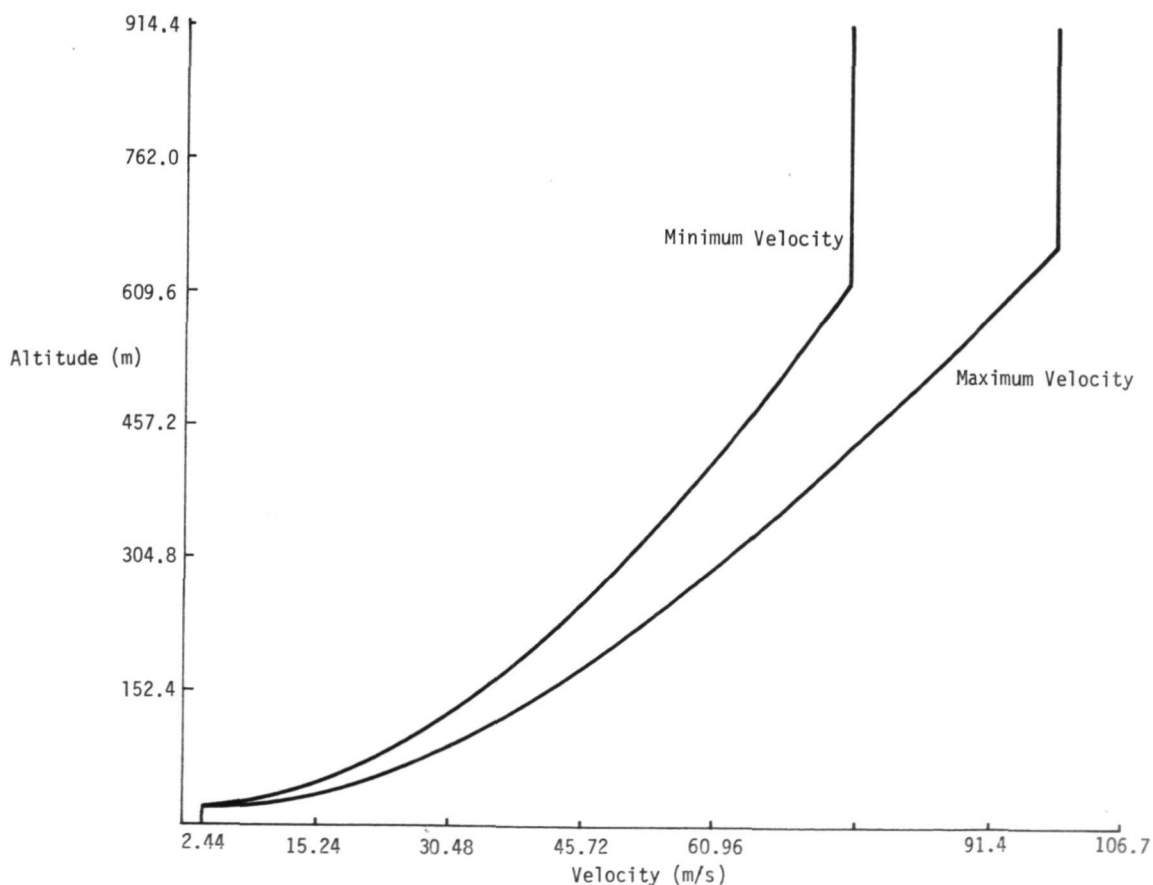


Figure 67 Viking Velocity - Altitude Descent Contour

The navigator's estimate of altitude is used to calculate a desired velocity from the contour. This desired velocity (V_D) is then compared with the navigator's estimate of velocity (V) and a throttle setting is computed that will cause the vehicle to follow the contour; that is,

$$t = G (V - V_D) + b$$

where t is throttle setting, G is the control system gain and b is the throttle setting where modulation occurs. The control system gain varies as a function of remaining fuel. The contour is designed for all velocity conditions resulting from winds during the parachute phase. It is shaped to account for propellant tank pressure blowdown and specific impulse changes. After a 2-sec engine warmup, the parachute is jettisoned and a 3-sec maneuver phase is allotted for aligning the thrust and velocity vectors. A high thrust phase is designed to command up to 84% of the available thrust. This will conserve propellant by minimizing gravity losses. The remaining thrust is used for steering and providing thrust margin. A constant-velocity phase allows the vehicle control system to reduce the effects of dynamic control lags and errors that result from following the high-thrust phase contour before shutting down the engines.

The lander, depending on initial velocity, follows the maximum or minimum contour. If the initial velocity is between the maximum and minimum, the lander will fly a contour that is a constant percentage of the distance between the minimum and maximum contour.

Simulations have shown that this approach allows margin for any 3σ combination of atmospheres, winds and surface slopes. The minimum velocity resulting from the parachute phase occurs in the maximum-density atmosphere with zero wind. The resulting trajectory has a long drop phase before intersecting the design descent contour for the high-thrust phase. The propellant required for this condition is less than that required for the maximum wind case.

The propulsion system design parameters of blowdown ratio, maximum thrust, throttle ratio, and propellant loading are defined through descent simulations using the guidance laws described above. The thrust and blowdown ratios were chosen to minimize the weight of the system.

Impact of Additional Fuel on Propulsion System

The Viking propulsion system and guidance and control laws are the result of careful analysis. They provide adequate performance with a minimum weight penalty. Adding an additional 10 kg of fuel to the current fuel tanks would require the removal of pressurant to keep the tank pressure at a level below the limits of the valves. If valves capable of taking higher pressures were used, more thrust would be available but the propulsion system would blow down differently. Viking personnel indicate that valve redesign is not practical. The diameter of the two fuel tanks can be increased from 0.6 to 0.63 m. This allows the addition of 10 kg of fuel to the current 60.1 kg of fuel and the addition of a corresponding amount of pressurant to provide identical thrust, tank pressure, and blowdown characteristics. With the implementation of the additional 10 kg of fuel, the lander can hold high-thrust levels for a longer period of time, but cannot provide instantaneous thrust higher than that of Viking '75.

Maneuver Capability

A guidance scheme must be designed for site selection maneuvering. This guidance scheme will depend on propulsion characteristics and on the site selection sensor characteristics. Because a firm sensor system design does not exist, the maneuver capability estimation was performed based on propulsion characteristics with no regard for the sensor's effect on maneuver capability. However, a discussion of maneuver capability considering sensor characteristics is presented later in this report.

Two approaches were used for maneuver capability analysis:

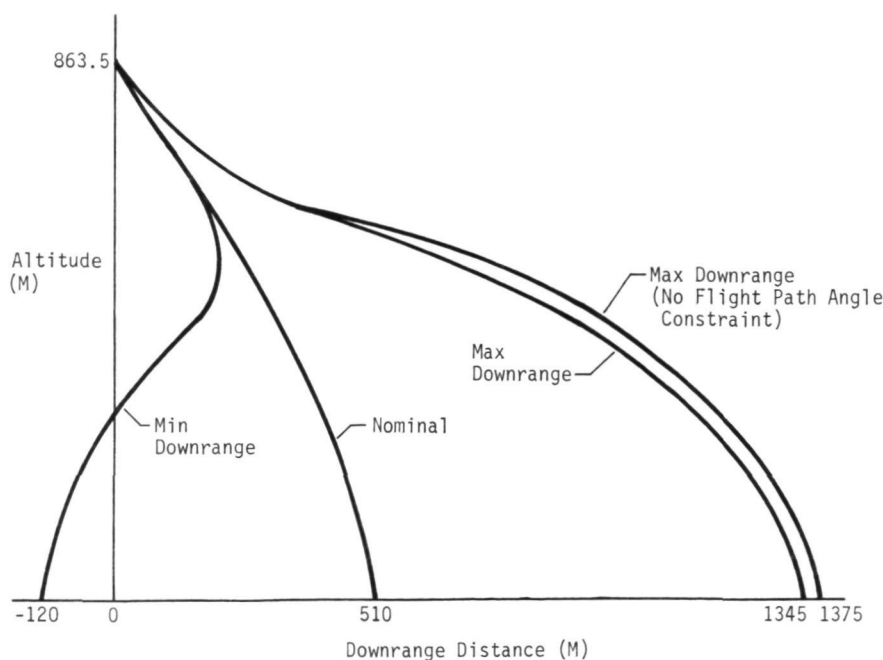
- (1) Estimate maneuver capability by performing tip-up and then perturbing the gravity turn-guidance logic for downrange and crossrange excursions;
- (2) Estimate maneuver capability by performing a gross maneuver performing tip-up and following the gravity-turn guidance logic to the ground.

In practice, a combination of the two approaches would provide considerable maneuver capability.

The following conditions existing for both approaches:

- (1) Lander weight = 645 kg;
- (2) Propulsion characteristics as described previously;
- (3) Site selection sensor constraints were ignored;
- (4) Initial altitude = 863.5 m;
- (5) Total velocity = 97.8 m/s;
- (6) Flight path angle = -50.11 deg;
- (7) Initial vehicle attitude has inertial pitch of 0 and yaw of 0; i.e., thrust vector pointed straight up. Roll was ignored;
- (8) Horizontal velocity vector is in same direction as planet rotation;
- (9) Vehicle is directly over the equator.

The initial conditions represent the maximum velocity conditions resulting from winds during the parachute phase. These conditions were used because they require maximum fuel consumption. The trajectory is plotted in Figure 68.



Analysis for maneuvering, by making small deviations from the gravity turn, was performed using the MOD6MV computer program. MOD6MV is a modularized six-degree-of-freedom trajectory program with the capability to simulate orbiting vehicles and planetary landers of various types. It is documented under NASA Contract NAS1-8913. The MOD6MV can simulate all phases of the Viking mission; however, only the terminal descent phase has been modified to include the capability of the video guidance system. Figure 69 depicts the guidance and control system for the powered portion of the terminal descent phase including the functions of the video guidance system. The MOD6MV program provided the basis for the vehicle control and dynamics. The digital simulation models that functionally describe sensor operation and the additional flight computer software for the video guidance system have been added, along with a surface model designed with the capability to generate and display a digital grey level representation of various surface features.

The throttling and propulsion portion of the program was used to determine the maximum maneuver distance possible while satisfying constraints at landing. This was done by determining the magnitude and direction of a bias velocity vector (as a function of time) that caused the lander to land at a particular point. Runs were then made to move that point away from the nominal landing point until the lander crashed. Using this technique, the small landing footprint illustrated in Figure 70 was obtained. This is a small area requiring little additional fuel, about 1.59 kg (3.5 lb). The lander follows the altitude-velocity contour except that the thrust vector is oriented to reach the desired point and not oriented opposite the velocity vector. A crash occurs when the angle between the velocity vector and the thrust vector become so large the control law cannot remove the velocity error. The control law gain was chosen assuming that thrust is opposite velocity. It appears to have the capability to remove velocity error when thrust is oriented within a limited region about the velocity vector. This allows some maneuver capability. When using a video guidance system, a control law should be designed corresponding to specific guidance system characteristics such as field-of-view and scan-positioning logic as well as propulsion characteristics.

The additional 10 kg of fuel cannot be used without a significant departure from the Viking flight plan. Additional maneuver capability for the 10 kg of fuel was determined by performing a large pitch or yaw maneuver before going to a gravity turn. This maneuver would result from VGLIS site

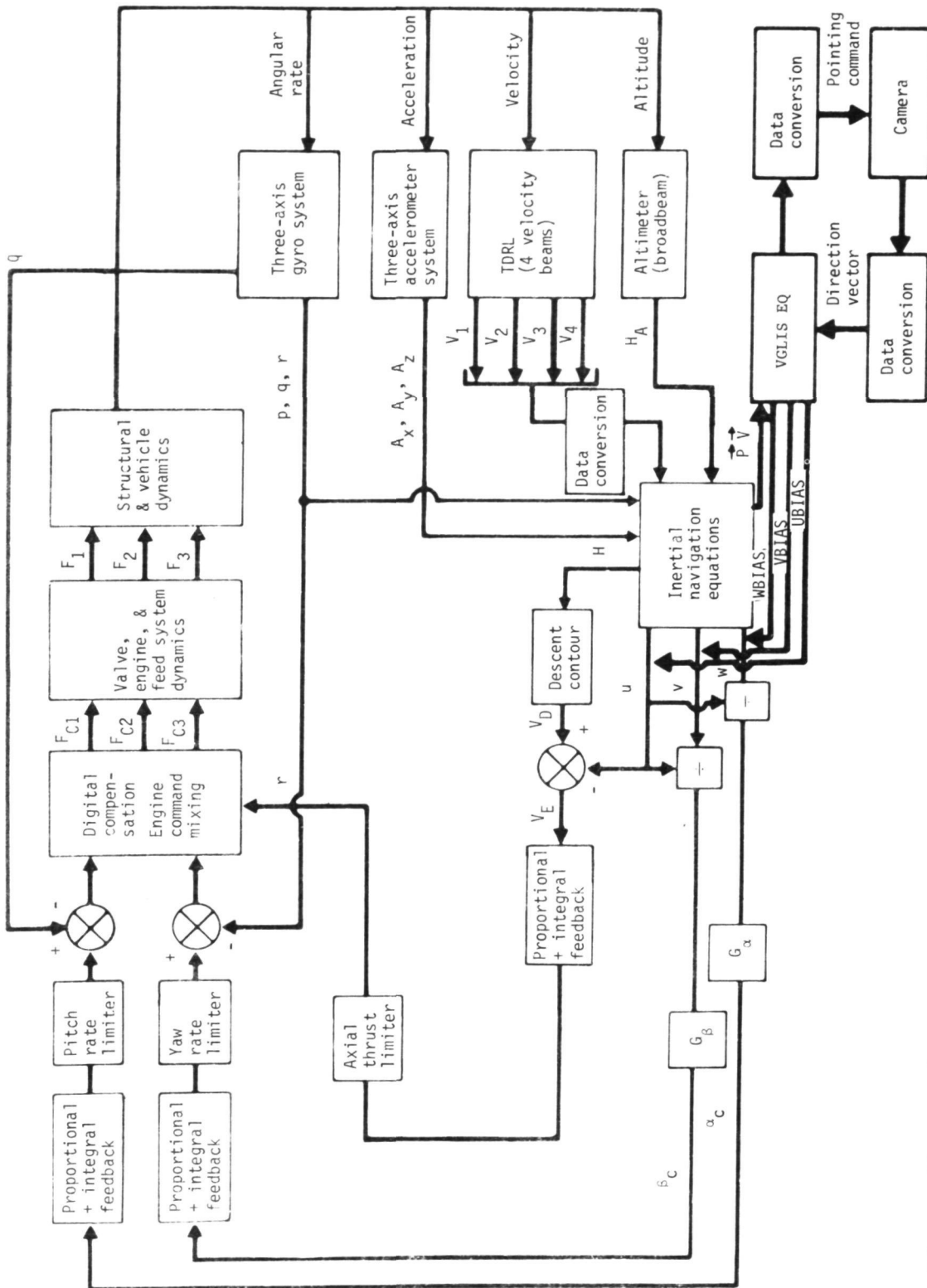


Figure 69 Terminal Descent Guidance and Control System

selection commands based on data collected during the parachute phase. The lander held this attitude and throttled at maximum thrust for a specified amount of time. Next, the lander performed the tip-up maneuver aligning the thrust and velocity vectors and followed the nominal altitude-velocity descent contour to the ground. The tip-up maneuver was performed at a high thrust level instead of the current low thrust level. The large landing envelope (Figure 70) was determined in this manner. The magnitudes of the pitch or yaw maneuver and the burn time following the maneuver were determined using the POST (program to optimize simulated trajectories) program. POST is a digital three-degree-of-freedom simulation providing the capability to optimize trajectories for launch, entry, and orbital vehicles in both atmospheric and exoatmospheric flight. The program was developed, documented, and validated under NASA Contract NAS1-10811. The generality of the program is evidenced by its N-phase capability, optimization by the discrete parameter technique, generalized targeting and stopping variables, static trim capability, oblate planet generalized atmosphere model, atmospheric winds, inequality constraints, and generalized table inputs.

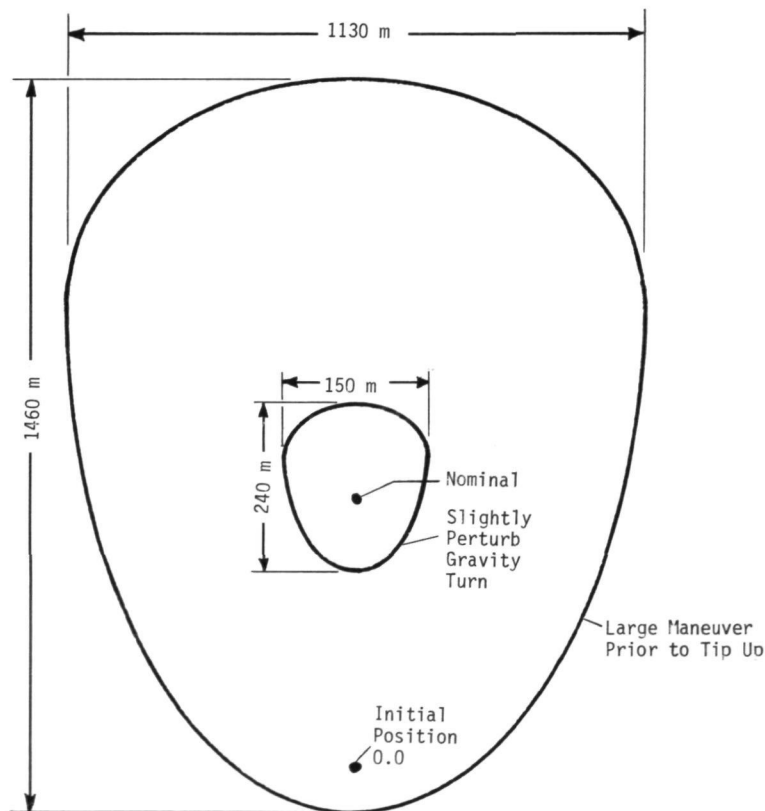


Figure 70 Maximum Maneuver Capability Footprints

This program allows modeling, by input, the Viking lander blow-down engines by a bivariant table of thrust values as a function of the remaining fuel and throttle setting. The inequality constraints allow the final velocity and attitude requirements to be met before landing. A program module is provided for implementing steering and throttling laws. Program statements were added to the module for computing the accelerations required to follow the terminal descent contour after the maneuver.

A brief description of the program operation will be given to clarify the selection of maneuver parameters.

We can find the point (X, Y) that lies within the circle $X^2 + Y^2 = 4$, for which X is a maximum (Figure 71). The answer is $(2, 0)$ but suppose the problem cannot be solved by inspection. Using the optimization technique in POST, one would make a guess at the answer and POST would attempt to find the actual solution. Suppose we made an initial guess of $(-3, 3)$, as indicated in the figure. POST would first check if the guess satisfied the constraint that the point lies within the circle $X^2 + Y^2 = 4$. It does not, so POST chooses the closest point on the circle. Now that the constraint is satisfied, POST tries to maximize X .

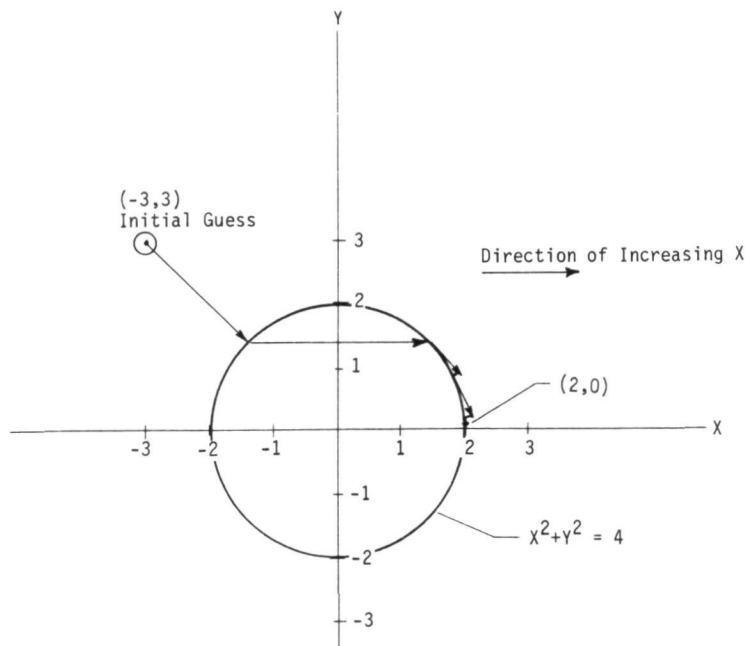


Figure 71 Post Optimization Algorithm

A new point is chosen in the direction of the gradient of X; i.e., the direction in which the magnitude of X increases most rapidly. This point must also satisfy the constraint. The point chosen has the same Y-coordinate but a larger X-coordinate. Next POST would take a series of steps around the circle as illustrated (Figure 71) until the value of X is a maximum and the point (2, 0) is selected.

This optimization and targeting capability was used to determine the parameters to achieve maximum maneuver capability.

Consider the case of maximizing the downrange maneuver distance. A profile to increase downrange distance from that obtained by following the nominal trajectory would consist of a pitch maneuver to an attitude permitting the vehicle thrust to decrease the range direction. After this attitude is reached, full thrust is applied for a specified time. Then the tip-up maneuver is performed; that is, another pitch maneuver is performed to thrust opposite the velocity vector and the terminal descent contour is followed to the ground.

POST was used to determine the magnitude of the pitch angle and the duration of the burn that will give maximum downrange travel subject to constraints on final velocity and attitude. The initial investigation revealed that the portion of the Viking control law programmed in POST had no difficulty in eliminating velocity errors after the maneuver and in following the altitude-velocity contour to the ground. Thus, all landing velocity and attitude requirements were met. It became apparent that it was not necessary to simulate the trajectory all the way to the ground.

Because no maneuvering is allowed during the constant-velocity phase, all digital simulations were terminated at an altitude of 13.72 m (45 ft). This is valid provided there is adequate fuel, 6.12 kg (13.5 lb), remaining to complete the descent. Fuel consumption during the constant-velocity phase is approximately 0.46 kg/m (0.3 lb/ft). On the advice of Viking project personnel, the remaining fuel was increased to 6.8 kg (15 lb) to allow some margin. The problem solved by POST then became: Determine the magnitude of the pitch maneuver and the duration of the burn that will yield maximum downrange distance subject to the constraint that there will be at least 6.8 kg (15 lb) of fuel remaining at an altitude of 13.72 m (45 ft). The solution to this problem was:

Pitch angle = -21.83 deg

Burn time = 3.59 sec

Downrange = 1376.8 m(4517 ft)

Remaining fuel = 6.8 kg (15 lb)

The resultant trajectory is plotted in Figure 65. During this flight, the vehicle flight-path angle (measured from local horizontal to velocity vector) came to -11 deg. This could cause radar lock to be lost (the limit is -15 deg). Viking project personnel indicated that loss of lock for less than 10 sec would not cause any problems. Table IV presents the history of values obtained by POST to solve this problem.

Table IV Post Iteration History

Iteration Number	Pitch Deg	Burn Time, s	Remaining Fuel, kg	Maximum Flight Path Angle, Deg	Down Range Dist, m	Comments
0	-60.0	1.5	2.13	-17.73	1370	This is initial guess; note fuel error.
1	-59.9	1.49	2.29	-17.8	1360	Fuel is improving.
2	-48.8	1.42	6.85	-19.4	1245	Both constraints are satisfied. Note loss in downrange.
3	-41.2	1.96	6.95	-17.7	1290	Both constraints still satisfied. Downrange improved.
4	-32.4	2.68	6.79	-15.0	1345	Solution--fuel and flight path angle are at limits.

Table V summarizes the final values for maximum and minimum downrange (Figure 68), and maximum crossrange (Figure 72).

Table V Maximum Maneuver Distances

	Attitude Maneuver, Deg	Burn Time, s	Maneuver Distance, m
Maximum downrange	Pitch - 32.4	2.68	1345
Minimum downrange	Pitch + 55.6	7.11	-120
Maximum crossrange	Yaw \pm 31.8	3.83	570

These numbers represent estimates of maneuver distances that can be obtained by expending all available fuel in an optimum manner for the initial conditions previously described. Additional maneuver capability can be obtained with the same fuel allotment by beginning to maneuver at a higher altitude. The lander velocity vector is relatively constant during the last 300 m of the parachute phase and the site selection process could start at any time by jettisoning the parachute earlier.

Considerations for designing a control law for a video guidance landing and imaging system must evaluate the characteristics of the site selection sensor and the associated gimbal authority and scan positioning logic.

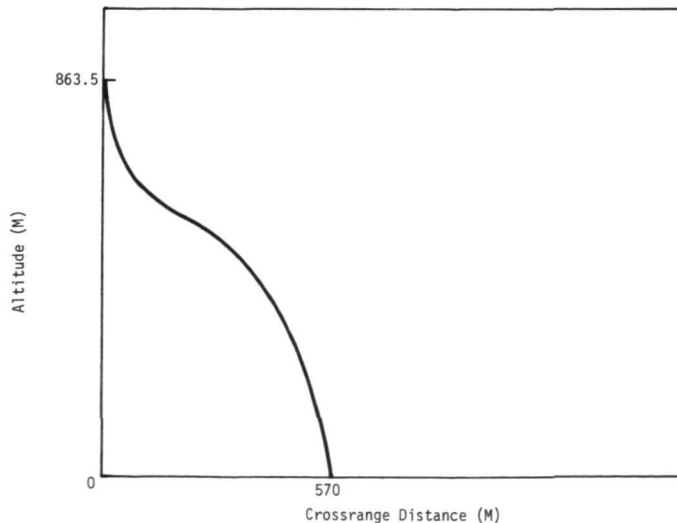


Figure 72 Crossrange Maneuver Capability

A vehicle such as Viking must perform an attitude maneuver in order to perform a crossrange or large downrange maneuver. The new vehicle attitude may make it impossible to see the point to which it is flying, depending on sensor gimbal authority.

Effects of Scan Positioning

The effects of scan positioning logic are more subtle. For example, previous work* presented a sensor system with an instantaneous field-of-view of 12 deg broken up into nine areas. The impact point was predicted and the scan was centered about it. The center of one of the nine areas was chosen as a more desirable impact point and the necessary maneuvers were begun to reach that point at the time of impact. One second later a new impact point was predicted. This prediction assumed that the maneuvers already performed would be the only maneuvers performed. Thus, the new predicted impact point lies on a line between the original impact point and the center of the area selected by the previous scan. This process continues until the lander reaches a minimum operating altitude. The site selection logic always chooses a point within its current field-of-view, and the size of the field-of-view is always decreasing. The net effect of this process is illustrated in Figure 73, which shows how the field-of-view decreases with altitude and how the predicted impact point moves. The upper right-hand corner was chosen as the desired landing site after every scan. This represents the maximum maneuver capability for this particular landing site selection system. Note that the propulsion system is not the only limiting factor. The limiting factors were that each successive scan was positioned close to the previous scan and that the field-of-view decreased with each step. Nevertheless, this landing site selection system was stable and effective.†

A landing on the simulated surface depicted in Figure 74 was attempted using this landing site selection system. The series of pictures in Figure 75 illustrates the visual aspects of this landing. Moving from left to right and top to bottom, the field-of-view decreases in size and increases in detail as the lander descends and ground resolution improves.

*R. T. Schappell and G. R. Johnson: "Experimental and Simulation Study Results of a Planetary Landing Site Selection System." Journal of Spacecraft and Rockets, Vol. 10, No. 4, April 1973, pp. 277-280.

† Ibid. R. T. Schappell

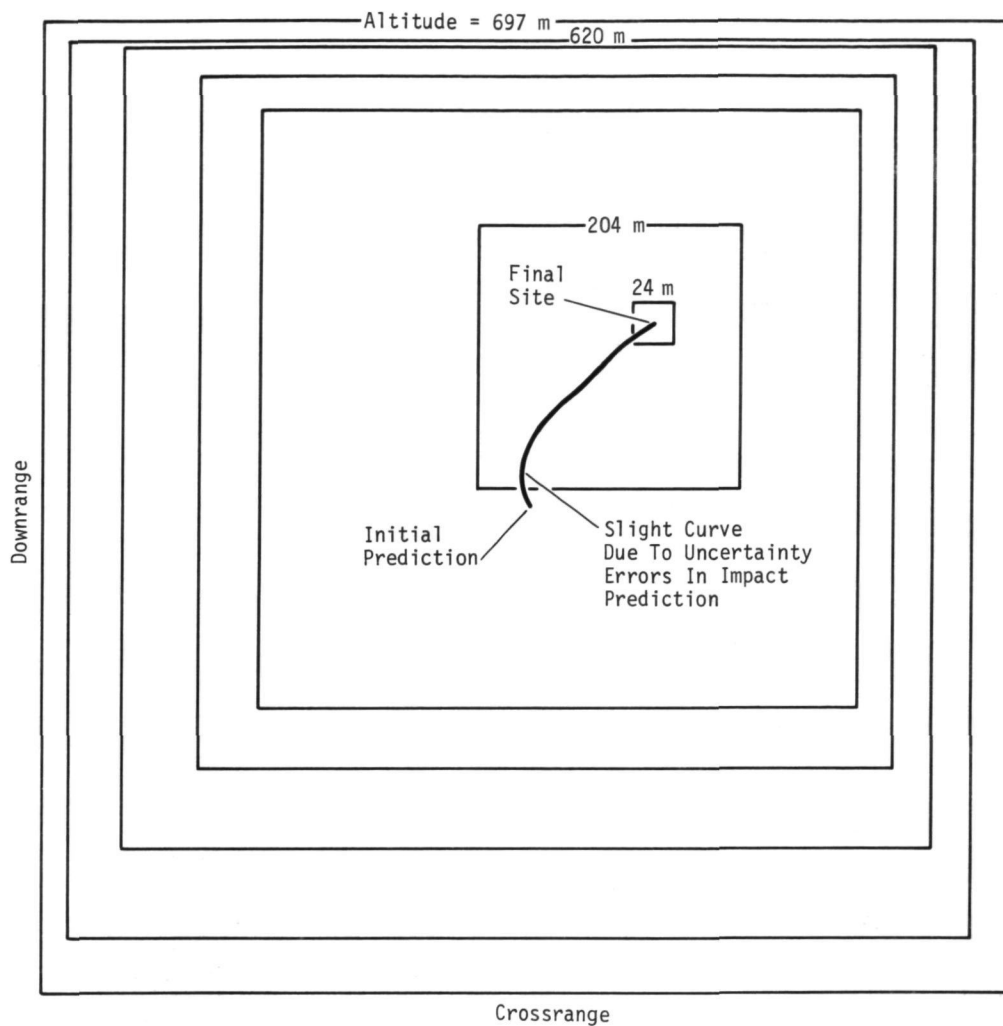


Figure 73 Scan Always Centered at PIP

The arrows under each picture indicate the maneuver direction chosen based on surface characteristics. The last three pictures are not full size because the digital surface grid point spacing does not allow enough points to plot at the full size and maintain reasonable "picture quality."

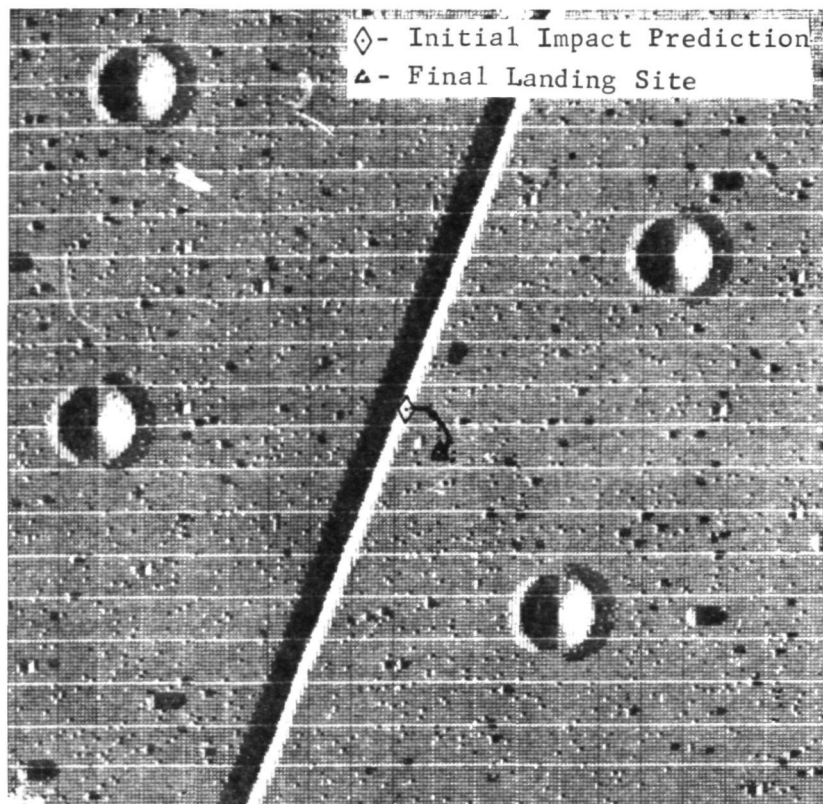


Figure 74 Digital Surface Simulation

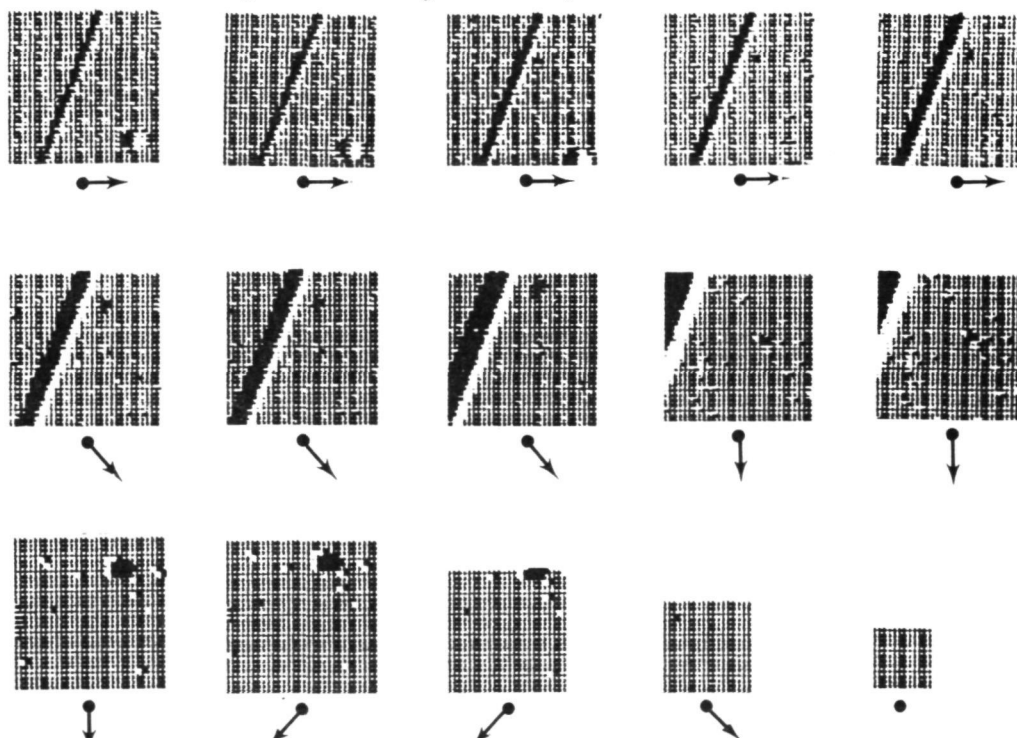


Figure 75 Digital Simulation of Sensor Field of View

Maneuver capability can be increased by positioning the scan differently. For example, the scan could be centered about the preferred landing site (a, Figure 76). This could cause points to be chosen outside of the initial field-of-view and to ultimately choose a point that was out of maneuver range. This process would not make efficient use of fuel since additional downrange or crossrange could be requested as altitude decreases.

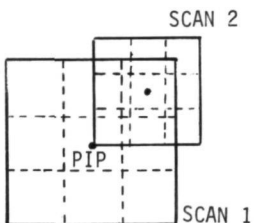
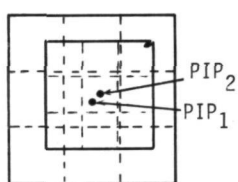
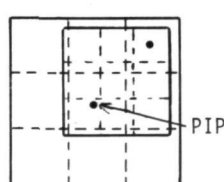
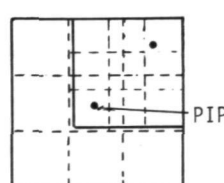
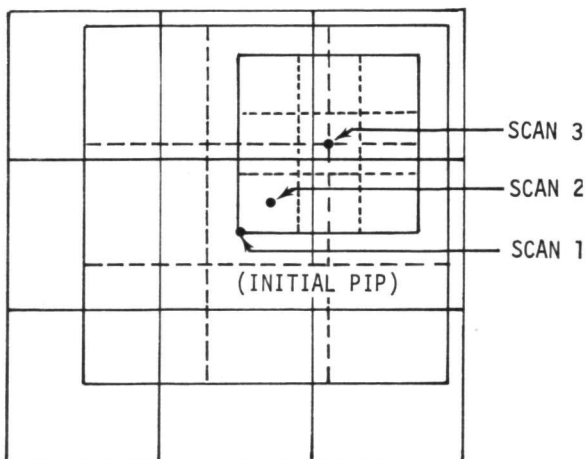
<p>a</p> 	<p>First scan is centered at PIP and subsequent scans are centered about the most recently selected area. This implementation can bring new data into the field of view and puts extreme requirements on maneuver capability because desired landing point can get farther away from initial PIP with every decision.</p>
<p>b</p> 	<p>First scan is centered at PIP, the best area is selected, and maneuvering begun. A new PIP is predicted and the second scan is centered about it. This continues to a minimum operating altitude. Here the scan positioning depends entirely on the response time of the maneuvering system. With a slowly responding system maneuver, range will be restricted because the size of the field of view decreases during descent, and the new scan is never moved very far from the previous scan.</p>
<p>c</p> 	<p>First scan is centered at PIP. Subsequent scans are positioned so that the coordinates of the center of the subframe, chosen during the last scan, correspond to the coordinates of the center of the same subframe for the next scan. This scheme puts very little strain on the maneuver system since the largest maneuver is commanded at the highest altitude. It is not possible to steer to all points in the original field of view.</p>
<p>d</p> 	<p>First scan is centered at PIP. Subsequent scans are moved toward the best site but restricted to previous field of view. All of the original field of view is available for a landing provided the maneuver system steers toward the edge or corners of the original field of view.</p>

Figure 76 Scan Positioning Logic Summary

In addition, new surface features are being processed during descent. This makes it possible to land on a large feature that would have been avoided if it had been included in the original field-of-view.

In the third approach, the initial scan is centered at the lander's predicted impact point. Subsequent scan positions are determined by the most recent landing site choice. The scan is positioned so that the coordinates of the center of the subframe chosen during the last scan are the coordinates of the center of the corresponding subframe for the next scan. For example, with 3x3 subframes, if the first two decisions choose the upper-right subframe as the best area, the scan positioning would be as shown in Figure 77. Note that the coordinates of the center of the upper-right subframe remain constant. This implies that the range of the lander is limited to the area bounded by the center of the outside areas of the 3x3 scan. MOD6MV runs were made to verify that these points were within maneuver range with the 12 deg field-of-view. The resultant traces of the predicted impact point for some of the areas are shown in Figure 78.

A fourth scan-positioning technique is implemented by centering the scan at the initial predicted impact point and then



*Figure 77 Scan Positioned by
Requiring Selected
Area Coordinates to
Remain Constant*

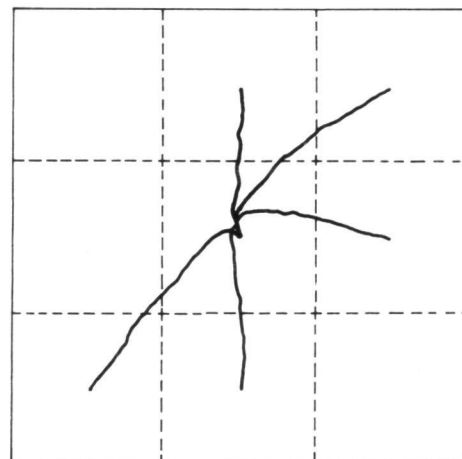


*Figure 78 Predicted Impact
Point Traces for
Landings*

positioning the next scan by moving it toward the selected site until the new field-of-view has a common boundary with the previous scan. Figure 79 shows a predicted impact point trace for a landing in which every decision chose the upper-right corner. This resulted in a crash because the desired landing point moved farther away from the initial predicted impact point with every step. This crash could have been avoided by changing the steering philosophy. That is, if the lander were steered toward the corner of the upper-right area instead of the center, it would have been able to maneuver to the ultimate landing site from the highest altitude. As it was implemented, the size of the required maneuver increased as the maneuver range decreased.

All four of these techniques are summarized in Figure 76.

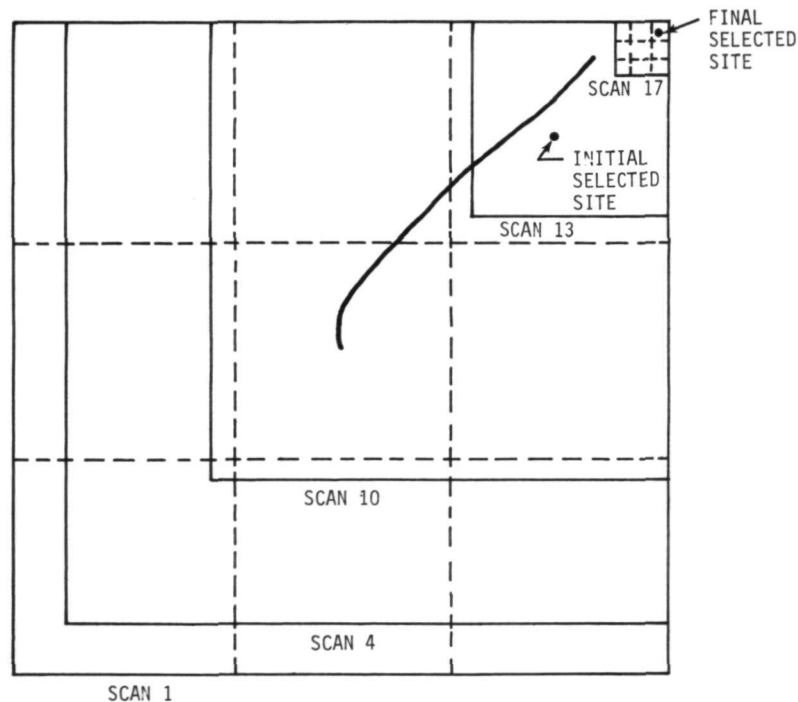


Figure 79 Scan Positioned by Moving to Boundary of Previous Area

SCIENTIFIC IMAGING CONSIDERATIONS

Introduction

The availability of the VGLIS camera onboard the lander raises the obvious and scientifically stimulating prospect of using the camera in a scientific imaging mode to record or transmit photographs of the landing site during the entry phase of the planetary landing. This capability will allow the scientific investigator to correlate geomorphologic features identified from orbital photographs with terrain features observable in postlanding ground scan cameras. The achievable benefits of imaging at lower altitudes are higher resolution, precise reconstruction of the landing site, and the ability to select desirable traverses for a planetary rover.

This study phase assesses the technical feasibility of adapting the VGLIS camera in an imaging mode for a future Viking Mars Lander Mission, using as much of current Viking Lander/Orbiter data handling and transmission capability as possible.

System Operation

Camera Characteristics

The VGLIS uses an image dissector camera, which has specific advantages for a scientific imaging mission. Its output is completely independent of scan rate and previous scan history. Its sensitivity is limited only by the random fluctuations of the scene-generated photoelectrons. The VGLIS has a high limiting resolution and is relatively insensitive to platform slewing.

The system's scanning is adaptable and capable of covering all or any part of the total field-of-view of the 60-deg diameter instrument. The scientific imaging scan mode does not need to be the same as that used in terminal phase guidance or even stay in a fixed mode during entry. Pictures taken early in entry (800,000 ft) where the flight path angle is very shallow (-15 to -17 deg), will show mostly outerspace in a 60-deg field-of-view. In this case, it would be desirable to cut down the field-of-view (and number of bits generated per picture) to look at the predicted impact point in much the same way as the terminal video guidance system. At a lower altitude, perhaps just prior to parachute jettison, it might be desirable to take a picture with the total field-of-view to see as much of the terrain around the landing site as possible. We will, therefore, take a

look at both narrow and full field-of-view applications of the camera.

The camera scan rate will be chosen in a trade-off between image distortion which may result from vehicle dynamics if the frame rate is too low (4-6 frames/sec) and high picture generation bit rate which exceeds the data transmission link capability if the scan rate is high (20-30 frames/sec).

Camera Resolution

The theoretical camera resolution described here assumes a high quality lens, adequate lighting of the target and no atmospheric degradation. Resolution depends, to a high degree, upon the camera-scanning aperture diameter (presently 0.0014 in). This limits the size of the smallest image that can be dissected at the photocathode of the tube. The present VGLIS camera photocathode diameter is 0.75 in. This implies that the best resolution at the photocathode is achieved when the scan lines are separated by 0.0014 in (536 lines across the diameter of the tube). The camera resolution is defined by the following equation:

$$r = \frac{a \cdot h}{f_e}$$

where r = resolution in meters at the ground target
 a = scanning aperture diameter, 0.0014 in.
 h = slant range to target in meters
 f_e = effective focal length of camera, in.

but, $f_e = \frac{d}{2 \cdot \tan(\theta/2)}$

where, θ = field-of-view of camera, 60 deg
 d = diameter of cathode, 0.75 in.

therefore, $f_e = \frac{0.75}{2 \cdot 0.577} = 0.65 \text{ in.}$

$$r = \frac{0.0014}{0.65} \times h = 2.154 \text{ } h \times 10^{-3}$$

The camera resolution in meters from various points during a typical Mars mean atmospheric entry is shown in Table VI.

Table VI Camera Resolution Versus Time

Time, sec	Event	Camera Resolution, m
0	Atmospheric Entry (800,000 ft)	3027.
100	Potential Data Link Blackout begin	2105.
240	Potential Data Link Blackout end	750.
498	Parachute Deployment (30,000 ft)	40.
528	After Roll Maneuver (12,500 ft)	10.
550	Terminal Descent Engine Ignition	
	(3,800 ft)	2.5
	At 100 m altitude	0.22

The VGLIS camera resolution is seen to be better than the 20-m orbiter camera resolution only after the roll maneuver during parachute descent. At higher altitudes, the VGLIS imaging would be useful primarily for keying later photographs from major terrain features.

Viking Data Link Capability

Although VGLIS scientific imaging is not constrained for future planetary missions to use the Viking data link and transmission system, it is considered typical of the capability and problems that will be encountered in any future system. The Viking system is examined to see what implications it might have on the VGLIS scientific imaging mode.

The Viking Mars lander can transmit data to the orbiting spacecraft whenever the orbiter is within line of sight. The orbiter then records the data for later transmittal to Earth or the orbiter may act as a direct S-band relay link to Earth. The data link between lander and orbiter operates at either a low bit rate of 4 kilobits per sec (kbps) or a high bit rate of 16 kbps. The relay link operating modes summarized in Table VII also show that transmitted power can be 30, 10 or 1 W. Both lander and orbiter have tape recorder storage capability of 4×10^7 bits of data.

The present Viking data link operates at the low bit rate (4 kbps) and 10 W of power during entry down to parachute deployment. The power is limited to 10 W in order to minimize an on-board heating problem, and the low bit rate lowers the bandwidth requirement of a marginal relay link back to Earth.

Table VII Viking Relay Link Operating Modes

MISSION PHASE*	ORBITER MODE	LANDER MODE
Checkout Modes (Relay link bit error rate shall not be specified.)	RRS/RTS Receive MDS in Relay Telemetry Data Position (S-Band Feedthrough Operative) for 4 KBPS Data 4 KBPS & 16 KBPS Data is recorded	Transmitter on at 1 watt and 4 KBPS for 3 minutes ** Transmitter on at 30 watts 1 and 4 KBPS for 1 minute Transmitter on at 30 watts 1 and 16 KBPS for 2 minutes Transmitter on at 10 watts and 16 KBPS for 1 minute.
Separation to Deorbit Burn Complete (Orbiter receiver may overload immediately after separation but shall operate within specifications prior to deorbit burn initiation minus 0.5 minutes)	RRS/RTS Receive Data Recorded at 4 KBPS S-Band Feedthrough Operative	Transmitter on at 1 watt and 4 KBPS
Deorbit Burn Complete to Entry Minus 180 Minutes (25 second transmission period each 24 minutes)	RRS/RTS Receive Data Recorded at 4 KBPS S-Band Feedthrough Operative	Transmitter on at 1 watt and 4 KBPS
Entry minus 180 minutes to Entry minus 100 minutes (25 second transmission period each 12 minutes)	RRS/RTS Receive Data Recorded at 4 KBPS S-Band Feedthrough Operative	Transmitter on at 1 watt and 4 KBPS
Entry minus 100 minutes to Entry minus 40 minutes (25 second transmission period each 6 minutes)	RRS/RTS Receive Data Recorded at a 4 KBPS S-Band Feedthrough Operative	Transmitter on at 1 watt and 4 KBPS
Entry minus 40 minutes to Aerodecelerator phase (continuous operation) (Degraded performance may occur for worst case conditions whenever the entry attitude maneuver occurs prior to entry minus 15 minutes) (Interruption of the link may occur as a result of communications blackout.	RRS/RTS Receive Data Recorded at 4 KBPS S-Band Feedthrough Operative	Transmitter on at 10 watts and 4 KBPS. Data recorded.
Aerodecelerator Phase to landing (A maximum of 10 seconds of degraded performance may occur as a result of parachute oscillations and a maximum of 12 seconds of degraded performance during Lander tip-ups at vernier ignition)	RRS/RTS Receive Data Recorded at 4 KBPS S-Band Feedthrough Operative	Transmitter on at 10 or 30 watts and 4 KBPS
Landing to Orbiter Set 12-15 minute Horizon Scan	RRS/RTS Receive Data Recorded at 16 KBPS	Transmitter on at 30 watts and 16 KBPS
Post Landed (Synchronous Orbiter) 20-40 minutes	RRS/RTS Receive Data Recorded at 16 KBPS	Transmitter on at 30 watts and 16 KBPS
Links of Opportunity, (Non-Synchronous Orbiter) Post Landed 58-63 days	RRS/RTS Receive Data Recorded at 4 or 16 KBPS	Transmitter on at 30 watts and 4 or 16 KBPS
Resynchronization of Orbiter, Post Landed	RRS/RTS Receive Data Recorded at 16 KBPS	Transmitter on at 30 watts and 16 KBPS
Contingency Mode	RRS/RTS Receive Data Recorded at 4 KBPS	Transmitter on at 1 or 10 watts and 4 KBPS

*When links are available they are continuous unless otherwise specified.

**Includes 50-second warmup

NOTE: Each transmission period will be preceded by a 50-second transmitter warm-up period with modulated data present.

From parachute deployment to landing, the low bit rate still is used because of the marginal relay link. Maximum power is used to increase the probability of getting data return during this short but very important phase of the flight. After touchdown, the lander transmits at high power and high bit rate until the orbiter passes over the horizon. During this 12 to 15-min period, the data link is transmitting ground scan camera data. From then on, for 50 to 90 days, the lander transmits for 20 to 40 min at high power and high bit rate every time the orbiter passes within transmission range.

Entry Vehicle Dynamics

The entry vehicle dynamic motion considerations affect the VGLIS imaging system in two ways. First, some of the entry vehicle attitudes dictated by performance and heating requirements produce marginal antenna patterns and make the data relay link unreliable. Second, attitude rates have the effect of causing camera image distortion. Table VIII summarizes the attitude rates and attitude perturbations that are likely during entry.

Table VIII Viking Entry Dynamics

	<u>Pitch</u>	<u>Roll</u>	<u>Yaw</u>
<u>Entry (800,000 feet)</u>			
Rates, Deg/Sec	1	15*	1
Attitude Perturbations	.5	74*	.5
<u>Parachute Deploy to Aeroshell Separation (0-7 Seconds)</u>			
Rates, Deg/Sec	100	1	100
Attitude Perturbations	15	.5	15
<u>Aeroshell Separation to Roll Maneuver</u>			
Rates, Deg/Sec	30	15	30
Attitude Perturbations	25	180	25
<u>After Roll Maneuver to Impact</u>			
Rates, Deg/Sec	10	1	10
Attitude Perturbations	25	.5	25
*Apply only to roll maneuvering mode using landmark navigation.			

There are several periods during entry where attitude changes and attitude rates are significant enough to preclude use of Video imaging or the data transmission link. The first occurs 15 min before entry (defined as 800,000 ft) where an attitude maneuver occurs to orient the vehicle for entry into the planetary atmosphere. A potential data link blackout of 60 sec occurs somewhere between 100 and 240 sec after entry. The next period involves attitude rates from 100 to 30 deg/sec immediately after parachute deployment. The aeroshell which provides aerodynamic heating protection is separated from the lander 7 sec after parachute deployment. A roll maneuver to a desired ground heading is executed at 15 deg/sec, 10 sec after parachute deployment. Finally, a tip-up maneuver to back out the ground wind is executed during the 5 sec after terminal descent engine ignition.

The most desirable time for scientific imaging appears to be during entry if an optical window is available in the aeroshell or between the roll maneuver and terminal descent engine ignition during parachute descent.

Image Distortion

The image dissector camera is not subject to picture smear in the usual sense of the word. If one image is generated in 1 sec with 100 lines and 100 picture elements (pixel) per line, each pixel has an effective shutter speed of 10^{-4} sec. The image can be distorted by vehicle motions where succeeding scan lines are shifted in position. This type of distortion can be eliminated by postflight reconstruction of the image if the vehicle rates are known. A more desirable objective would be to limit imaging to flight times where vehicle rates are below a level that will ensure good picture quality. The Viking airborne computer is capable of deriving vehicle rates as low as 0.019 deg/sec and could provide the intelligence to the camera system to negate imaging above a specified rate.

In order to determine the vehicle rates that provide good picture quality, a criterion is established that vehicle rates and/or imaging scan rates will be selected so that no adjacent lines will overlap more than 10%. Another way of stating this is to limit the motion of the terrain in the camera field-of-view to no more than 10% of the scanning rate of the camera. Vehicle rates meeting the above criterion at various frame rates are tabulated below for the full screen field-of-view of 42 deg (360 lines/frame, 360 pixels/line) and for a reduced field-of-view of 21 deg (180 lines/frame, 180 pixels/line).

<u>Scan Rate</u>		<u>Vehicle Rates - Deg/Sec</u>	
<u>Frames/Sec</u>	<u>Sec/Frame</u>	<u>42° FOV</u>	<u>21° FOV</u>
0.5	2	2.1	1.05
0.666	1.5	2.8	1.4
1.0	1.0	4.2	2.1
2.0	0.5	8.4	4.2
4.0	0.25	16.8	8.4
8.0	0.125	33.6	16.8

A brief study of the rate profiles in pitch and yaw for a typical gusty parachute descent in the mean Mars atmosphere (Figs. 77 and 78) show that an image lock setting of 2 to 3 deg/sec would scarcely allow any imaging.

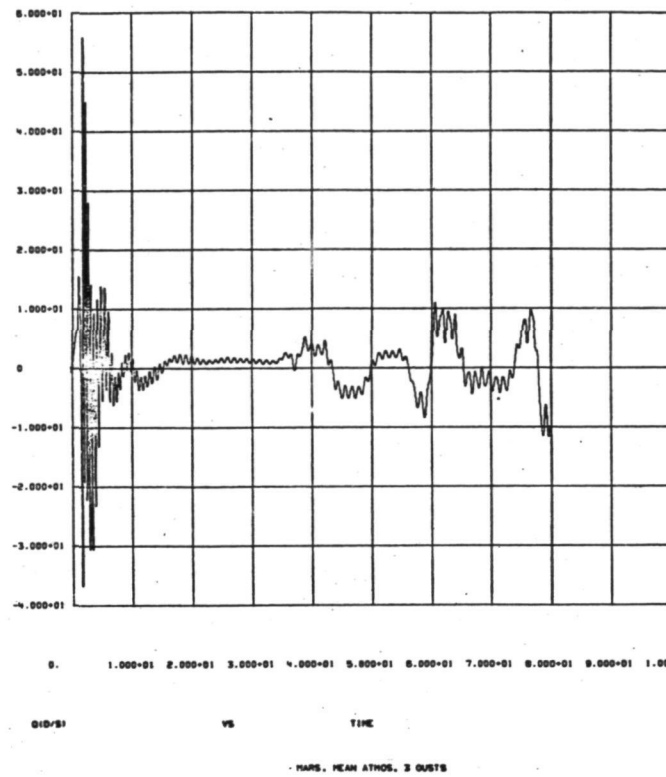


Figure 80 Pitch Rate during Parachute Descent

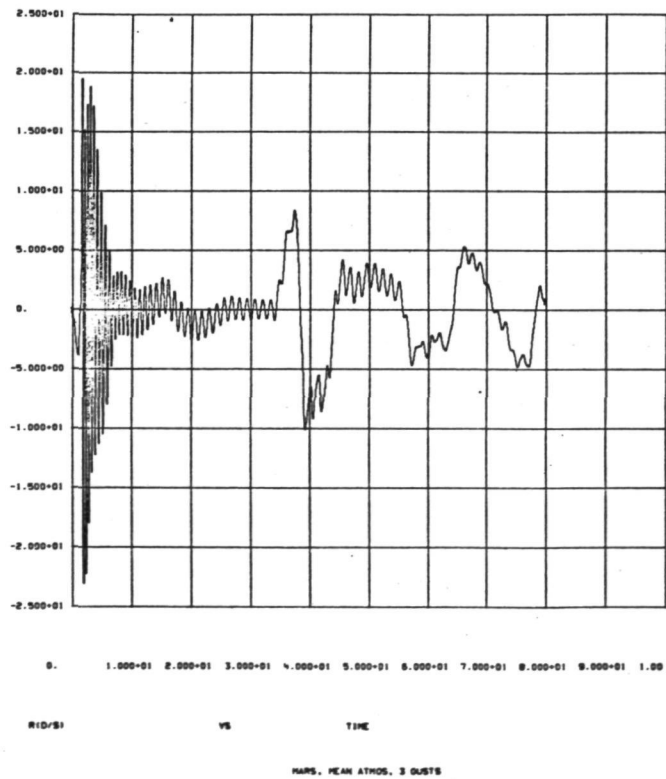


Figure 81 Yaw Rate during Parachute Descent

A cut-off setting of 4.2 deg/sec would provide the minimum acceptable time for imaging. Therefore, the imaging scan rate should be 1 frame/sec or higher for the full field-of-view and 2 frames/sec or higher for the reduced field-of-view. It should be noted that the lower frame rates produce a better signal to noise ratio for the imaging system. Frame rates above 4 sec for the reduced field-of-view would produce a signal-to-noise ratio of less than 10 to 1 rms which is not favorable.

Typical Data Storage and Transmission Requirements

The most desirable imaging system would be capable of generating a series of perhaps ten nested images starting well before entry and continuing down to terminal descent engine ignition. It would be desirable to be able to transmit such images to the orbiter before touchdown to save the data in the unlikely event of a catastrophic landing. The data storage and transmission requirements of these features pose problems for the Viking data link capability. Table IX shows the storage and transmission time required for a single picture using either the full or reduced field-of-view image. Two bits per picture element are assumed to convey four shades of gray in the image.

Table IX Viking Data Storage and Transmission

FOV, deg	LINES/ SCAN	SCAN RATE FRAME/sec	NO. OF BITS IMAGE	DATA GENERATION	IMAGE TRANSMISSION	
				RATE BITS/sec	TIME, sec 4 kbps	16 kbps
42	360	1*	259,200	259,200	64.8	16.2
21	180	2*	64,800	129,600	16.2	4.05
7	60	6*	7,200	43,200	1.8	0.45
7	60	0.55	7,200	4,000	1.8	0.45
7	60	2.22	7,200	16,000	1.8	0.45

The system characteristics (Table IX) are not the only ones that could be selected, but they are based on the following conditions:

- (1) The full field-of-view (42 deg) provides the largest square image without corner cut-offs.
- (2) The number of lines/scan were chosen in each FOV to provide optimum resolution at the photocathode.

- (3) Scan rates marked with an asterisk (*) provide acceptable image distortion with vehicle rates up to 4.2 deg/sec. The other combinations were selected to get the data bit rate low enough to meet the real time data link transmission bit rate. There would be a high risk of image distortion associated with these images.

Conclusions and Recommendations

The following implications may be drawn for an imaging system applied to the current Viking data storage and transmission capability.

- (1) The data storage capability on both lander and orbiter of 4×10^7 bits can readily handle 10 images of the size envisioned for VGLIS scientific imaging without saturating the storage capacity.
- (2) Image size and distortion quality would have to be compromised to allow images to be transmitted in real time to the orbiter before touchdown.
- (3) Probably the best compromise system would be a 21-deg field-of-view that is aimed at the predicted impact point through electronic scan control. A 2-frames/sec scan rate and 180 lines/scan would generate 64,800 bits/image at a bit rate that exceeds the real-time link bit rate. Selected images would, therefore, be stored on the lander tape recorder and retransmitted at the high bit rate before touchdown. The transmission time of 4.05 sec per image would allow several high priority images to be transmitted to the orbiter in the 50-odd sec between aeroshell separation and terminal descent engine ignition.
- (4) Other lower priority images could be stored on the lander for transmission to the orbiter after touchdown.
- (5) VGLIS scientific images are expected to provide best resolution and scientific application during the parachute descent phase of a Viking-type mission.
- (6) Image distortion can be minimized by imaging only when the airborne computer indicates vehicle rates are below a specified level.

SUMMARY AND RECOMMENDATIONS

The results of this study show that an imaging system can be mechanized to provide a spacecraft or satellite with a considerable amount of adaptability with respect to its environment. It will provide a level of autonomy essential to many future missions and will also enhance their data gathering ability.

This section summarizes the study results and contains an approach for applying this technology to specific scientific objectives for future missions. As an example, the landmark acquisition and tracking system should be considered as a future shuttle experiment for instrument pointing and for constituent tracking purposes. These applications and the achievable benefits are summarized in Tables X, XI, and XII in this chapter.

Planetary Landing Site Selection System

The feasibility of an autonomous video guidance system capable of observing a planetary surface during terminal descent and selecting the most acceptable landing site was successfully demonstrated in the laboratory. The system was breadboarded and flown on a physical simulator consisting of a control console, a dynamic simulator, and a PDP-9 computer. The breadboard system consisted of an image dissector camera and the appropriate processing logic. Feasibility was established by performing repeated flights to a number of three dimensional scaled surface models such as that shown in Figure 82. The dots indicate the landing sites selected as a result of automated flights to the surface starting at random points above the surface model.

A goal of the scientific community has been to land commanded planetary vehicles close to areas of high scientific interest. Unfortunately, the current techniques result in large landing site dispersions because of orbit position errors, deorbit maneuver errors, vehicle L/D uncertainties, and atmospheric uncertainties including winds. The Viking '75 lander, for example, has an elliptical landed footprint of 300x100 km that results from a statistical combination of these errors. For this reason, a landmark navigation system is being considered for future missions. In the performance of this study, we determined that a Viking-type vehicle could be maneuvered during the entry phase of flight by rolling the spacecraft to orient the vehicle lift vector. The results of the simulation effort

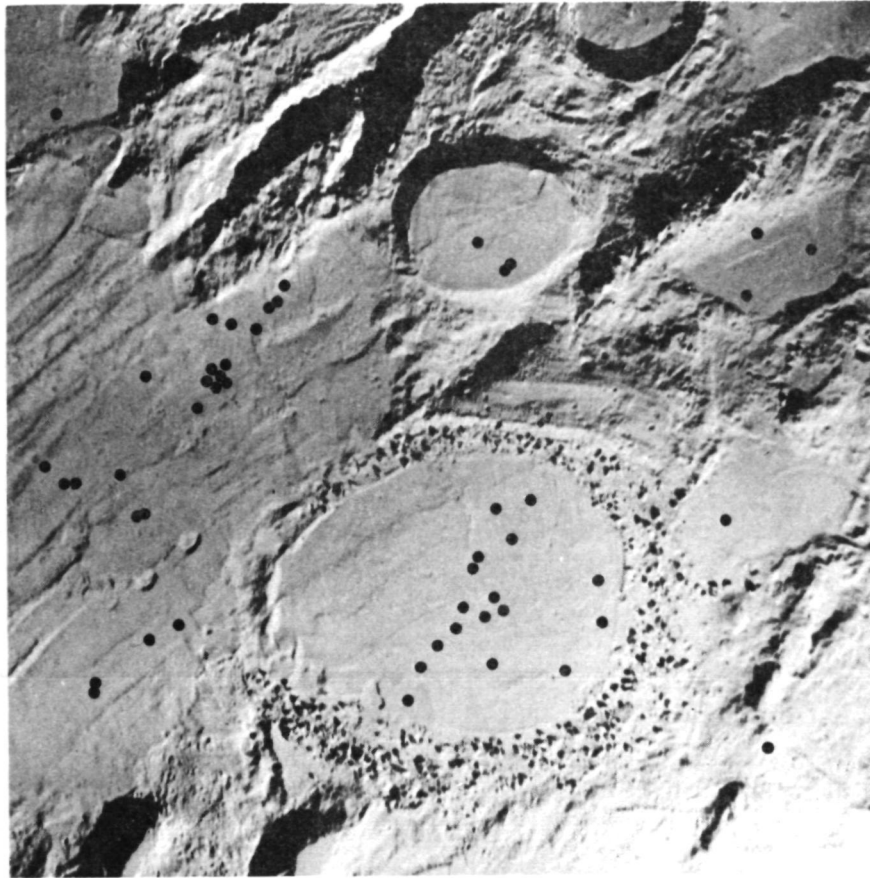


Figure 82 Monte Carlo Experiment Results

indicate that a maneuvering system using roll control of the lift vector on the Viking spacecraft can be successfully mechanized to remove 50% of the current landing impact dispersions during the earlier phase of the flight.

Scientific site selection laboratory experiments were also conducted demonstrating the ability of the video guidance system to target an area of contrast during the terminal descent phase and generate the bias steering commands to maneuver towards it in order to enhance postlanded scientific exploration. During the latter phase of the scientific site selection flight, the system reverts to the obstacle-avoidance mode in order to prevent catastrophic landing in a complex area.

The same logic is applicable to planetary, asteroid, and comet-approach navigation in that areas of known contrast, such as the red spot on Jupiter, could be acquired and tracked

to aid in spacecraft navigation and attitude determination, and scientific observation of the stellar body features of interest.

The flight version of the optical guidance system is expected to weigh approximately 6.35 kg and consume 12 W at 28 V (nominal) of power. The navigation computer would be required to provide two analog or digital signals to position the video scan with respect to the predicted impact point. The computer would perform the sequencing of the video guidance system, accept guidance information in terms of subframe selected or desired direction of travel, and effect the appropriate maneuvering.

The study results and potential benefits relative to interplanetary and lunar missions are summarized in Table X.

Table X Study Results for Interplanetary and Lunar Missions

FUNCTIONAL CAPABILITY AND BENEFITS	SIGNIFICANT STUDY RESULTS
Increased Probability of Mission Success	Demonstrated via Monte Carlo Obstacle Avoidance Experiments on Simulator
Scientific Site Selection	Demonstrated for Areas Having Distinct Signature
Footprint Reduction for Landers and Probes during Deorbit to Parachute Deployment Phases of Flight	MOD6MV Studies Indicate that an Improvement of 50% Is Achievable
Obstacle Avoidance for Planetary Landers	Feasibility Demonstrated in Laboratory
Increased Science Return	Data Rates and Storage for a Viking-Type Lander Will Allow for Scientific Imaging during Approach to Surface
Autonomous Real-Time Operation	Demonstrated in Laboratory for Site Selection and Obstacle Avoidance
Roving Vehicle Traverse Selection	Achievable Through Imaging during Terminal Descent
Planetary, Asteroid and Comet Approach Navigation	Achievable Through Acquisition and Tracking Algorithm for Targets Having Unique Signatures

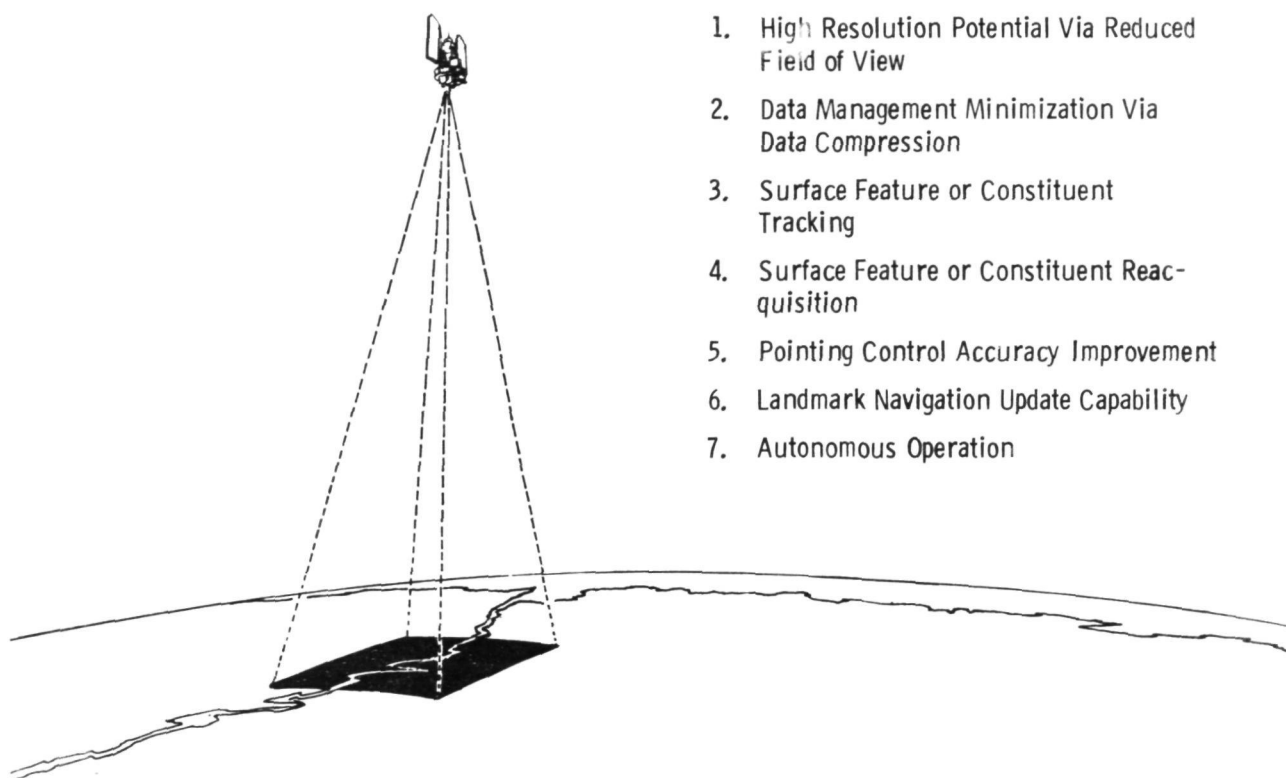
Recommendations for Adaptive Video Guidance System

Having successfully completed the feasibility demonstration, the next step in the evaluation of this technology is to build a prototype system. To arrive at a prototype system, the following tasks should be performed.

- (1) A mission applications study must be performed to optimize performance, assess multimode capability, assess environmental requirements, and to minimize weight, power, and interface requirements.
- (2) An imaging sensor tradeoff study is required to select the most suitable camera for the timeframe of interest. Advanced technology cameras, such as charge-coupled devices, should be considered.
- (3) A laboratory test program should be conducted to evaluate prototype system performance against scaled target models with the anticipated albedo, geomorphological, and illumination characteristics in a similar manner as was done with the breadboard system.
- (4) Continued digital simulation is necessary in order to estimate AVGS impact on fuel, stability, and maneuvering capability for specific trajectories.
- (5) Ultimately, a helicopter flight test would provide an excellent performance evaluation check.

Earth Resources Pointing and Tracking System

The techniques developed for acquisition, pointing, and tracking show promise for recognizing and tracking coastlines, rivers, and other constituents of interest as shown in Figure 83. The laboratory system is simple in design and could significantly enhance scientific imagery acquisition and lower data/information handling requirements. The system would be somewhat independent of the satellite attitude control system and would maintain lock while minimizing the vehicle jitter effects. It could also be applied to position determination of the satellite with respect to known terrain features.



1. High Resolution Potential Via Reduced Field of View
2. Data Management Minimization Via Data Compression
3. Surface Feature or Constituent Tracking
4. Surface Feature or Constituent Reacquisition
5. Pointing Control Accuracy Improvement
6. Landmark Navigation Update Capability
7. Autonomous Operation

*Figure 83 Advantages of a Landmark Tracker
for Earth Orbital Missions*

The study results and benefits achievable are summarized in Table XI.

Table XI Study Results for Earth Resources Missions

FUNCTIONAL CAPABILITY AND BENEFITS	SIGNIFICANT STUDY RESULTS
Remote Acquisition, Pointing and Tracking	Demonstrated Via Coastline and River Acquisition and Tracking Experiments
Data Management Minimization Via Relaxed Resolution Requirements for Camera: Improved Pointing Accuracy Allows Reduced Field-of-View	Achievable Via Constituent Tracking. Transmit only What is Being Tracked with a Smaller Field-of-View
Cloud Detection and Avoidance to Minimize Data Information Handling	Multispectral Identification Appears Promising
Pointing Control Accuracy Improvement	Imaging Acquisition and Tracking System Would Be Independent of Satellite Attitude Control System and Would Maintain Lock on Constituent of Interest. Should Also Minimize Spacecraft Jitter Effects
Autonomous Operation	Demonstrated in Laboratory
Location Accuracy Improvement for Earth Orbiters	Achievable Through Landmark Tracking

Recommendations for the Earth Resources Pointing and Tracking Sensor System

A program should be initiated to design, develop, and demonstrate a prototype system capable of remote acquisition, pointing, and tracking for future earth resources applications such as pollution monitoring, flood plain observations, survey missions, constituent tracking, etc. The goal would be to develop a uniquely simple, lightweight and adaptive sensor mechanization that would enable the use of a scanning imaging

system to acquire and track various targets of scientific interest to maximize the data return for a given mission. Maximum use should be made of the signal processing technology developed in the performance of this study.

The objective would be accomplished by performing the following tasks:

- (1) Identify and select applicable targets and investigate spectral signature characteristics.
- (2) Investigate sensor heads; i.e., Video, RF, and IR scanners as a function of spectral signature characteristics for each target of interest.
- (3) Investigate multimode potential of a given sensor configuration.
- (4) Develop algorithms for laboratory evaluation of imaging concepts resulting from the above tasks. Breadboard algorithms developed during the performance of this study.
- (5) Evaluate existing area correlation techniques and investigate potential use of prestored imagery for missions of interest.
- (6) Perform feasibility demonstration using physical simulator and multidimensional target models where applicable.
- (7) Perform preliminary design of recommended acquisition and tracking system including a sensor head tradeoff study.

Video Stationkeeping and Docking Sensor System

As shown in the laboratory results, the basic routines are written and checked out which will accomplish a multitude of rendezvous, docking, and stationkeeping functions. For steering, the centroid routines would be used. An automatic threshold setting will have to be worked out, as will the guidance equations, to translate the camera image plane coordinates to spacecraft or rendezvous coordinates. Automatic ranging, with dual cameras or split optics, looks feasible with the algorithms as developed. This is attractive since the same

system that provides crossrange steering will also yield range and range rate information.

Close-in steering and stationkeeping with this system also appears feasible, but here special problems must be overcome. Since the object is three dimensional, some distinction must now be made as to what point on the object should be tracked and what parts avoided (i.e., solar panels and booms). Computer logic will be required for this in addition to some type of feature detection. The same basic algorithms will probably be used but will be imbedded in a larger logical procedure for each task.

An algorithm for angular orientation determination was developed and tested, but at present, it is not clear how this will fit into an overall rendezvous and docking scheme. Possibly this will help in feature detection to generate a unique signature.

Study results and achievable benefits of the rendezvous and docking system are summarized in Table XII.

Table XII Study Results for Spacecraft Rendezvous and Docking Missions

FUNCTIONAL CAPABILITY AND BENEFITS	SIGNIFICANT STUDY RESULTS
X-Y Steering during Rendezvous	Centroid Tracking Experiments Demonstrated Feasibility
Range Determination	Achievable Through Prestored Image Comparison and/or Stereo Convergence Angle Calculation
Target Vehicle Angular Orientation Determination	Algorithms Developed and Tested on Simulator. Spacecraft Skin Patterns or Other Visual Cues Such as Lights, Concentric Circles, etc. Would Be Effective.
Target Vehicle Spin Axis Determination	Feasibility Using Scanning and Time Correlation Techniques
Autonomous Real-Time Operation	Demonstrated in Laboratory for Several Algorithms
Multi-Mode Capability	The Same Imaging System Used for Autonomous Rendezvous and Docking Could Be Used for Manual Remote Control and Inspection

Recommendations for Stationkeeping and Docking System

Short-term future work should be in the area of dimensionally calibrating the system, including target and camera. This will involve a mathematical model of the system such that when a position is commanded by the computer, the scan spot on the target is known. An error model will be required. As a result, many frames of the same scene are needed to produce a spread of data and thus the error dispersion for the several measurements. The area calculation errors, for example, will be a function of object size in the field-of-view, sample point resolution, and the focal length. Centroid measurement will also be troubled by lens aberration and angular distance from the optical centerline. These items fall under the category of refinement of the laboratory setup.

Longer term future work should center on the problems of how the system is to be implemented onboard the spacecraft. Here, trades need to be made between using a special analog preprocessor versus a microprocessor dedicated to this task. In each case, the unit should be self contained and not require a great deal of external processing by the onboard computer. Another major area of investigation will be some type of supervisory software to provide autonomous completion of the required task. This will involve a rudimentary artificial intelligence scheme with enough capacity that it will not be easily fooled by the range of scenes it will encounter. The tradeoff here will be between software complexity versus probability of success.

The following tasks would be required:

- (1) Performing a stationkeeping and docking phase requirements analysis for space vehicles such as Shuttle Orbiter, Space Tug, Interim Upper Stage, Earth Orbital Teleoperator Spacecraft, Free Flying Satellite Experiments, and the Astronaut Maneuvering Unit. This will provide the necessary parametric data for establishing a realistic set of design requirements. Consideration should also be given to a multiple spacecraft docking system. Maximum use should be made of past and current study results relating to the various spacecraft;
- (2) Conducting design investigations and feasibility studies on video processing algorithms, hardware

(2) (Continued)

alternatives, target definition, and target spacecraft motion effects. This task involves the utilization of work accomplished at NASA-MSFC and Martin Marietta on the development of stationkeeping and docking algorithms and an evaluation of preliminary experimental results thus far achieved. Camera tradeoffs should also be performed as a function of mission requirements;

- (3) Demonstrating the feasibility of the video system on a computer/hardware six-degree-of-freedom simulator. This will enable the evaluation of various rendezvous and docking algorithms in a dynamic environment with realistic scaled target vehicles;
- (4) Performing a preliminary design for an engineering prototype system for the next phase of development. This will include the definition of weight, power, and cost estimates for the eventual fabrication of a "protoflight" system.
- (5) Design, develop, and evaluate a prototype video stationkeeping and docking sensor system.

Aircraft Approach and Landing System

Another application of this technology is as a terminal guidance system to be used during the cruise, approach, and landing phases for helicopters and RPVs whereupon an autonomous all-weather operational mode is desirable. This mechanization would make use of much of the logic and algorithms already developed during the performance of this study for landing site selection and target acquisition and tracking with an IR or RF sensor in place of the TV camera.

A typical example, as illustrated in Figure 84, is for improving guidance and navigation capabilities of helicopters used both in military and commercial operations. During the cruise phase of flight, this system could be used for landmark (known or unknown) navigation. During the approach and landing phases of flight, the same system could be used to acquire and lock-on to the heliopad, generate steering commands to the flight control system and/or pilot, and therefore provide an autonomous approach and landing capability for helicopters.

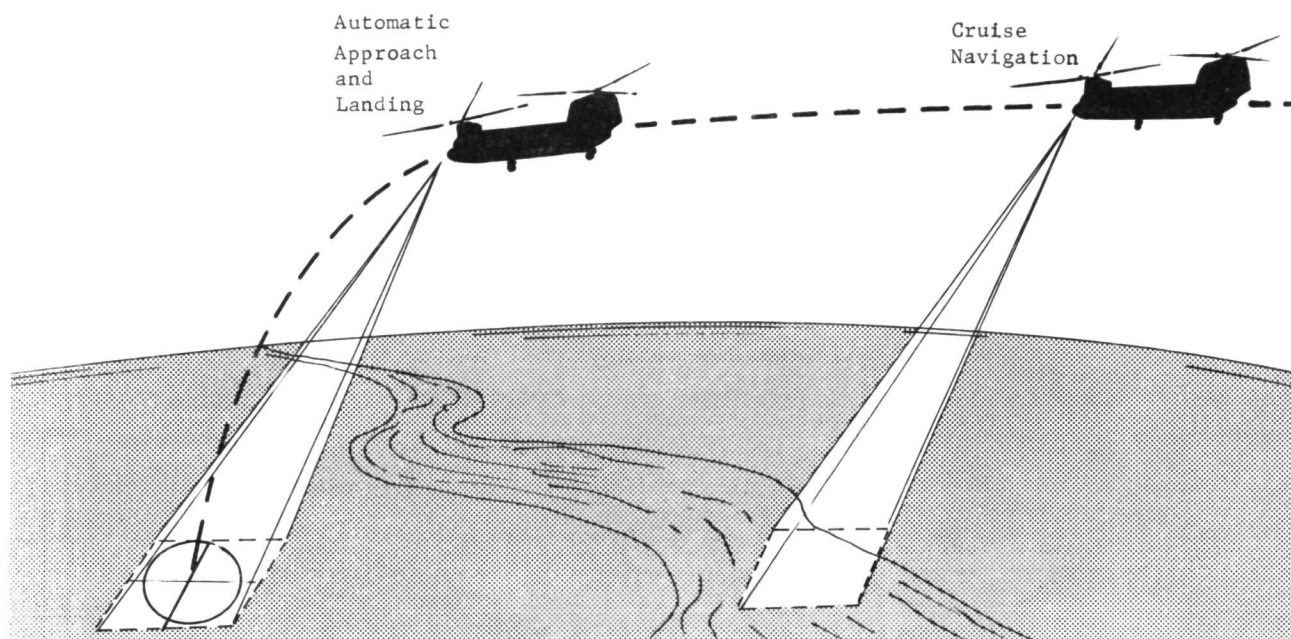


Figure 84 Helicopter Automatic Approach and Landing System

For operation in remote or unimproved areas, the site selection logic would be especially useful for providing to the pilot an estimate of terrain roughness.

This mechanization would benefit VTOL approach and landing technology in a number of ways.

- (1) Reduction of helicopter pilot workload.
- (2) Low-cost direct link helicopter automatic approach and landing system.
- (3) Reduction in inertial hardware performance requirements.

- (4) Visual display in all weather situations.
- (5) Automatic or manual operation.
- (6) Aid to fuel consumption optimization via landmark navigation update during cruise.
- (7) Flight time minimization.
- (8) Remote area IFR capability via site selection logic.
- (9) Possible weapons delivery aid via landmark tracking and offset targeting.

Recommendations for Developing an Aircraft Approach and Landing System

This concept could readily be mechanized and tested in the laboratory by constructing representative scaled landing sites (heliopads), and simulating the IR and/or RF sensor by using a video system and providing the necessary visual aids for a feasibility demonstration. The landmark navigation aspect of this concept has already been successfully demonstrated. Various algorithms should be tested for differing flight path angles and approach rates. Experiments would be run in both manual and automatic modes since this capability already exists in the laboratory.

Future Study Recommendations Summary

This study has resulted in the development and laboratory evaluation of relatively simple algorithms that could immeasurably enhance performance capability and scientific data acquisition for a number of missions. The obvious advantages in terms of data compression, increased probability of mission success, and autonomous operation could well justify the implementation of this type system. Cost should not be a significant factor in that no long-lead items are required unless a peculiar scanning sensor head is desired for a particular spacecraft. For a given mission, the following tasks are recommended:

- (1) Identify and select applicable targets and investigate spectral signature characteristics and mission-related constraints.

- (2) Investigate and select a sensor head; i.e., video, RF, and IR scanners, as a function of target characteristics and mission requirements.
- (3) Optimize algorithms via laboratory evaluation using breadboard hardware and prototype camera.
- (4) Investigate multimode potential.
- (5) Perform preliminary design.
- (6) Build and test "protoflight" system.

Extensive savings in cost and time will result through the use of the operational six-degree-of-freedom simulator laboratory due to the built-in flexibility, available control modes and signal processing hardware.